DETECTION OF MAN MADE TARGETS USING RADAR POLARIMETRY

by

FLAVIO WASNIEWSKI

B.Sc., Universidade Estadual do Rio de Janeiro, Rio de Janeiro, Brazil, 1995

A THESIS SUBMITTED IN PARTIAL FULFILLMENT OF THE REQUIREMENTS FOR THE DEGREE OF

MASTER OF APPLIED SCIENCE

in

THE FACULTY OF GRADUATE STUDIES

(Electrical and Computer Engineering)

THE UNIVERSITY OF BRITISH COLUMBIA

August 2007

ABSTRACT

Since the late 1970's, various synthetic aperture radar (SAR) satellite missions have provided a valuable source of information about the earth's surface. Providing their own illumination, these sensors generate imagery of our planet 24 hours a day, regardless of cloud cover.

Until recently, except for the short term space shuttle SIR-C system, these SAR missions carried single-polarized sensors, meaning that the information extracted from the imagery, and the resulting quality of interpretation, was limited.

In 2006 the first of a series of planned satellites carrying fully polarimetric SAR sensors was launched. In polarimetric SAR systems, images can be acquired with horizontal (H) and vertical (V) polarizations of the electric field on both transmission and reception. The resulting multipolarized imagery makes available a higher level of information content for a number of applications, including man made target detection. The potential of polarimetric SAR for man made target detection is investigated in this thesis.

In the man made target detection field, the purpose is to differentiate the signature of the targets from those of adjacent natural areas. The most operationally successful application in this field is ship detection, as the sea surface usually forms a quite homogeneous and easily distinguishable clutter. Vegetated surfaces, however, usually constitute a more challenging clutter, as the backscatter levels can be very high and the signatures diverse, often being confused with those of man made targets.

A few algorithms have been developed with the purpose of separating the targets from clutter. A methodology that employs the following three algorithms was recently tested in order to discriminate crashed aircraft from the surrounding terrain: Polarimetric Whitening Filter (PWF), Even Bounce Analysis and Cameron Decomposition. In these tests, successful results were achieved when the terrain was composed of a homogeneous field of grass and the targets were crashed airplanes.

In this work the same methodology is tested with different man made targets and with different clutters. Also, methodologies involving the use of two other algorithms are tested in order to reduce the false alarm rates. These algorithms are Coherence Test of the Symmetric Scattering Characterization Method (SSCM) and Freeman-Durden Decomposition.

The methodologies are applied to three different data sets acquired over different Canadian locations - Ottawa (ON), Gagetown (NB) and Vancouver (BC) – with the CV-580 polarimetric SAR system and the false alarm rates are assessed. Results show that the Coherence Test can lower false alarm rates on high vegetation clutter when applied in combination with other algorithms, while Freeman-Durden Decomposition does not perform effectively in the same experiments.

TABLE OF CONTENTS

LIST OF TABLES

LIST OF FIGURES

ACKNOWLEDGEMENTS

I owe my gratitude to my supervisor, Dr. Ian Cumming, who always had a word of good advice and academic guidance when needed and for his understanding attitude. He was also generous both on sharing his knowledge in SAR and on making himself available even after his retirement.

I am also thankful to Dr. Rabab Ward for co-supervising me in the final stage of my thesis and for making the Image Processing Lab such a friendly environment for myself and for my lab mates during these years.

Many thanks to Dr. Tom Lukowski, from the Defence Research and Development Canada (DRDC), and Dr. François Charbonneau, from the Canada Centre for Remote Sensing (CCRS) and the authors of some of the key papers cited in this work, for sharing their knowledge on radar polarimetry and for patiently answering the many questions I asked.

I also wish to thank the RADARSAT-2 Group from Radarsat International (now MDA-GSI), led by Dr. John Hornsby, for their support and for providing the Gagetown CV-580 data for my research project.

Kaan Ersahin and Colette Wabnitz: thank you for denying me authorization to be unmotivated in the most difficult days.

Stephen, Erin, JoAnne, Jeff, Gillian, Aline, Gwendal, Tania, Verda, Karina, Clarice, Kyle, Pamela, Travis, Erin J, Wellington, Natalia, Marian and Eva are among the friends who deserve thanks for all their encouragement and for making me feel at home in Vancouver. And so do fellow SAR students Kaan, Millie, Bernd, Shu and Yew Lam, who were very important in this journey for all their help and good company.

Very special thanks to Kelly Hamilton for being both a companion and an inspiration during the hard times of my thesis completion period.

And finally I would like to thank my family for the many years of love and investment in my education that brought me to this stage, and also for their continuous unconditional support even from distant Rio de Janeiro, Brazil.

Flavio Wasniewski

The University of British Columbia
August 2007

To my friends
Wolymir, Joselita, Ricardo and Marília

CHAPTER 1 - INTRODUCTION

1.1 Radar Polarimetry

The word *Radar* is an acronym for *radio detection and ranging*. Radar systems transmit short pulses of microwave energy and record the strength of the echoes received from the objects within the radar field of view. Radar remote sensing systems use an antenna fixed below an aircraft or spacecraft and pointed to the side. By providing their own illumination in the microwave portion of the spectrum, these systems provide information on ground features that neither photogrammetric systems nor optical satellites systems – the two most common imaging systems used in remote sensing – can provide.

Due to this characteristic and to its capability of penetrating the atmosphere under virtually all conditions, including poor weather and night imaging, Synthetic Aperture Radar (SAR) has been, especially in the last three decades, a field that attracted both research and commercial interest in remote sensing. The development of airborne and spaceborne earth observation SAR systems and the consequential increase in data availability have led to a high demand for technical expertise in the area. The RADARSAT-1, ERS-1, JERS-1 and ERS-2 satellites are some of the most representative systems of this era (see Table 1), and some of these satellites are still operating. Among these systems SIR-A, SIR-B and SIR-C were short duration missions (3 to 10 days) on board the NASA Space Shuttle.

These SAR systems transmit and receive waves in the same polarization state. The measured data are typically the amplitude and differential phase of the received wave as compared to the transmitted one. However, as a result of its interaction with the earth's surface, the received wave can have its polarization state changed into one the receiver may be partially or completely blind to.

Sensor	Country	Launch	Polarization	Band
SEASAT	USA	1978	HH	L
SIR-A	USA	1981	HH	L
SIR-B	USA	1984	HH	L
ALMAZ	Soviet Union	1991	HH	S
ERS-1	EU	1991	VV	C
JERS-1	Japan	1992	HH	L
SIR-C	USA	1994	Quad	X, C, L
ERS-2	EU	1995	VV	C
RADARSAT-1	Canada	1995	HH	C

Table 1: Single polarized spaceborne missions (with the exception of SIR-C).

In order to be able to measure the received waves in different polarization states and to increase the information content of SAR data, polarimetric SAR (which in this thesis will be referred to as *polarimetric radar*) systems were developed. These systems can transmit and receive waves in two orthogonal polarization states, and therefore provide more information on the physical attributes of the target.

Polarimetric radar systems generate data in four channels, corresponding to the combinations of the transmitted and received horizontal (H) and vertical (V) waves. These channels are typically named HH, HV, VH and VV. An illustration of the dependence of the radar's response to polarization is shown in Figure 1, where three C-band images (HH, HV and VV) acquired by the CV-580 airborne system over Gagetown (NB, Canada) are shown along with a colour composite of them, for better visualization.

Figure 2 shows the same area imaged by the optical satellite system Quickbird and by the C-band, HH polarized RADARSAT-1 satellite for comparison. The optical image is a RGB colour composite of the Red, Green and Blue bands (Quickbird channels 3, 2 and 1, respectively) and is therefore very close to the terrain's natural colours (Figure 2(a)). A visual comparison with the polarimetric colour composite – Figure 1(d) – is a snapshot of how different their information contents are. Differences between the HH, HV and VV

channels are easily seen in the RGB colour composite (HH – R, HV – G and VV – B). The RADARSAT-1 image shown in Figure 2(b) and the CV-580 image shown in Figure 1(a) both have the same polarization and have a high degree of similarity. The differences between them are due to their different resolutions, incidence angles and look directions. Terrain differences such as moisture content could also play a role as the images were acquired on different dates.

The research on radar polarimetry has received important contributions at least since the 1940's, when George Sinclair showed that a radar target can change the incident wave's polarization and have its properties expressed as a 2x2 scattering matrix. In 1952 Kennaugh demonstrated that there are polarization states for which the radar receives maximum or minimum power, and how these states can be optimized [3]. Huynen followed in the 60's showing how the targets physical structure and geometry could be determined by the radar wave's backscattered polarization states, and in the late 70's Boerner's extension of Kenaugh's work on optimal monostatic polarization to the bistatic case was influential in the addition of polarimetric capability to the civil and military radars [3].

NASA's Jet Propulsion Laboratory (JPL) built the first fully polarimetric radar in 1985. This system was upgraded to the AIRSAR system in the early 90's, which was followed by similar systems from research institutions in Canada (CV-580), Denmark (EMI-SAR) and others. With the data acquired by these airborne sensors, recent research has been able not only to advance the theory but to start bridging the gap between theory and successful operational applications. The recent launch of the first three satellites carrying polarimetric radar sensors and the approaching launch of others (see Table 2) will increase the data availability and provide extensive and periodical coverage of the earth's surface, bringing promising improvements in radar remote sensing applications compared to the current single polarized satellites. Some of these fields are: sea ice classification, ship detection, crop type and condition classification, soil moisture, search and rescue and forest management [6] [7]. While dual polarization systems can acquire simultaneous images in two different polarizations, quad polarization systems can acquire four simultaneous images (HH, HV, VV, VH).

These four channels can provide complete radar scattering information of the earth's surface, for the given frequency, incidence angle and look direction.

Sensor	Country	Launch	Polarization	Band
ENVISAT/ASAR	EU	2002	Dual	C
ALOS/PALSAR	Japan	2006	Quad	L
TerraSAR-X	Germany	2007	Quad	X
RADARSAT-2	Canada	2007	Quad	C
RISAT	India	2008	Quad	C
COSMOS-Skymet	Italy	2008	Quad	X
SAOCOM	Argentina	2008	Quad	L

Table 2: Current and planned spaceborne polarimetric radar systems.

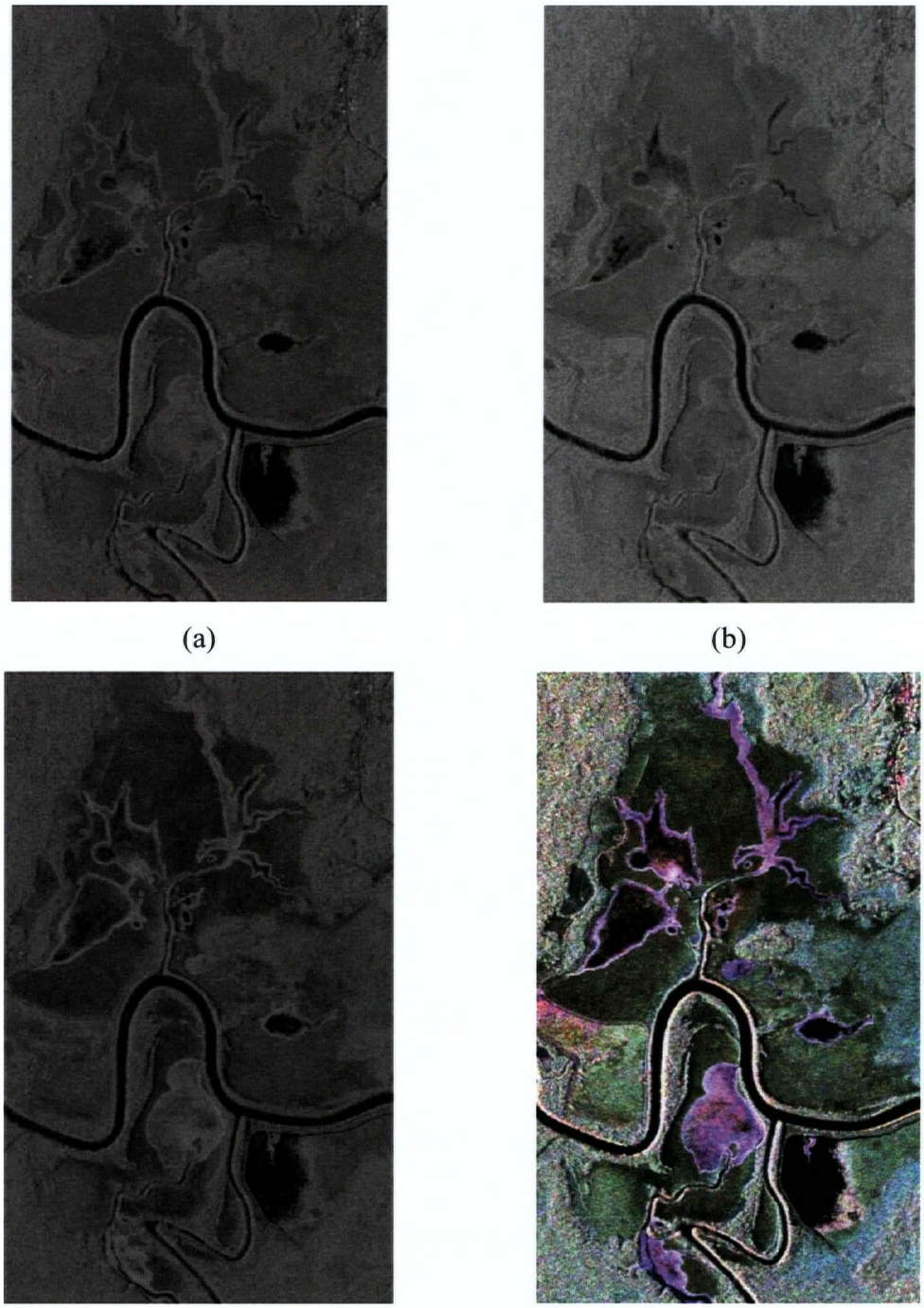

(a) (b)

(c) (d)

Figure 1: Swamp area in Gagetown (NB, Canada) imaged on 9/11/2001 by the CV-580 airborne system (C-band). (a) HH (b) HV (c) VV and (d) RGB colour composite.

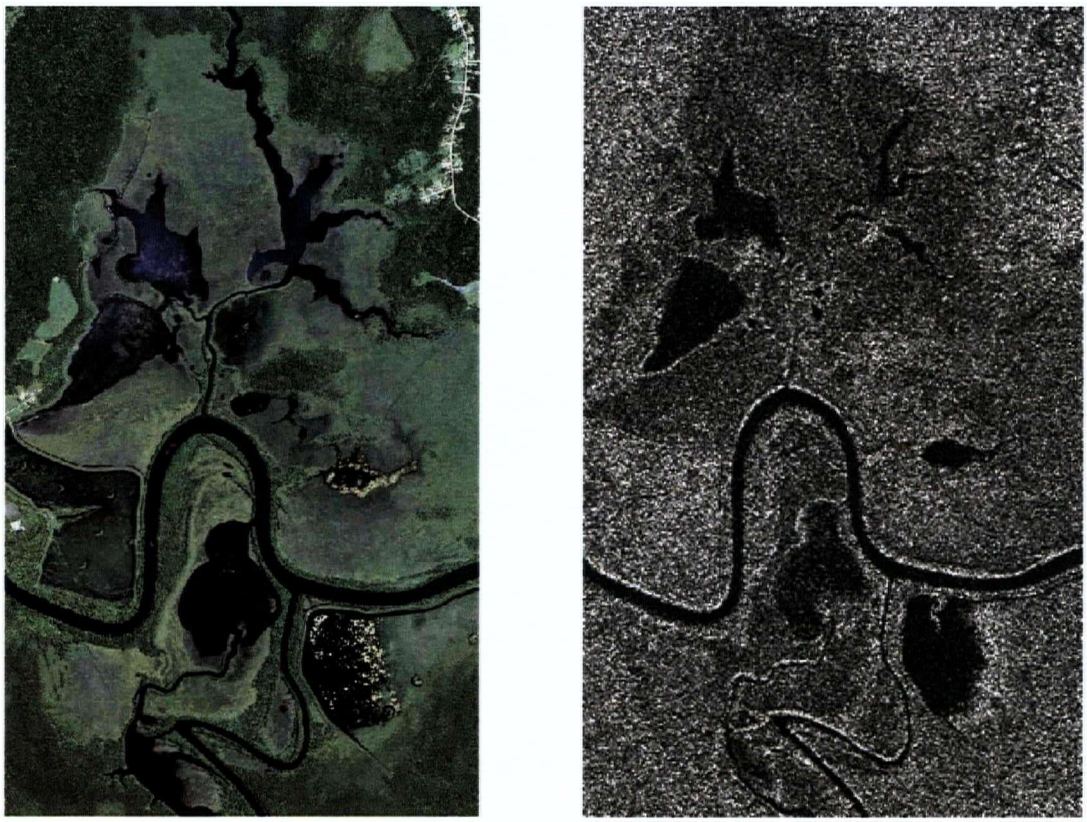

(a) (b)

Figure 2: Quickbird and RADARSAT -1 images over the Swamp area in Gagetown (same area as in Figure 1) (a) Quickbird image (b) RADARSAT-1 Fine Beam Mode (C-band).

1.2 Thesis Objectives and Outline

The noticeable increase of research in radar polarimetry applications in the last few years led to the development of a number of algorithms and methodologies in various fields. The detection of man made targets, encompassing many possible applications such as ship detection, search and rescue, mapping and surveillance, are some of these fields, and are expected to benefit significantly from the advent of the spaceborne polarimetric radars.

The main purpose of this work is to experiment with a few of the algorithms that can potentially be used for the detection of man made targets and describe their performance

for different targets and clutters. The results that will be obtained in this thesis with airborne data are expected to be, to a large extent, applicable to datasets that will be generated by future radar satellites mentioned in Section 1.1, providing a contribution to the users of polarimetric radar data.

Target detection involves discriminating a discrete target within a vegetation clutter and identifying it as a likely man made target. This is all that is required for some applications, while for others it is necessary to add one more step: *target recognition*. The development of Automated Target Recognition (ATR) systems is a very specialized field of research, and typically relies on high resolution data (0.3 – 1m). Some of the algorithms used here might help with the identification when the targets are large compared to the sensor resolution. However, target recognition is not within the objectives of this work.

In order to test the polarimetric radar detection capabilities, a specific methodology will be used as a starting point: the use of polarimetric imagery for the detection of crashed airplanes, as used by Tom Lukowski and others [8] [9] [10]. This methodology uses three main algorithms applied with a constant false alarm rate (CFAR) detector and image morphology processing in order to detect crashed aircraft in a homogeneous clutter of grass. These algorithms are Polarimetric Whitening Filter (PWF), Cameron Decomposition (CD) and Even Bounce Analysis. In this work this methodology will be referred to as DCA (detection of crashed airplanes).

In this thesis, the DCA methodology is applied to more generic situations: instead of crashed airplanes only, any man made feature is accepted as a target, and instead of grass only, any kind of vegetation is accepted as clutter.

In some of these situations, particularly when the clutter is composed of high vegetation, it is reasonable to expect an increase in the false alarm rates. In order to keep these rates at a low level, and in order to test other algorithms' effectiveness for man made target detection, two other methodologies are proposed and tested here:

First, PWF and Even Bounce Analysis are replaced in the DCA methodology by Coherence Test, which is part of the Symmetric Scattering Characterization Method (SSCM) [16]. Second, the Freeman-Durden decomposition is applied using the percentage of dihedral response as a threshold and also followed by morphology processing. The methodologies and algorithms used are described in Chapter 4.

Chapter 2 describes the most relevant principles related to radar polarimetry and used in this work, from the behavior of EM wave propagation and its interaction with surfaces to the various matrices used in the description and processing of polarimetry data.

Chapter 3 provides a general description of target decomposition in polarimetry and a few of the techniques resulting from recent developments in the target detection field. This provides context to the methods described in Chapter 4.

Chapter 5 describes the datasets used in this work, a brief description of the data acquisition platform (CV-580) and the data format.

Finally, details on the targets, processing, results, analysis and conclusions are provided in Chapters 6 and 7.

CHAPTER 2 - FOUNDATIONS OF RADAR POLARIMETRY

2.1 EM Waves and Their Polarization

2.1.1 EM Waves

Electromagnetic (EM) Waves are composed of electric (*E*) and magnetic (*H*) fields. These fields are perpendicular to each other, and their relationship and description at any position and time satisfy Maxwell's equations [1]. Accordingly, an electromagnetic wave can be fully characterized by its electric field vector, described by the following equation [2]:

$$\vec{E}(\vec{r},t) = E_x\vec{x} + E_y\vec{y} = [a_x.\exp(j\delta_x)\vec{x} + a_y.\exp(j\delta_y)\vec{y}].\exp[j(wt - kz)] \quad (1)$$

where:

w is the angular frequency of the radar wave;

δ_x and δ_y are the x and y phases of the $\vec{E}$ components.

The real vector $Real(\vec{E})$ has the following Cartesian components:

$$\begin{aligned} E_1 &= a_x \cos(\tau + \delta_x) \\ E_2 &= a_y \cos(\tau + \delta_y) \end{aligned} \quad (2)$$

where $\tau = wt - kz$.

If we eliminate the parameter τ in (2), we get the following equation of a conic:

$$\frac{E_1^2}{a_x} + \frac{E_2^2}{a_y} - 2\frac{E_1}{a_x}\frac{E_2}{a_y}\cos\delta = \sin^2\delta \quad (3)$$

where $\delta = \delta_x - \delta_y$.

As the radar wave (1) can be considered monochromatic and fully polarized, a_x, a_y and δ are constant, making (3) the equation of an ellipse (*fully polarized* is defined in Section 2.1.4). This shows that, as the wave propagates, its electric field vector tip traces an ellipse.

2.1.2 Linear Polarization

One of the important properties of plane EM waves is ***polarization***, which is the way an electromagnetic wave oscillates as it travels. The polarization of a wave can be linear, circular or, more generically, elliptical.

If we take a plane perpendicular to the direction of propagation, a linearly polarized wave will trace a straight line on this plane. Two particular cases, a vertically polarized wave and a horizontally polarized one, will respectively trace a vertical line and a horizontal line. The directions H (horizontal) and V (vertical) are commonly used in polarimetry instead of the x and y directions.

In linearly polarized waves the two components will present a phase difference $\delta = 0$ or a multiple number of π.

2.1.3 Elliptical Polarization

Instead of tracing a vertical or horizontal line on a plane perpendicular to the direction of propagation, the wave could trace a circle or an ellipse – which correspond, respectively, to circular or elliptical polarizations. It can also have a direction of rotation, which can be right-handed or left-handed – respectively clockwise or counterclockwise, for an observer looking in the direction of propagation.

The elliptical shape that would be traced by the wave's E vector, whether linear or elliptical, is called the wave's polarization ellipse (Figure 3). The length of the semi-major

axis of the ellipse characterizes the wave's amplitude, and its polarization is defined by two angles: the ellipticity χ and the orientation ψ.

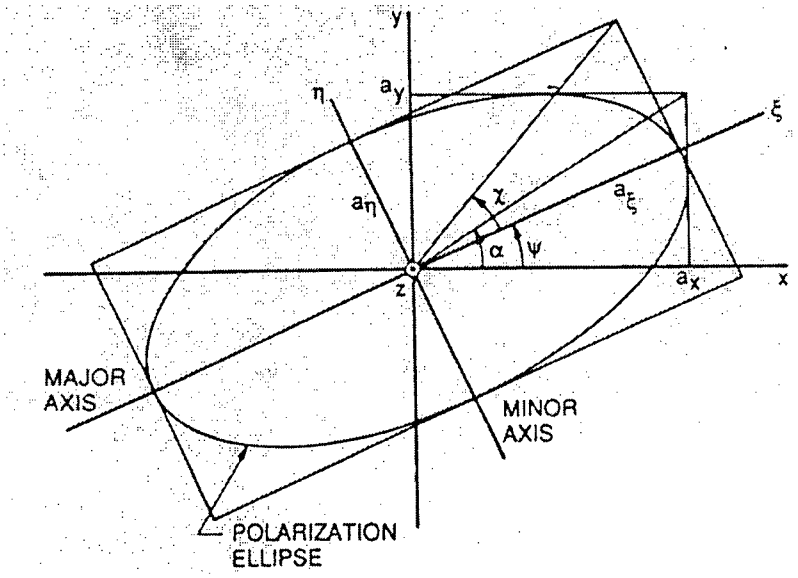

Figure 3: Polarization ellipse in the x-y plane.

The ellipticity describes the "fatness" of the polarization ellipse. It is measured from the major axis of the ellipse to the line connecting the intercept of the major and minor axes with the outline of the ellipse, and it can range from -45° to +45°. When the ellipticity angle is 0 degrees, the polarization is linear, and when it is 45°, the polarization is circular (+45° for left circular and -45° for right circular). The ellipticity χ can be defined as:

$$\chi = \arctan(a_\eta / a_\xi) \tag{4}$$

The orientation angle describes the "tilt" of the ellipse. It is measured from the horizontal axis (x, in Figure 3) to the major axis of the ellipse, and can range from 0 to 180 degrees.

The polarization angles can be expressed in terms of the wave parameters a_x, a_y and δ by:

$$\begin{aligned} \tan 2\psi &= (\tan 2\alpha)\cos\delta \\ \sin 2\chi &= (\sin 2\alpha)\sin\delta \end{aligned} \tag{5}$$

where α is defined by:

$$\tan\alpha = a_y / a_x \tag{6}$$

2.1.4 Partial Polarization

A wave is said to be completely polarized when its orientation and ellipticity are constant. When its polarization state is time dependent, the wave is either completely unpolarized or partially polarized. The partially polarized wave can be understood as a sum of a completely polarized and a completely unpolarized wave, and has therefore a degree of polarization.

Partially polarized waves are well characterized by mathematical relations among the Stokes vector elements. The Stokes vector describes the polarization state of an EM wave and is:

$$\begin{bmatrix} S_0 \\ Q \\ U \\ V \end{bmatrix} = \begin{bmatrix} |E_v|^2 + |E_h|^2 \\ |E_v|^2 - |E_h|^2 \\ 2\,\mathrm{Re}\{E_v E_h^*\} \\ 2\,\mathrm{Im}\{E_v E_h^*\} \end{bmatrix} = \begin{bmatrix} S_0 \\ S_0 \cos 2\psi \cos 2\chi \\ S_0 \sin 2\psi \cos 2\chi \\ S_0 \sin 2\chi \end{bmatrix} \tag{7}$$

The completely polarized case follows the relation:

$$S_0^2 = Q^2 + U^2 + V^2 \tag{8}$$

where S_0^2 is the total power, and the terms Q^2, U^2 and V^2 of the Stokes vector give the polarized part of the power. That explains the equality with a completely polarized wave, and the following inequality for a partially polarized wave:

$$S_0^2 > Q^2 + U^2 + V^2 \tag{9}$$

The degree of polarization (d) is shown below. It has an important physical meaning: it is related to the purity of the scattering mechanism (which is defined in item 2.2.2). Surface scattering results in values of d close to 1 while diffuse (volume) scattering results in values of d close to 0. This loss of polarization caused mostly by terrain interaction and represented by the lowering of d is called *depolarization*.

$$d = \frac{\sqrt{Q^2 + U^2 + V^2}}{S_0} \tag{10}$$

The elements Q, U and V represent respectively the linear polarization, orientation and circular polarization contents of the wave [5]. Therefore, more specific relations can be defined, such as the degree of linear polarization (equation 11) and the degree of circular polarization (equation 12):

$$\frac{\sqrt{Q^2 + U^2}}{S_0} \tag{11}$$

$$\frac{V}{S_0} \tag{12}$$

2.2 Interaction of EM Waves with Scattering Objects

2.2.1 Introduction

After interacting with the incident wave, each scatterer on the ground will produce a scattered wave which could have a different polarization from the incident wave. For any given pixel, the resulting scattered wave is a vector addition of all the individual scatterers waves in that pixel and will have contributions in both the vertical and horizontal axes.

The orthogonal contributions of the signal received by the radar can be described by different types of matrices, which contain information about the amplitude and phase of the scattered wave in both directions. Polarimetric radar scattering information can be stored in a scattering matrix, a covariance matrix, a coherency matrix or a Stokes matrix. These matrices are explained below in sections 2.2.3 to 2.2.6.

The coherency and covariance matrices contain information on correlation properties of the scatterers and are therefore more convenient for manipulation of data containing distributed targets such as clutter.

2.2.2 Scattering Mechanisms

The different ways the ground features scatter the incident waves can be expressed as a composition of simple scattering behaviors. Those behaviors, represented by elemental scatterers, are called scattering mechanisms. Some examples of scattering mechanisms are: Sphere (single bounce), dihedral (double bounce), helix, trihedral (odd bounce), cylinder and dipole (a random distribution of dipoles represents diffuse scattering). Figure 4 shows sketches of three common scattering mechanisms.

These scattering mechanisms are expressed as specific scattering matrices, and can therefore be retrieved when fully polarimetric information is available. Identifying the

dominant scattering mechanisms in each resolution cell gives information on the target structure [14]. This identification can be a complex task, which is made easier by knowing the result of the wave's interaction. For example: a double bounce typically causes a 180 degrees shift in the phase difference between the vertical and horizontal components of the wave. In general, but not necessarily, the higher the number of bounces – as in diffuse scattering – the more likely the wave will have its polarization state transformed, a phenomenon called repolarization [3]. Also, the larger will be its unpolarized component.

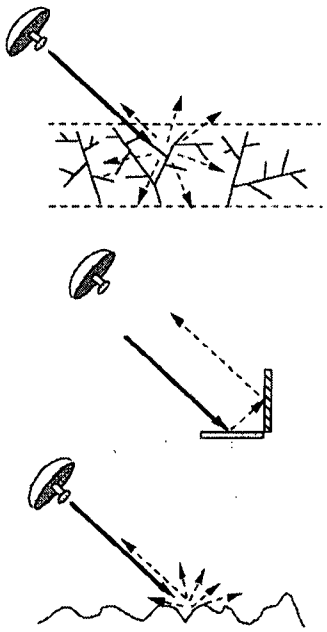

Figure 4: Representation of three scattering mechanisms: diffuse canopy scatter (top), double-bounce scatter (middle) and surface scatter (bottom). Adapted from Freeman and Durden [18].

2.2.3 The Scattering Matrix

For a radar system that coherently transmits and receives both horizontal and vertical polarizations, a complete scattering matrix can be constructed for each pixel. Both the amplitude and phase for each channel are recorded.

The elements of the scattering matrix are functions of the radar wavelength and the illuminating and scattering geometries. There will be a separate complex scattering matrix for each pixel of the image, but other data representations derived from this matrix can be more directly useful in data analysis. The scattering matrix also contains noise, which is typically introduced at the radar receiver.

The scattering matrix can be represented as the following relation between the electric fields of the incident and scattered waves:

$$\begin{bmatrix} E_h^s \\ E_v^s \end{bmatrix} = \begin{bmatrix} S_{hh} & S_{hv} \\ S_{vh} & S_{hh} \end{bmatrix} \begin{bmatrix} E_h^i \\ E_v^i \end{bmatrix} \tag{13}$$

where the superscripts "*i*" stand for "incident" and "*s*" for "scattered", and subscripts *h* and *v* stand for horizontal and vertical.

In the *monostatic* case (when the radar transmitter and receiver are located in the same spot), the reciprocity principle dictates that $S_{hv} = S_{vh}$, thus reducing the number of independent parameters. From now on, only the monostatic case will be considered in this thesis.

2.2.4 The Covariance Matrix

Many forms of analysis are performed more efficiently when power representations of the scattering matrix are used, and the Covariance Matrix is one of the most common ones. This matrix is the inner product of the scattering vector with itself. The scattering vector has the same components of the scattering matrix, but in vector form:

$$\mathbf{k}_C = \begin{bmatrix} S_{hh} \\ \sqrt{2}S_{hv} \\ S_{vv} \end{bmatrix} \tag{14}$$

and therefore the covariance matrix has the following form:

$$\mathbf{C} = k_C \cdot k_C^{+} = \begin{bmatrix} |S_{hh}|^2 & \sqrt{2}S_{hh}S_{hv}^{*} & S_{hh}S_{vv}^{*} \\ \sqrt{2}S_{hv}S_{hh}^{*} & 2|S_{hv}|^2 & \sqrt{2}S_{hv}S_{vv}^{*} \\ S_{vv}S_{hh}^{*} & \sqrt{2}S_{vv}S_{hv}^{*} & |S_{vv}|^2 \end{bmatrix} \tag{15}$$

where + denotes conjugate transpose and * the conjugate.

As this matrix is formed by the products of the backscatter measured in the antenna (voltage units) it relates the power of the incidence and the scattered waves.

2.2.5 The Coherency Matrix

Another commonly used matrix is the "coherency matrix". Sometimes the interpretation of the physical scattering mechanisms is easier using this matrix, which is:

$$\mathbf{T} = k_T \cdot k_T^{+} = \frac{1}{2}\begin{bmatrix} |S_{hh}|^2 + 2\Re(S_{hh}S_{vv}^{*}) + |S_{vv}|^2 & |S_{hh}|^2 - 2\mathrm{j}\Im(S_{hh}S_{vv}^{*}) - |S_{vv}|^2 & 2S_{hh}S_{hv}^{*} + 2S_{vv}S_{hv}^{*} \\ |S_{hh}|^2 + 2\mathrm{j}\Im(S_{hh}S_{vv}^{*}) - |S_{vv}|^2 & |S_{hh}|^2 - 2\Re(S_{hh}S_{vv}^{*}) + |S_{vv}|^2 & 2S_{hh}S_{hv}^{*} - 2S_{vv}S_{hv}^{*} \\ 2S_{hv}S_{hh}^{*} + 2S_{hv}S_{vv}^{*} & 2S_{hv}S_{hh}^{*} - 2S_{hv}S_{vv}^{*} & 4|S_{hv}|^2 \end{bmatrix} \tag{16}$$

This matrix is obtained by using the following vector:

$$\mathbf{k}_T = \frac{1}{\sqrt{2}} \begin{bmatrix} S_{hh} + S_{vv} \\ S_{hh} - S_{vv} \\ 2S_{hv} \end{bmatrix} \tag{17}$$

Both this matrix and the covariance matrix are by definition hermitian matrices and have the same real non-negative eigenvalues, but different eigenvectors. The covariance matrix and the coherency matrix are linearly related.

2.3 Radar Systems and Polarimetry

Radar polarimetry tries to determine the polarization content of every resolution cell in the image as a way to derive information on the scatterers on the ground. In order to fully characterize a scatterer, the full scattering matrix must be measured. This requires the radar system to transmit and receive at two orthogonal polarizations, and that the system retains the coherent phase information for the transmitted and received waves.

The transmitting antenna of the radar system determines the polarization of the emitted wave, and the receiving antenna determines which polarization of the returned signal will be recorded. In fully polarized data there are four polarization combinations based on the systems transmit/receive polarization. These linear polarization combinations are named using the following convention:

HH = horizontally polarized transmit and received signal,
HV = horizontally polarized transmit signal and vertically polarized received signal,
VH = vertically polarized transmit signal and horizontally polarized received signal,
VV = vertically polarized transmit and received signal.

Different transmit polarizations can cause radar waves to interact differently with the surface and produce different returns. Therefore, when interpreting surface characteristics from a radar image it is important to know the polarization combination used to collect the image. In radar polarimetry the amplitude and phase of the four possible combinations are used to extract terrain information.

Like-polarized images (VV and HH) will in most situations have stronger returned signals and higher signal to noise ratios than cross polarized images (VH and HV). This is because natural scatterers, on average, only repolarize a small amount of the transmitted wave.

Many differences in contrast between differently polarized images can be noticed for various types of surfaces. When the plane of polarization of the transmitted wave is parallel to the dominant plane of linear features on the surface, the like-polarized radar return will be stronger than if the radar wave had the orthogonal polarization. As an example, some crops like wheat, which have a vertical structure, will result in a stronger signal in the VV channel, and appear more clearly in the associated VV image.

2.4 Polarization Synthesis

Once the scattering matrix is known, one can synthesize the radar response for any possible transmit and receive polarizations. This is called polarization synthesis, and is used to construct images in different polarization combinations. The synthesized image can be constructed by computing the Stokes matrix from the scattering matrix and then pre-multiplying and post-multiplying it by the unit Stokes vector (*see Section 2.1.4*) that contains the chosen receive and transmit polarizations.

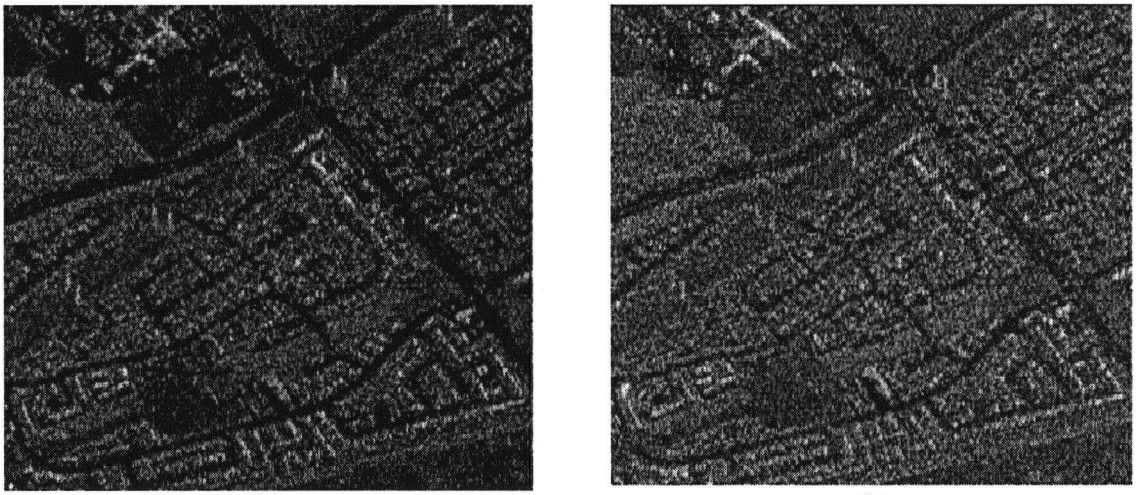

(a) (b)

Figure 5: Examples of synthesized images. (a) VH polarized image, (b) Right-Left circularly polarized synthetic image. The data was acquired by the CV-580 SAR system.

In radar polarimetry applications, creating a synthetic set of images that enhance the features to be detected can be very useful. For discrete targets, as an example, the target-to-clutter ratio can be maximized by selecting the appropriate polarization combination, therefore increasing the detectability of the target.

2.5 Polarization Signatures

A polarization signature is a way to visualize the response of a target for different possible transmit and receive polarizations. They are a plot of the backscatter received as a function of four independent variables: the ellipticity and orientations of the incident wave and the ellipticity and orientation of the receiving wave.

The plot is a surface plot, as in Figure 6, mapped over a two dimensional grid (χ = -45deg. to 45 deg. and ψ = 0 deg. to 180 deg.). As a complete mapping of all the variables is too complicated for interpretation, only two variables are used at a time to portray the polarization signatures: the ellipticity and orientation of the incident wave. For simplicity,

the plot shows two particular cases: The co-polarization signature, where the backscatter is computed for when the transmitted and received waves are the same polarization; and the cross-polarization signature, where the received polarizations are orthogonal to the transmitted ones.

The two main features that help with the interpretation of the plots are the shape of the 3D surface and the pedestal height. The surface symmetry, and the existence and location of peaks are indicators of the scattering mechanism that originated it. The pedestal height is the minimal value of intensity of the plotted surface, and its presence indicates the existence of an unpolarized scattering component in the received signal. The larger this component is, the larger the presence of random scattering from the target.

Polarization signatures are generally not very useful for target analyses as they are not clear in the absence of pixel averaging.

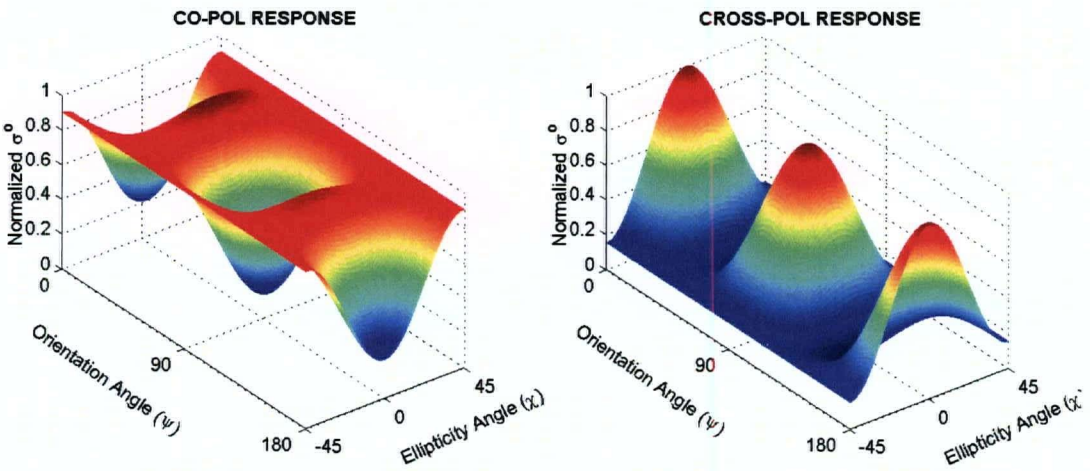

Figure 6: Co-pol and cross-pol polarization signatures of a forested area in Gagetown (NB, Canada).

CHAPTER 3 - THE DETECTION OF MAN MADE TARGETS

3.1 Man Made Targets in Radar Polarimetry

The concept of a feature as being a *target* has military origins and brings the notion of being both "significant" and surrounded by a background clutter. Typical man made targets are buildings, vehicles, power lines or train tracks, whereas typical natural targets are forests, crop fields, water and bare soils.

In remote sensing, man made targets (as well as natural ones) in a scene are often perceived differently by different sensors. This will depend not only on the physical properties of the target but also on factors such as the frequency in the EM spectrum and the resolution of each sensor. In the case of polarimetric radars, these targets will typically be perceived by their:

- characteristic changes in the phase and amplitude of the wave's orthogonal components due to the large presence of scatterers of right angles, planes or cylinders; or
- higher levels of backscattering compared to the clutter.

In the polarimetric analysis, man made targets can be considered as *pure* targets – whose signature can be completely determined by the measured scattering matrix. Man made targets are also characterized by local *structure* rather than texture [4], and by tridimensional geometrical shapes. Natural targets, which can be treated as homogeneous, are considered *distributed* targets.

3.2 Target Detection Methods

3.2.1 Introduction

The purpose of this section is to provide an overview of the current target detection (TD) techniques used in radar polarimetry, including some of the recent research and developments. This will provide the context for understanding the methodology used in this work, as described in Chapter 4.

For SAR image users in general, man made targets are often expected to have a higher backscatter level than the mean of the surrounding natural clutter. Therefore, one could think that we could detect them by thresholding the magnitude of the data. However, this alone may not produce acceptable results. This is because natural targets can sometimes have a high backscatter response and speckle noise, which can cause high statistical variability in the image.

As these factors can cause a large number of false targets, different algorithms have been developed to take advantage of the relationships that exist between phase and amplitude at different polarizations. Many of these algorithms employ target decompositions and different polarimetric discriminators in order to detect targets. Being considered pure targets, man made targets will typically have their physical properties better characterized when coherent decompositions are employed, while non-coherent decompositions are commonly employed for distributed targets.

3.2.2 Coherent and Non-Coherent Target Decompositions

Target decomposition techniques aim at expressing the average scattering mechanism as a sum of independent components [2]. These components will usually, but not necessarily, belong to orthogonal vector spaces, and for operational purposes a decomposition should successfully associate a meaningful physical property to each component. The physical properties identified for each data pixel will contain information about the imaged target.

Methods of target decomposition can be distinguished as: coherent target decomposition (CTD) and non-coherent target decomposition. When the target can be characterized by a highly polarized wave and can be well represented by a scattering matrix, a coherent target decomposition can be used. Some of the main coherent decomposition methods are Kennuagh-Huynen CTD [24, 25], Pauli CTD, Cameron CTD [22] and the Symmetric Scattering Characterization Method (SSCM) [16].

When the scattered wave is partially polarized and there is a high variability in the scattering properties among the different pixels in an area, it is more meaningful to extract information from a pixel-averaged matrix, such as the Stokes, covariance, or coherency matrices. These matrices do not retain the absolute phase information, but the average phase difference between the polarizations is retained. Some of the main non-coherent decomposition methods are: Van Zyl [26], Freeman–Durden [18] and Cloude–Pottier [27]. Chapter 4 will discuss the SSCM, Cameron and Freeman-Durden decomposition methods in more detail, since these methods have been applied in this study.

3.2.3 Some Target Detection Methods

Various developments in the detection of man made targets have been published since the 1960's, and have received noticeable high activity in recent years. Even though a complete survey of methods is not in the scope of this work, some of the most recent ones are mentioned below in an attempt to draw an approximate picture of the state of the art:

- Adaptive Polarimetric Target Detector using a polarimetric Generalized Likelihood Ratio Test (GLRT) [28];
- Sub-aperture coherence detection using the 2L-IHP (two-look internal Hermitian product) algorithm [29];
- Polarimetric Texture Discriminator: a classification scheme based on the polarimetric texture signature [30].

Additional methods that we study in more detail are discussed in Chapter 4.

CHAPTER 4 - METHODOLOGY AND DETECTION ALGORITHMS

4.1 Methodology Used in This Work

There are different algorithms that could help in detecting man made targets. The methodology applied by Lukowski [10] for the detection of crashed airplanes (DCA) uses a combination of three of these algorithms. It has an important application: to assist in search and rescue operations in remote areas by providing coordinates of possible crashed airplanes, with a low false alarm rate.

The DCA methodology was tested in fields with low vegetation (characteristic of many remote areas, as the Canadian prairies and most of the arctic regions) on both serviceable and crashed airplanes. It uses the different responses of targets in polarimetric data to discriminate them from their surroundings.

DCA uses the Polarimetric Whitening Filter (PWF) [11], [12] to reduce the effect of speckle while maintaining the target resolution (see Section 4.2). Its output is an image that no longer holds polarimetric information thus it is not used as input to other algorithms, but shows more clearly the sharp point discontinuities in the clutter. These points are a first set of potential targets, as the airplanes are supposed to have a higher backscatter than the clutter. In order to detect the targets, a constant false alarm rate (CFAR) is imposed, using a threshold dependent on the local variance. The CFAR magnitude is calculated as:

$$y \geq \mu + K\sigma \tag{18}$$

Where y is the intensity value of a pixel, μ is the mean of the intensity image, σ is the variance of the intensity image and K is a parameter used to set the detection threshold for each scene [23].

Another characteristic of crashed airplanes is that they normally retain their tails intact after the fall, and dihedrals are thus the most dominant elemental feature present. As a result, a strong double bounce effect can be expected, and to detect points with a predominant double bounce, the Even Bounce algorithm [13] is used (see Section 4.3). A CFAR threshold is also applied to the algorithm and another set of potential targets is generated.

Besides the Even Bounce algorithm, a double bounce scattering mechanism is also detected by using the Cameron decomposition algorithm (see Section 4.4). This algorithm is applied in order to classify the scatterer responses according to their dominant scatterer type. The scatterer is compared with the responses of six elemental scatterers and mapped in Cameron's unit disc shown in Figure 9. The pixels classified as dihedrals and narrow dihedrals are chosen as potential targets.

Many natural features in the images can have the same signatures as crashed airplanes - tree trunks, for example, can sometimes act as perfect dihedrals. They will typically, however, have fewer pixels than an airplane. Therefore, after applying a detecting algorithm, morphological processes can be employed in order to distinguish false targets from real ones using size and continuity as criteria. In this thesis the morphology processing consists of:

1 – Applying the morphological operator "closing", which encompasses a dilation operation followed by an erosion operation. Here we choose a 2x2 structuring element in order to close a 1-pixel gap between detected pixels.
2 – Eliminating the clusters that are smaller than 3 pixels.

The resulting image is used to calculate the false alarm rate (FAR). FAR is calculated as:

FAR = False Alarms / (False Alarms + Correct Rejections)

The number of false alarms is the number of clusters that were left after the morphology operation minus the target clusters. The FAR unit used in this thesis is the number of targets per km^2.

DCA showed promising results and its potential usefulness in operationally practical situations stimulate questions on what are the limits of this methodology and what possible extensions are there. The motivation of our present work is to address a few of these questions. These are:

- Can we use the DCA methodology to detect other kinds of man made targets and in areas with different vegetation clutters?
- Can the more recently developed Symmetric Scattering Characterization Method (SSCM) algorithm also be used successfully in this task?
- Can a non-coherent decomposition be successfully applied for the detection of man made targets?

In order to find the answers to these questions, we used different datasets (see Chapter 5), in which different types of man made targets are selected. These targets are either surrounded by or lie on the edge of different clutters: sparse, low or high vegetation. Then, the DCA methodology is applied for these different situations and its false alarm rate is assessed.

In addition to the DCA, three other methodologies are proposed, tested and compared. These four methodologies are called here Methodologies 1, 2, 3 and 4 and are explained below. A flow chart for each of these methodologies is shown in Figure 7.

Methodology 1: This is the DCA methodology, which is applied as explained above.

Methodology 2: This is a variation of the Symmetric Scattering Characterization Method (SSCM).

The SSCM algorithm was introduced in 2002 by Touzi and Charbonneau [16], who proposed the use of a coherence test followed by the application of Cameron Decomposition and the mapping of the results into the Poincaré Sphere (shown in Figure 9, in Section 4.5), instead of mapping them into the Cameron's unit disc.

In our work, the Coherence Test algorithm is applied as proposed in the SSCM, but Cameron Decomposition is applied as originally designed and as used in Methodology 1. Therefore, the results are mapped in Cameron's unit disc, which is a classification scheme successfully applied in previous target detection work [19], [20] and [21] .

In Methodology 2 the Coherence Test generates a set of potential targets and Cameron Decomposition is applied on this set of pixels. Then, only dihedrals and narrow dihedrals are selected and the morphology processing is applied as in Methodology 1 to generate the final map of detections. False Alarm Rate is calculated from this map.

Methodology 3: The aim here is to apply a non-coherent target decomposition for detection of man made targets. We apply the Freeman-Durden decomposition that classifies every pixel into one of the three following classes of scattering types - volume scattering, surface scattering and double bounce scattering. This decomposition was chosen for two reasons: first, since it was designed to detect the dihedral scattering generated by ground-trunk interaction, and it is thus reasonable to suppose that it will also detect the dihedrals present in man made targets. Second, this decomposition method calculates the percentage of each scattering mechanism present in each pixel.

In this methodology, the percentage of dihedral scattering yielded by this decomposition is used as a threshold. Thus, even if the dihedral response is not the dominant one for a

particular target, a lower value of the dihedral percentage can still generate a target map where the target is present. The morphology processing is also applied in this methodology and the false alarm rate is assessed.

Methodology 4: This is the intersection of Methodologies 1 and 2, which means that a detection is declared if it appears in Methodology 1 and in Methodology 2. This methodology is expected to be beneficial on high vegetation clutters, when the false alarm rates of Methodologies 1 and 2 can be increased due to the high backscatter response from the tree canopies. Methodology 4 is equivalent to adding the Coherence Test algorithm to the DCA methodology.

The four methodologies above are applied with various thresholds. The chosen thresholds are the ones that keep the false alarm rate to a minimum without erasing the target. For each target the optimal thresholds used in this work are reported in Chapter 6.

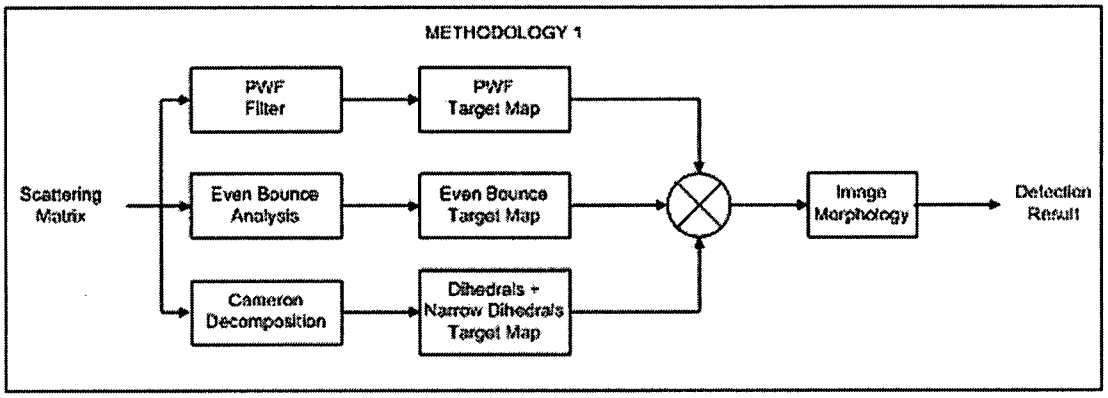

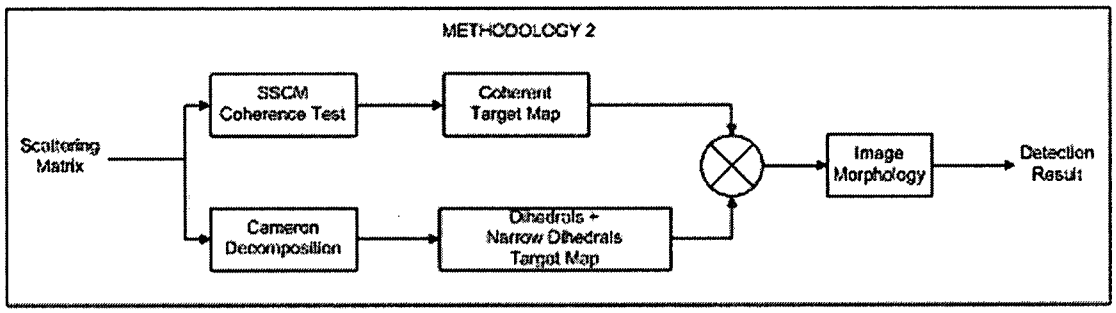

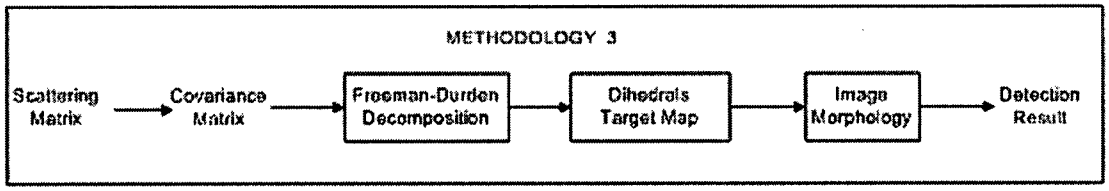

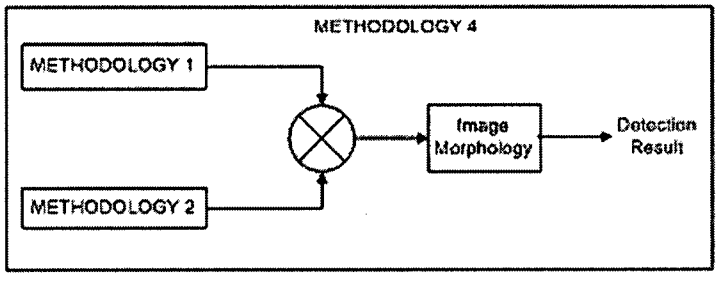

Figure 7: Flow chart of detection algorithms (Methodologies 1 – 4).

4.2 The Polarimetric Whitening Filter (PWF)

4.2.1 Introduction

PWF (Polarimetric Whitening Filter) was developed to reduce the effect of speckle of the natural targets in a Synthetic Aperture Radar (SAR) polarimetric image without affecting its resolution [11].

In the context of man made target detection, the general role of PWF is to enhance the detectability of an individual target in clutter. It can be used in two main ways: the first is to reduce the speckle level thus preparing the image for further processing or image interpretation. Secondly, it can also be used directly as a target discriminator. As every speckle filter, PWF can lead to loss of information, and this is a negative point to be considered when using it for speckle noise reduction.

The DCA methodology [10] for target detection uses the filter for the second aim mentioned above. PWF is used as a discriminator and the results form a set of potential targets, instead of a filtered image for further processing. These targets will be later cross-checked against other methods used in the detection process.

In the DCA methodology a Constant False Alarm Rate (CFAR) detector is applied to an image, using a threshold experimentally determined to generate an initial set of targets. These targets will not only be man made targets, but it is expected that man made targets will be among the ones detected due to the high target-to-clutter ratio they typically present. This part of Lukowski's methodology uses PWF as Novak proposed in 1993 [10], [12]. Novak also proposed the Multilook Polarimetric Whitening Filter (MPWF) and its adaptive version (AMPWF). These filters are not adopted here, because we only use single look complex (SLC) data.

4.2.2 Speckle and Polarimetric Speckle Filtering

Radar imaging systems are of the coherent type, where the phases of the transmitted and received signals are carefully recorded. The return signal from one resolution cell on the ground is the result of the vector addition of reflections from all the scatterers within that resolution cell. Even if adjacent cells on the ground visually appear to be very similar, the signal from their components may combine to result in completely different backscatter. This variation in backscatter for otherwise similar scatterers is known as speckle.

Polarimetric speckle filtering is a technique that could be applied to the original radar image for reducing image speckle while preserving spatial resolution, after the image is formed. It uses the three complex channels (HH, HV, VV) to reduce the speckle.

4.2.3 Mathematical Description

The purpose of the PWF filter is to process the three channels HH, HV and VV in order to obtain an intensity image with the minimum amount of speckle.

As reported above, the area chosen is homogeneous, and thus can be characterized by a complex Gaussian clutter model. This means that the expected returns HH, HV and VV can be expressed by a covariance matrix of the form:

$$\Sigma_c = \sigma_{HH} \begin{bmatrix} 1 & 0 & \rho^* \sqrt{\gamma} \\ 0 & \varepsilon & 0 \\ \rho^* \sqrt{\gamma} & 0 & \gamma \end{bmatrix} \tag{19}$$

where

$\sigma_{HH} = E\{|HH|^2\}$ is the HH power,

$$\varepsilon = \frac{E\{|HV|^2\}}{E\{|HH|^2\}} \text{ is the cross-pol ratio,}$$

$$\gamma = \frac{E\{|VV|^2\}}{E\{|HH|^2\}} \text{ is the co-pol ratio and} \tag{20}$$

$$\rho = \frac{E\{HH.VV^*\}}{\sqrt{E\{|HH|^2\}E\{|VV|^2\}}} \text{ is the complex correlation.}$$

We want to find the optimal single channel (or b/w) image from HH, HV and VV. The parameter used to measure the noise (speckle) reduction performance will be σ/μ, which is the ratio of the standard deviation of the pixel to mean of intensities:

$$\frac{\sigma}{\mu} = \frac{st.dev\{y\}}{E\{y\}} \tag{21}$$

where y is pixel intensity in the filtered image.

Now, considering X = [HH, HV, VV] (complex elements), we want to find a weighting matrix A that results in an image $y = X^{\dagger}AX$ whose σ/μ ratio is minimal. Let

$$\begin{aligned} E\{y\} &= tr(\Sigma_c A) = \sum_{i=1}^{3} \lambda_i \\ \text{var}\{y\} &= tr(\Sigma_c A)^2 = \sum_{i=1}^{3} \lambda_i^{\,2} \end{aligned} \tag{22}$$

where λ_1, λ_2 and λ_3 are the eigenvalues of the matrix $\Sigma_c A$. Thus, we want A such that σ/μ will be minimum. From the above we can derive σ/μ as

$$\frac{\sigma}{\mu} = \frac{\sqrt{\sum_{i=1}^{3} \lambda_i^2}}{\sum_{i=1}^{3} \lambda_i} \tag{23}$$

A is called the *whitening* filter, or PWF. It should have equal values for its eigenvalues, and thus the minimum-speckle image is:

$$y = X^{\dagger} \Sigma_c^{-1} X \tag{24}$$

This takes us back to the covariance matrix of the clutter given in (19). The solution y, considering the covariance matrix (19), is:

$$\begin{aligned} y \;=\; & \frac{|HH|^2}{\sigma_{HH}\left(1-|\rho|^2\right)} + \frac{|VV|^2}{\sigma_{HH}\left(1-|\rho|^2\right)\gamma} + \frac{|HV|^2}{\sigma_{HH}\varepsilon} \\ & - \frac{2|\rho|}{\sigma_{HH}\left(1-|\rho|^2\right)\sqrt{\gamma}} |HH||VV| \cos\left(\phi_{HH} - \phi_{VV} - \phi_{\rho}\right) \end{aligned} \tag{25}$$

4.3 Even Bounce Analysis

Even bounce analysis can contribute as a discriminator to the detection of man made targets. This is because the dihedrals normally present in those targets provide strong double bounces (see Figure 4). While few dihedral structures exist in natural clutter, natural clutter tends to exhibit more odd-bounce reflected energy than even-bounce reflected energy.

The double bounce scattering mechanism creates a 180° phase shift between the HH and VV polarizations [13], and the following relation gives the strength of the even bounce scattering:

$$E_{even} = \frac{|S_{hh} - S_{vv}|^2}{2} + 2|S_{hv}|^2 \tag{26}$$

In this work an even bounce image (example shown in Figure 8) is created using equation (26), and a CFAR (explained in Section 4.1) can be applied to this image in order to generate an even bounce bright target map. A man made target stands out and can be detected by applying a CFAR to the Even Bounce image.

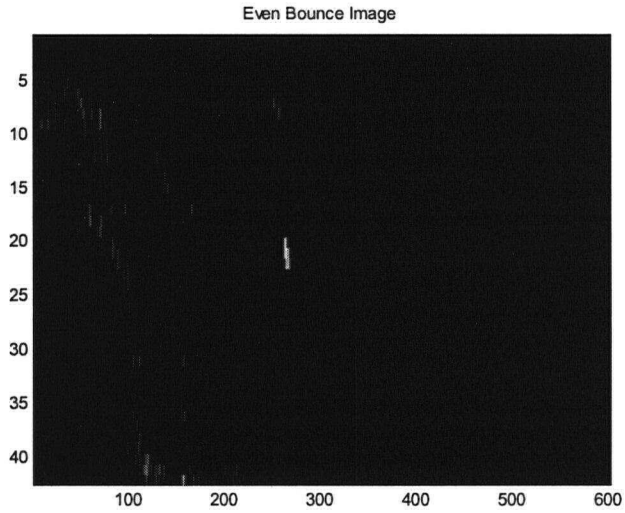

Figure 8: Even Bounce image of Target 1 (see section 6.2).

4.4 Cameron Decomposition

The Cameron decomposition detects an elemental scatterer based on the physical scattering mechanism associated with the image backscatter, thus providing information about the structure of the scatterers. This method is based on two assumed properties of radar targets: *symmetry* and *reciprocity*. Symmetric scatterers have an axis of symmetry in the plane orthogonal to the line of sight (LOS) of the radar.

In monostatic radar the transmitting and receiving antennas can be considered as being in the same position, and therefore every target can be considered reciprocal – having thus the orthogonal elements of its scattering matrix equal to each other:

$$S_{hv} = S_{vh} \tag{27}$$

Given the scattering matrix S, its vector form can be expressed as

$$\vec{S} = \begin{bmatrix} S_{hh} \\ S_{hv} \\ S_{vh} \\ S_{vv} \end{bmatrix} \tag{28}$$

$\vec{S}$ can also be represented in terms of Pauli spin matrices as

$$\vec{S} = \alpha \vec{S}_a + \beta \vec{S}_b + \delta \vec{S}_c \tag{29}$$

where α, β and γ are the Pauli components given as follows:

$$\alpha = \frac{S_{hh} + S_{vv}}{\sqrt{2}} \tag{30}$$

$$\beta = \frac{S_{hh} - S_{vv}}{\sqrt{2}} \tag{31}$$

$$\gamma = \sqrt{2} S_{hv} \text{ (reciprocal case)} \tag{32}$$

According to Cameron, a reciprocal target can be expressed as the sum of two components:

$$\vec{S} = A[\cos\tau \, \vec{S}_{sym}^{\max} + \sin\tau \, \vec{S}_{sym}^{\min}] \tag{33}$$

where:

$\vec{S}_{sym}^{\max}$ is the maximum symmetric component;

$\vec{S}_{sym}^{\min}$ is the minimum symmetric component;

$\cos\tau$ is the degree of symmetry, measuring how far $\vec{S}$ is from $\vec{S}_{sym}^{\min}$; and

$$A = \left\| \vec{S} \right\| \tag{34}$$

$$\vec{S}_{sym}^{\max} = \alpha \vec{S}_a + \varepsilon \vec{S}_b \tag{35}$$

$$\varepsilon = \beta \cos\theta + \delta \sin\theta \tag{36}$$

$$\tan 2\theta = \beta\gamma^* + \beta^*\delta / (|\beta|^2 - |\delta|^2) \tag{37}$$

An arbitrary symmetric scatterer can be decomposed according to:

$$\vec{S}_{sym} = a e^{j\rho} [R(\psi)] \hat{\Lambda}(z) \tag{38}$$

Where a is the amplitude of the scattering matrix, ρ is the nuissance phase and ψ is the scatterer orientation angle. The matrix $[R(\psi)]$ denotes the rotation operator and $\hat{\Lambda}(z)$ is given by

$$\hat{\Lambda}(z) = \frac{1}{\sqrt{1+|z|^2}} \begin{pmatrix} 1 \\ 0 \\ 0 \\ z \end{pmatrix} \tag{39}$$

The purpose of the decomposition is to find the value of the scattering type parameter (z) for a given pixel; this is because each elemental scatterer has its z value, and the classification proposed by Cameron compares the scattering matrix with those of the elemental scatterers (Table 1). In order to find scattering type parameter the value of z is plotted in the Symmetric Scatterer Unit Disc (Figure 9).

The classification of the pixels is performed by calculating the distance between z for each pixel and the z_{ref} of each of the primitive scatterers: Trihedral, dihedral, dipole, cylinder, narrow diplane, quarter wave device. Table 1 shows the value of z_{ref} for each of these scatterers.

Target	SM	Z
Trihedral	$\begin{pmatrix} 1 & 0 \\ 0 & 1 \end{pmatrix}$	1
Dihedral	$\begin{pmatrix} 1 & 0 \\ 0 & -1 \end{pmatrix}$	-1
Dipole	$\begin{pmatrix} 1 & 0 \\ 0 & 0 \end{pmatrix}$	0
Cylinder	$\begin{pmatrix} 1 & 0 \\ 0 & 0.5 \end{pmatrix}$	0.5
Narrow Diplane	$\begin{pmatrix} 1 & 0 \\ 0 & -0.5 \end{pmatrix}$	-0.5
Quarter Wave	$\begin{pmatrix} 1 & 0 \\ 0 & i \end{pmatrix}$	i

Table 3: z values for the elemental scatterers and their scattering matrices.

Finally, the following relation gives the distance from a given pixel's z value to the elemental scatterer's z_{ref}. This distance will tell how close they are from each other

$$d(z, z_{ref}) = \cos^{-1}\left(\frac{\left|1 + z^* z_{ref}\right|}{\sqrt{1+|z|^2}\sqrt{1+|z_{ref}|^2}} \right) \tag{40}$$

and which one is the closest elemental scatterer.

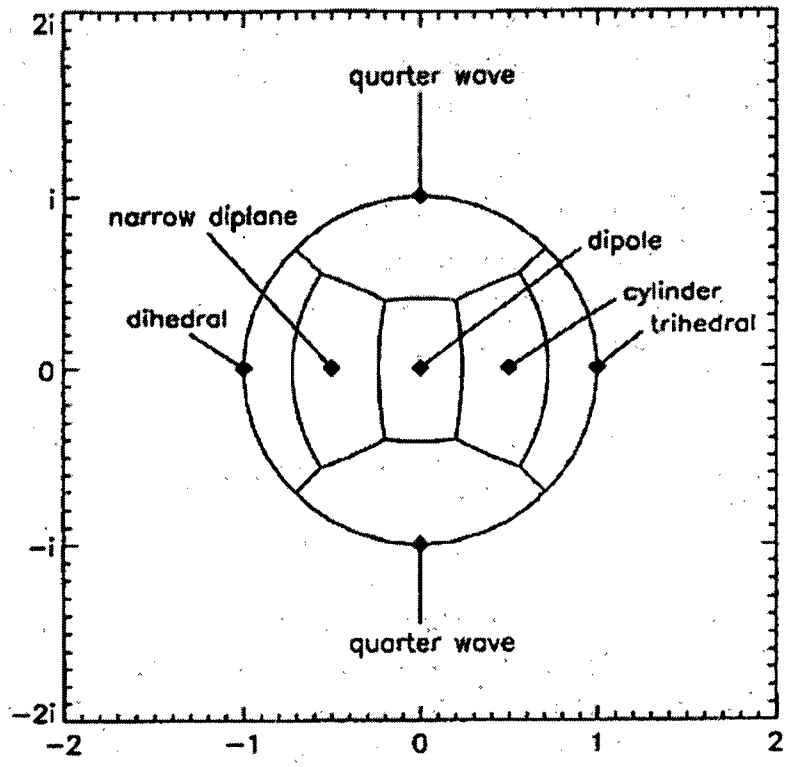

Figure 9: Cameron's unit disc. Adapted from Cameron *et al.* [22].

4.5 The Coherence Test of the Symmetric Scattering Characterization Method (SSCM)

The SSCM is an extension of Cameron decomposition for symmetric coherent scatterers. It employs the maximum symmetric component $\vec{S}_{sym}^{\max}$ of the scattering matrix as used by Cameron. The SSCM scheme includes the following steps:

- Calculation of the parameters α and ε (as in Cameron decomposition, Section 4.4);
- Classification of target scattering as coherent or non coherent, using the degree of coherence (equation 41) and the Rician threshold [16]. Rician Threshold is a threshold based on the Rician distribution of clutter;
- Classification of coherent scatterers using Cameron decomposition and mapping the results in the Poincare Sphere (Figure 10).

The Poincare Sphere is illustrated in this section in order to provide a complete overview of the SSCM method. Nevertheless, in this thesis, only the Coherence Test of the SSCM will be used.

The degree of coherence p_{sym} of a target is calculated as follows:

$$p_{sym} = \frac{\sqrt{\left(\left\langle |\alpha|^2 - |\beta|^2 \right\rangle\right)^2 + 4\left|\left\langle \alpha.\beta^* \right\rangle\right|^2}}{\left\langle |\alpha|^2 + |\beta|^2 \right\rangle} \tag{41}$$

The degree of coherence p_{sym} separates coherent from partially coherent scattering targets. This classification is important, as the SSCM will try to characterize only the coherent targets. This characterization is done by mapping the scatterers into one half of the Poincaré sphere. This provides a higher resolution mapping, according to the authors, than the Cameron's unit disc.

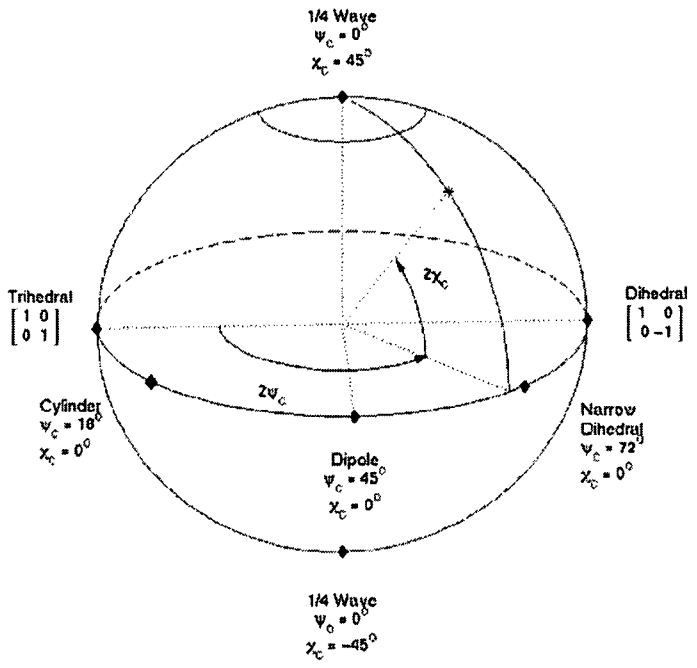

Figure 10: Poincaré Sphere.

4.6 The Freeman-Durden Decomposition

The Freeman-Durden decomposition models the covariance matrix as the contribution of three different scattering mechanisms:

1. Surface scattering – or single bounce scattering;

2. Double bounce scattering, modelled by a dihedral mechanism;

3. Volume scattering from a cloud of randomly oriented dipoles, which is typical from a canopy scatterer.

An illustration of these scattering mechanisms can be seen in Figure 4 (Section 2.2.2).

In detection of man made targets, the purpose of using the Freeman-Durden decomposition is to assess how effective it is in identifying double bounce scattering originated from corners in a physical structure.

For each pixel, Freeman-Durden decomposition calculates the percentage of each of the three scattering mechanisms described above. The pixel is assigned to the image that corresponds to the dominant scattering mechanism.

Before applying this technique on real data we have performed the following test: typical dihedral and surface scattering matrices were simulated and added in a rectangle (no volume contribution was added). After that, Gaussian noise was added to the whole image, including the rectangle. Finally, Freeman-Durden decomposition was applied.

Figure 11 shows the results for four different percentage values of dihedral and surface scattering. The percentage of dihedral varies from 100% to 40%, while the percentage of surface varies from 0% to 60%. The results show that the algorithm tends to classify the pixels correctly, but the presence of noise causes many pixels to be classified as volume-dominated scatterers.

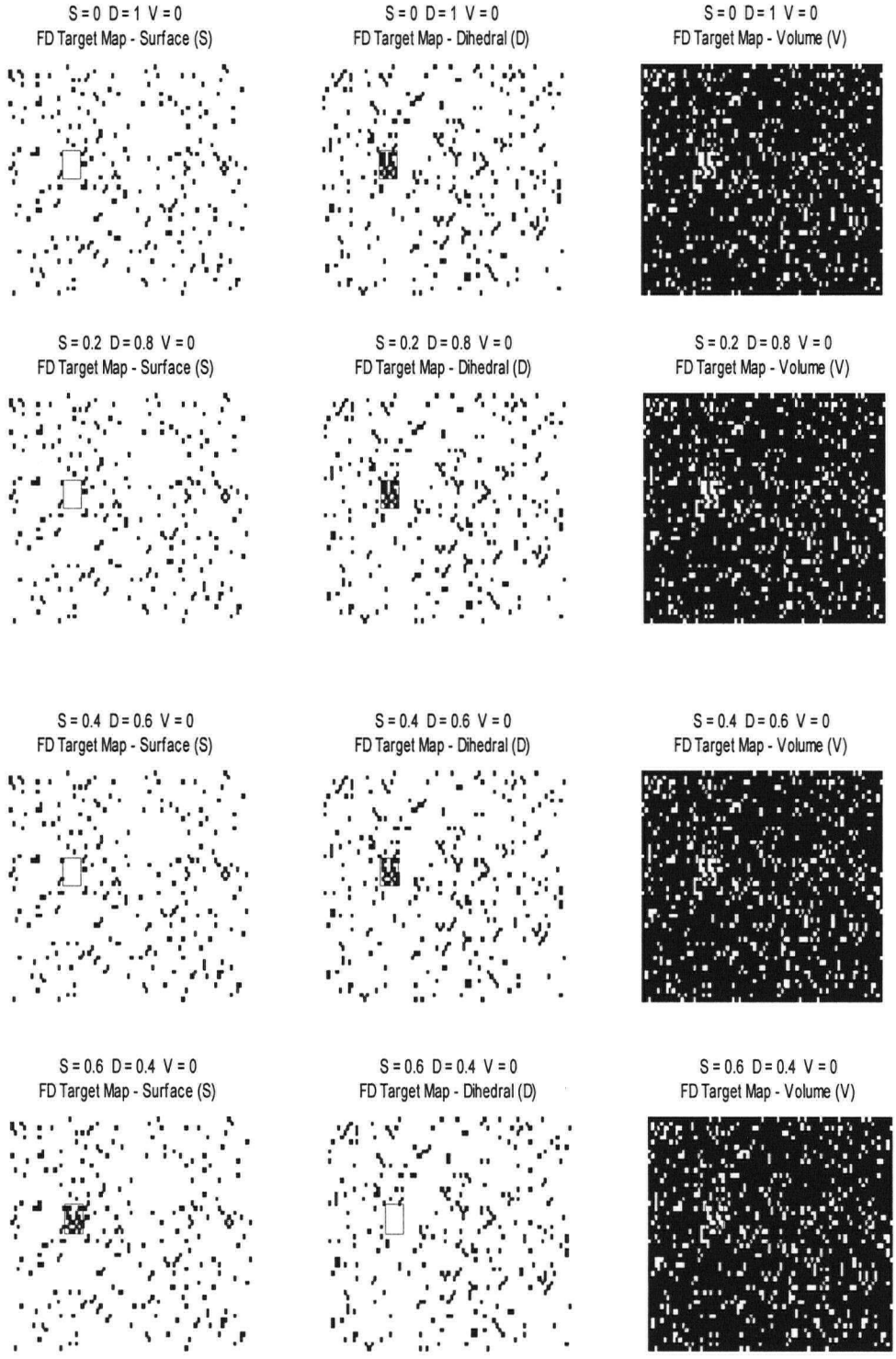

Figure 11: Freeman-Durden decomposition applied to simulated images.

CHAPTER 5 - DATASETS

This chapter describes the three datasets used in the experiments in this work. These are the Ottawa dataset (2002), the Westham Island dataset (2004) and the Gagetown dataset (2001). The descriptions will also include the ground reference data collected for each of the datasets. The ground reference data are used to validate the experimental results. The photographs of the specific targets selected for the experiments in this work will be shown in Chapter 6, along with the processing results.

All the datasets are fully polarimetric and were acquired by the Convair-580 (CV-580) SAR airplane (Figure 12), which was originally developed, owned and operated by the Canada Centre for Remote Sensing (CCRS), and later transferred to Environment Canada [15]. The data are processed by MDA's Geospatial Solutions at the Canadian Data Processing Facility (CDPF) at Gatineau (Quebec). The CV-580 specifications and data format are described at the end of this chapter.

Figure 12: The Convair 580 SAR airplane (Source: CCRS, 2002)

5.1 Datasets Used

5.1.1 The Ottawa Dataset

The first dataset is acquired from an area to the northwest of Ottawa (ON, Canada), where a controlled experiment was carried out by a group from the Canada Centre for Remote Sensing (CCRS), to test their methodology to detect crashed airplanes [10]. In this thesis part of the data is used. It covers a grass field where a single target was placed along with corner reflectors for data calibration. In this work, these data are used both as a check for the methodology implementation and as a first test for the comparison of algorithms performances proposed here. The data was acquired by the CV-580 radar system on June 25th, 2002.

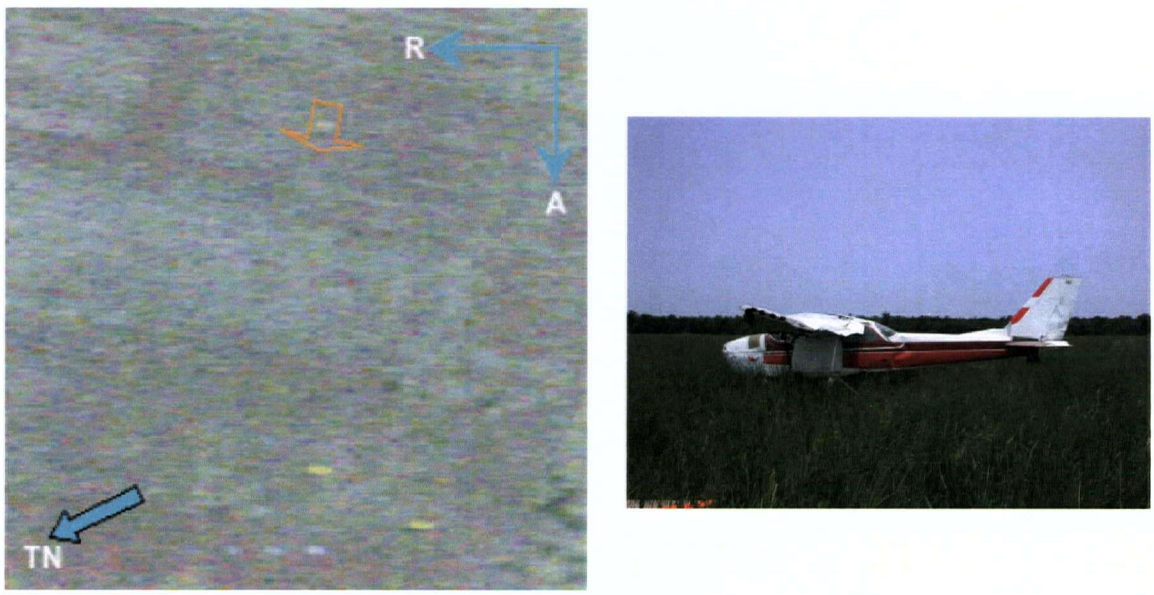

Figure 13: Overview of the Ottawa dataset and photograph of the crashed airplane. **Left:** (HH, red; VV, green; HV, blue). Orange arrow shows the orientation of the airplane, and blue arrows indicate azimuth (A), range (R), and true north (TN). **Right:** Photograph of the crashed airplane. (Source: Lukowski *et al.* [10]).

5.1.1.1 Ground Reference Data From Ottawa

For the experiments in Ottawa a previously crashed airplane was placed on a grass field in order to simulate a real crash of a small aircraft on a low, uniform vegetation. The corner reflectors and Active Radar Calibrators were also placed nearby and were used for data calibration.

5.1.2 The Westham Island Dataset

The second dataset covers Westham Island, a very flat island south of Vancouver (BC, Canada). The island's land cover is mostly composed of agricultural fields, with a few houses and machinery spread along the roads. The island's borders used to be flooded by the tide. This effect was avoided in the crop fields by the construction, years ago, of a ditch surrounding the island. On the north and northwest sides there are forested areas and swamps. Many migratory birds populate this area for part of the year. The area is located between 123° 07' 47''W and 123° 11' 36"W in the E-W direction and between 49° 04' 13"N and 49° 06' 40"N in the N-S direction.

Figure 14: Overview of Westham Island. HH – Red, HV – Green and VV – Blue.

This data was collected and processed for the UBC Radar Remote Sensing Group (RRSG) as part of a larger acquisition campaign on September 30, 2004. The data swath extends up to the city of North Vancouver.

5.1.2.1 Ground Reference Data from Westham Island

The ground data for the Westham Island dataset comprises ground photographs taken by members of the RRSG (UBC) during two fieldwork trips to the island. The first trip took place on September 28th 2004 – two days before the acquisition date – with the purpose of making an overall examination of the terrain and its potential targets. Accessibility was checked and some photographs of fixed targets were taken.

The second field trip took place on the acquisition date (September 30th), and other targets were photographed. The photos were taken over approximately 2 hours. The CV-580 airplane was flying over the area (between 11:00am and 1:00pm, local time). Parked machinery, wreckage, buildings, boats and other relevant man made targets were included in the photographs and GPS readings were taken. Due to the almost total absence of forests in the island, few targets are located within of high vegetation clutters.

High resolution optical data available online were also used in this work as complementary reference information on the ground features. These data are a mosaic of images acquired between March 10th, 2004 and September 19th, 2004, and were helpful in identifying non-movable targets seen in the radar data.

5.1.3 The Gagetown Dataset

The third dataset was acquired on September 11th, 2001, over Gagetown (NB, Canada). It was acquired for Radarsat International (now MDA's Geospatial Services), who provided the UBC RRSG with a copy for research purposes. Most of the area includes the Canadian Forces Base (CFB) Gagetown, which has low buildings, military vehicles, training ranges and a residential area. The Fredericton airport is on the NW corner of the imaged area, the Saint John river is on the north edge and forests, ponds and low vegetation fields cover the rest of the image. The area is approximately 16 km (W/E direction) X 8 km (N/S direction) and is located between 66° 20' 17''W and 66° 34' 00"W in the E-W direction and between 45° 27' 20"N and 45° 53' 00"N in the N-S direction.

Figure 15: Overview of Gagetown data.

5.1.3.1 Ground Reference Data from Gagetown

Two field campaigns were performed to collect ground truth data at selected sites in the Gagetown area by Aerde Environmental Research Inc. The first one took place on September 10, 2001, which was one day before the acquisition date. This fieldwork generated 16 ground photos of different targets lying both inside and outside CFB Gagetown.

The SAR data were processed in 2002, and visual analysis showed the need for more ground truth. Based on the radar responses seen in the image and auxiliary information (both from a 1:50,000 map) and a high resolution Ikonos image, specific targets were selected for a second fieldwork. Most of these targets were man made targets such as public monuments, fixed artillery pieces for display and buildings. This fieldwork took place on November 27, 2002, and around 70 photographs were taken of the targets – except those that presented access problems.

Figure 16: Ikonos image acquired on Oct 4th, 2001 over Gagetown.

An Ikonos image was acquired over part of the area on Oct 4th, 2001 (23 days after the CV-580 acquisition date) and was used in this work to identify larger targets of interest in the

area. A RADARSAT-1 Fine beam mode (10 meters resolution) image was acquired on the same day as the CV-580 SAR data were acquired and is part of the reference data.

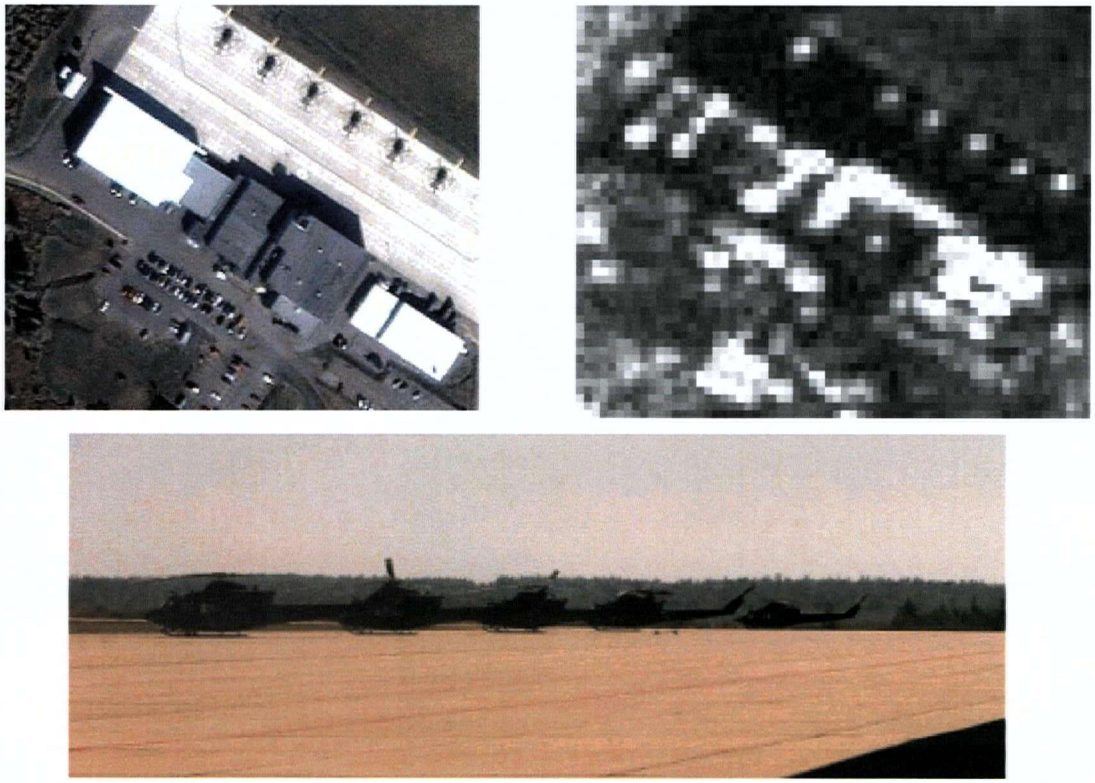

Figure 17: Ikonos, CV-580 data and photograph of Gagetown data. **Top left:** Detail of Ikonos image (Oct. 4th, 2001) used as auxiliary ground reference data showing helicopters in the CFB Gagetown. **Top right:** Enlarged detail of VV channel of CV-580 data (Sept. 11th, 2001) of the same area. **Bottom:** Photograph showing the helicopters. Notice that, due to the difference in acquisition dates, the helicopters are not in the same positions in the images.

5.2 CV-580 SAR System Specifications and Data

5.2.1 The CV-580 SAR System

All the data used in this work were acquired by the CV-580 SAR system. This airborne system was developed by the Canada Centre for Remote Sensing (CCRS) of Natural Resources Canada, and in 1996 transferred to Environment Canada (EC). The system can

produce both interferometric and polarimetric data, in both X-band (not polarimetric) and C-band, and the data used in this work are fully polarimetric C-band data.

Figure 18: Tail section of Convair –580 showing SAR radomes. (Source: CCRS, 2002).

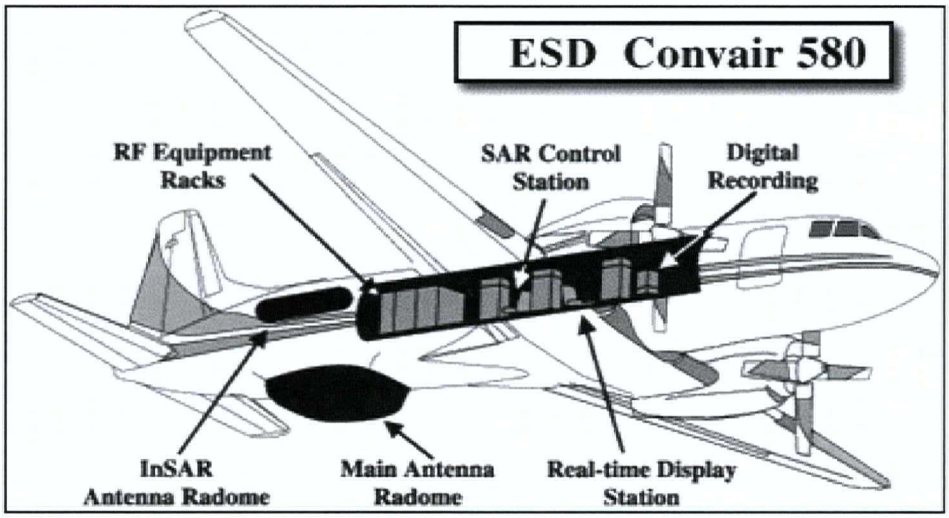

Figure 19: Convair System configuration (Source: CCRS, 2002).

5.2.2 Data Format

The raw data received during acquisition were transcribed to a computer compatible format. After a large set of processing stages, the four channels of complex polarimetric data are generated. Following the focusing and calibration of the data, two main classes of files are generated: (1) The PolGASP (output from the Polarimetric Generalized Airborne SAR Processor); and (2) The SIR-C data format [15].

The SIR-C format is provided with equal range and azimuth resolutions, and is used to generate geocoded imagery in a compressed format. The PolGASP format, which is used in this work, carries Single Look Complex (SLC), floating point data, and its extension is .img. Each file carries one of the four polarizations (HH, HV, VH and VV) and is accompanied by a header ASCII file (.hdr extension). The addition of a master header file that contains the general information about the four polarization headers makes a total of nine files per data.

The binary data were written on a SGI machine, in big-endian format (i.e., byte swapped compared to a PC). This should be considered by the routine used to read the data into Matlab.

POLSAR single look complex (SLC) data have different resolutions in azimuth and range. This is because in radar imaging these resolutions depend on different parameters. The range resolution depends on the chirp bandwidth, and the azimuth resolution depends on system parameters such as the antenna length and the fraction of the Doppler bandwidth processed.

CHAPTER 6 - DATA PROCESSING RESULTS AND ANALYSIS

6.1 Selected Targets

The targets for this work were selected from both the Westham Island and Gagetown datasets, and one target in the Ottawa dataset where a crashed airplane was intentionally placed in the scene (see Chapter 5).

The following two criteria were kept in mind during the selection of these data: targets should be surrounded by different backgrounds (bare soil, low, medium and high vegetation) and should be typically man made ones, as defined in Section 3.1.

This task was completed by analyzing both the photographs taken in the fieldwork trips and the Ikonos image. Table 4 describes the targets, the clutter type and their location. Coordinates are given in WGS-84 datum. In Figure 20, photographs or optical satellite images of the targets are presented.

Target	Target description	Clutter type	Coordinates (WGS 84 Datum) and Dataset
1	Two cylindrical steel containers	Forest + wheat field	49° 05' 49"N / 123° 09' 51"W Westham Island
2	Agricultural plowing machine	Low grass + bare soil	49° 05' 02"N / 123° 08' 20"W Westham Island
4	Cart beside a 10 metre high tree	Low grass	49° 05' 14"N / 123° 08' 25"W Westham Island
5	Two steel cylinders (water tanks) on stands	Corn field	49° 05' 42"N / 123° 08' 45"W Westham Island
7	Large house surrounded by trees	Broccoli field	49° 05' 33"N / 123° 09' 59"W Westham Island
12	Artillery pieces	Low grass	45° 50' 25"N / 66° 27' 59"W Gagetown
14	House	Forest	45° 52' 37"N / 66° 32' 17"W Gagetown
21	House	Forest	45° 51' 59"N / 66° 28' 13"W Gagetown
20	Crashed airplane	Medium grass	Ottawa

Table 4: Target and clutter descriptions and locations.

Target 1

Target 2

Target 4

Target 5

Target 7

Target 12

Target 14

Target 21

Target 20

Figure 20: Photos and images of the 9 targets selected for this work.

6.2 Results

The methodologies described in Chapter 4 have been applied to images containing the targets and an area of clutter. The images are all sub-images from the original datasets and were cropped in the largest possible area of homogeneous clutter along with the target. Roads, fences, poles and other man made features were kept out of the scenes in order to avoid scene complexity and keep only one target in each image.

In our study we are mainly concerned with the detection of the targets and decrease of the number of false alarms. In order to achieve that, various thresholds were applied for each algorithm. The detection results are obtained by applying the thresholds that yield the lowest false alarm rates while still keeping at least three connected pixels of the target. These thresholds are considered the optimal thresholds for that particular target and clutter. Detections containing one or two pixels cannot be considered as targets or as false alarms. The valid targets are highlighted within ellipses in the various detection results shown in the figures in this chapter.

For each target, a description of both target and clutter is provided, followed by graphical and numerical results. For clarity, full results for Targets 7, 14 and 21 are shown in this chapter. Final detection results for Targets 1, 2, 4, 5, 12 and 20 are also shown in this chapter, and plots showing intermediate processing results for these targets are shown in Appendix A.

The methodologies are applied as follows:

Methodology 1:

The Polarimetric Whitening Filter (PWF) and the Even Bounce (EB) algorithm were each applied to the original image, generating a PWF processed image and an Even Bounce processed image. Different Constant False Alarm Rate (CFAR) values (represented by the constant K, as explained in Section 4.1) were applied to the PWF and to the Even Bounce

images. The optimal thresholds are determined and used to generate both the PWF target map and the Even Bounce target map. A mask was created for each of these two target maps and Cameron decomposition was applied to both masks. After that, only dihedrals and narrow dihedrals were selected.

The intersection between the results above resulted in a target map to which the morphological processing was applied, as explained in Section 4.1. The intersection is an "AND" operator, and selects only the pixels that are detected in both images. The resulting target map was the detection map, from which the false alarm rate was calculated.

Methodology 2:

The Coherence Test procedure from the SSCM algorithm was applied to the original image. Various degree of coherency and Rician threshold values were applied. The Coherence Test target map was generated by applying the optimal degree of coherence and Rician thresholds. Cameron decomposition was applied to this target map and only the pixels classified as dihedrals and narrow dihedrals were kept. Morphological processing was applied to the resulting map in order to generate the detection map, from which the false alarm rate was calculated

Methodology 3:

The Freeman-Durden decomposition was applied to the original image. Various dihedral percentage threshold values were applied to the dihedral scattering image, generating a target map. Morphological processing was applied to the resulting map in order to generate the detection map, from which the false alarm rate was calculated.

Methodology 4:

The detection maps resulting from Methodologies 1 and 2 were cross-checked (only those targets appearing in both detection maps were retained). If the number of connected pixels from the target in the resulting image was larger than three, the target was considered to be

retained. Otherwise, Methodologies 1 and 2 were applied again with different thresholds until the target was retained. When the target was finally retained, morphological processing was applied and the final detection map was generated. After that, the false alarm rate was calculated.

6.2.1 Results for Target 7 (House Among Trees)

6.2.1.1 Target Description

Target 7 is a house surrounded by trees in its immediate vicinity. The clutter is a broccoli field.

Figure 21: Target 7 - RGB composite and photograph. **Left:** Colour composite image (HH – Red, HV – Green, VV – Blue) showing Target 7 (in the ellipse) and the surrounding ground. **Right:** Target 7 photograph.

Analysis:

Methodology 1 generated one false alarm close to the house (see Figure 22). This can be due to the high scattering from the large tree or, more likely, to a vehicle parked close to this tree.

In Methodology 2 the Coherence Test detected many pixels on the house (see Figure 24) as well as in the broccoli field.

Results from both Methodologies 1 and 2 show that, although the PWF, Even Bounce and Coherence Test could detect most pixels of the house, Cameron Decomposition identified very few of these as dihedrals. This may be due to the roof causing a strong surface scattering, which Cameron would classify as trihedral. Also, these three algorithms detected part of the trees that surround the house as targets, while Cameron decomposition did not. This kept the trees from being confused with the house, although they are very close and present a high backscatter.

Methodology 3 detected the house with a considerably lower false alarm rate than it did in the other targets. Freeman-Durden decomposition calculated a high percentage of dihedral in the house scattering. This allowed us to use for this image the highest threshold value for a target in this work (dihedral percentage > 94%). This caused the drop in the false alarm rate, although it had still the highest false alarm rate among the four methodologies. Methodology 4 detected the target without incorrect detections.

	Methodology 1	Methodology 2	Methodology 3	Methodology 4
False Alarm count	1	7	10	0
False Alarm Rate	20	146	209	0

Table 5: Target 7 - False Alarm count and False Alarm Rate (false alarms/km^2)

6.2.1.2 Processing Results for Target 7

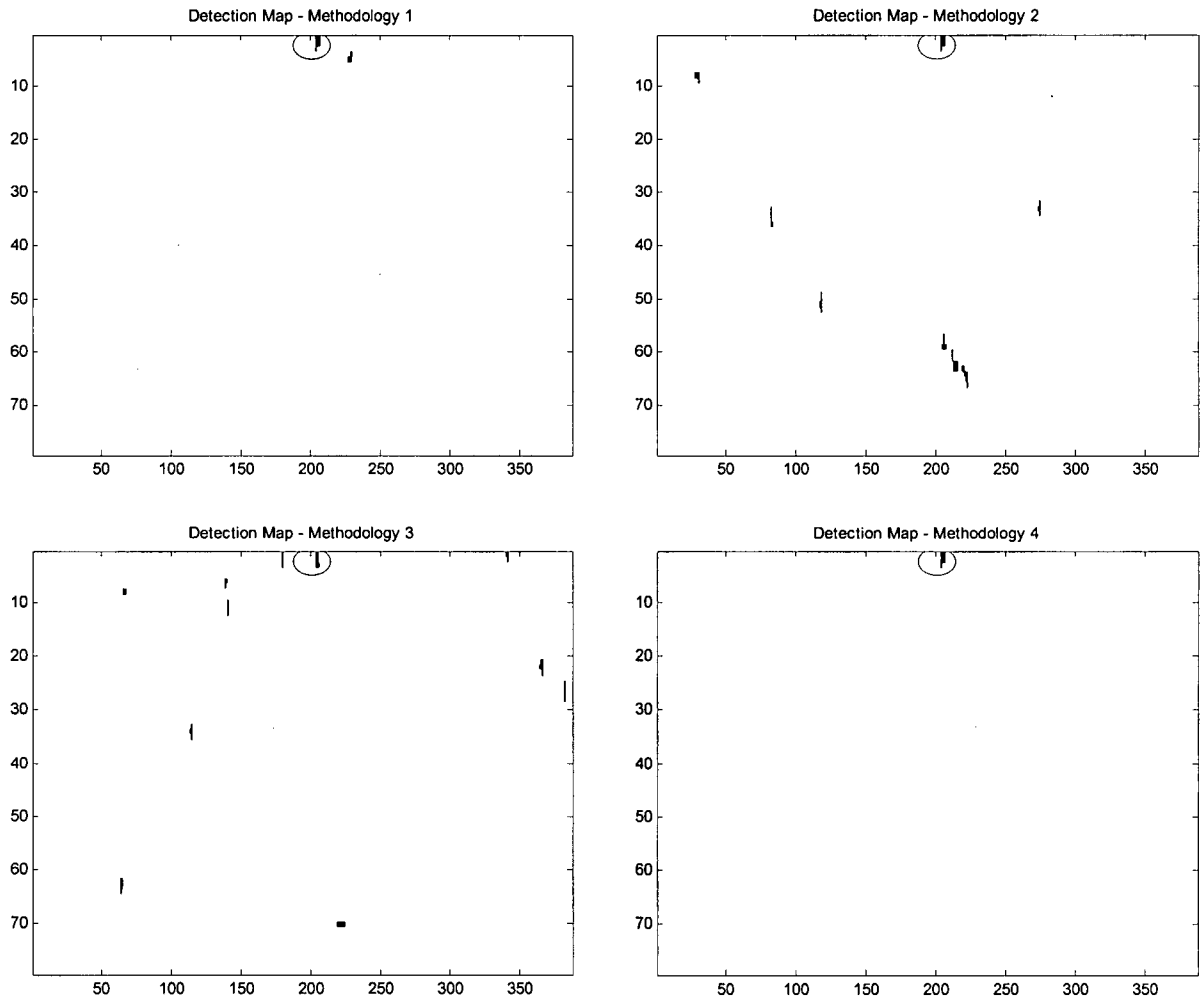

Figure 22: Target 7 - Final detection maps for Methodologies 1 to 4.

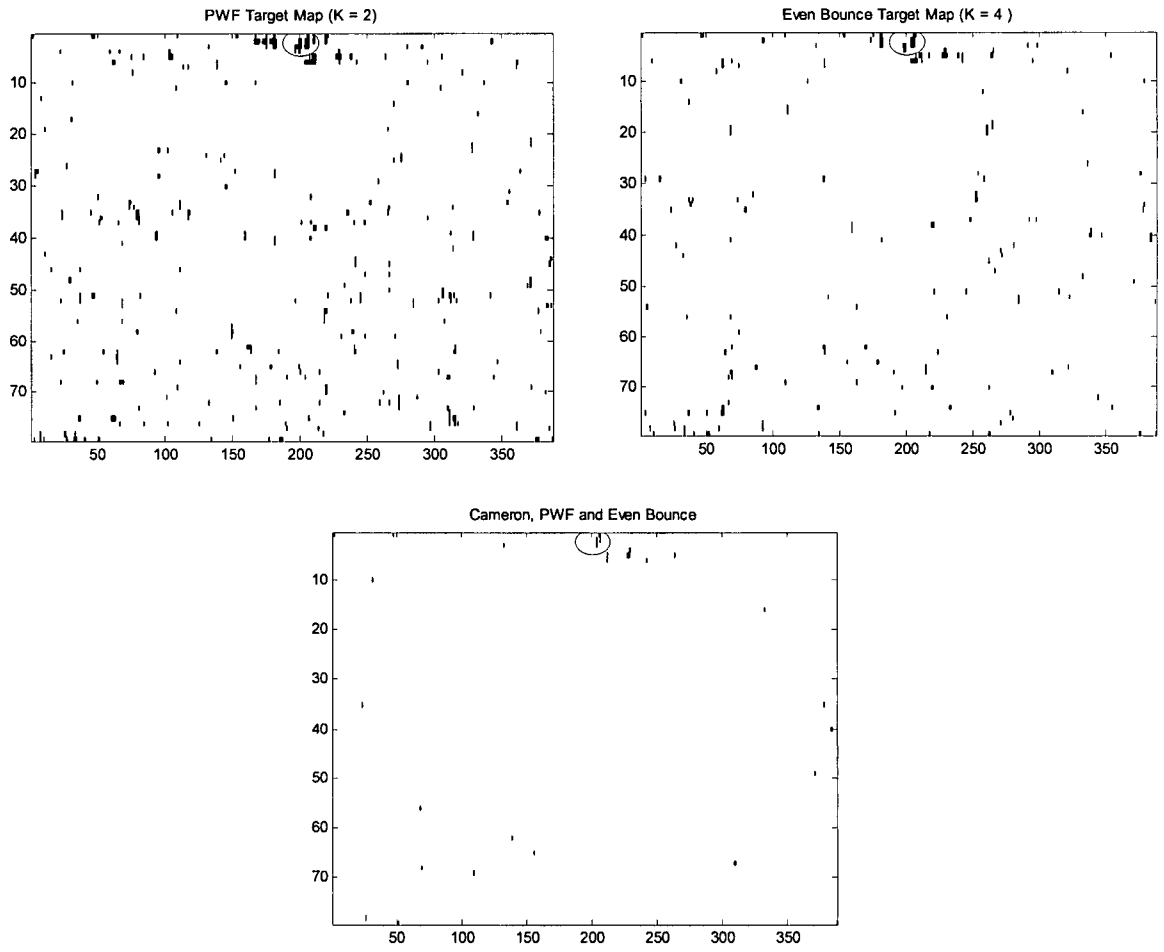

Figure 23: Target 7 - Plots from Methodology 1. Upper left: PWF target map. Upper right: Even Bounce target map. Bottom: combined result of Cameron (dihedrals plus narrow dihedrals), PWF and Even Bounce. K is the CFAR constant.

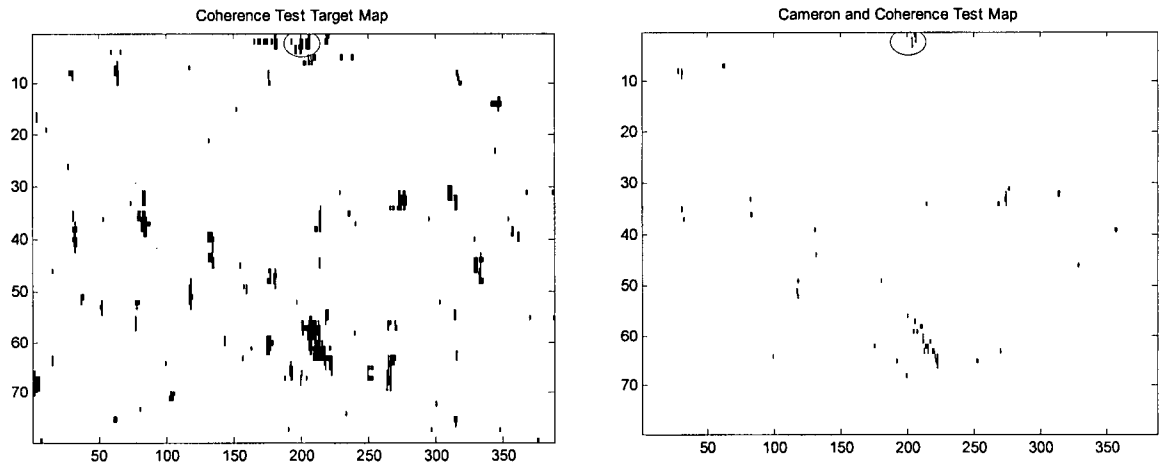

(a) (b)

Figure 24: Target 7 - Plots from Methodology 2. (a) Coherence Test target map. (b) Combined result of Cameron (dihedrals plus narrow dihedrals) and Coherence Test.

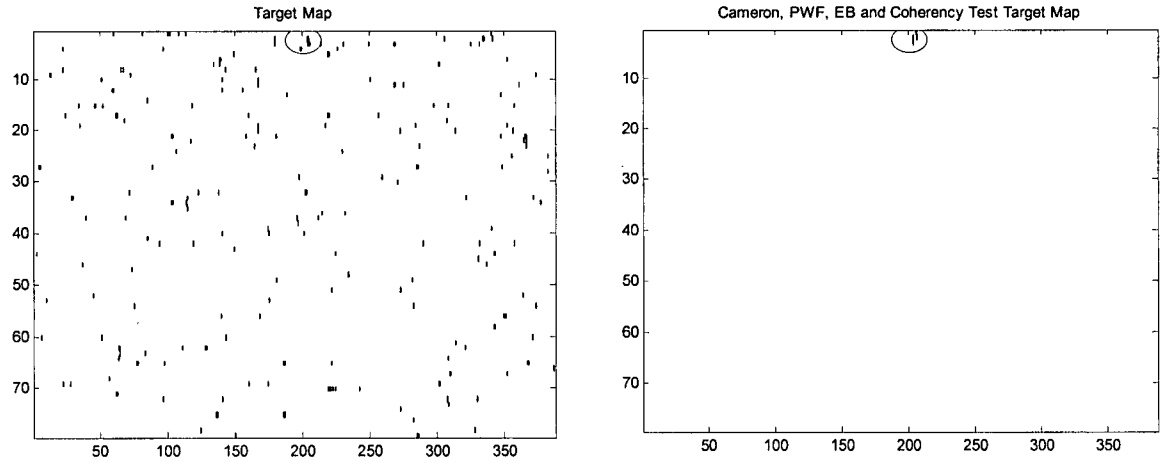

(a) (b)

Figure 25: Target 7 - Plots from Methodologies 3 and 4. (a) Freeman-Durden target map showing pixels that present a percentage of dihedral scattering above the chosen threshold. (b) Combined results of Cameron (dihedrals plus narrow dihedrals), PWF, Even Bounce and Coherence Test.

6.2.2 Results for Target 14 (House in Forest)

6.2.2.1 Target Description

Target 14 is a house located in a remote area and is surrounded by forest.

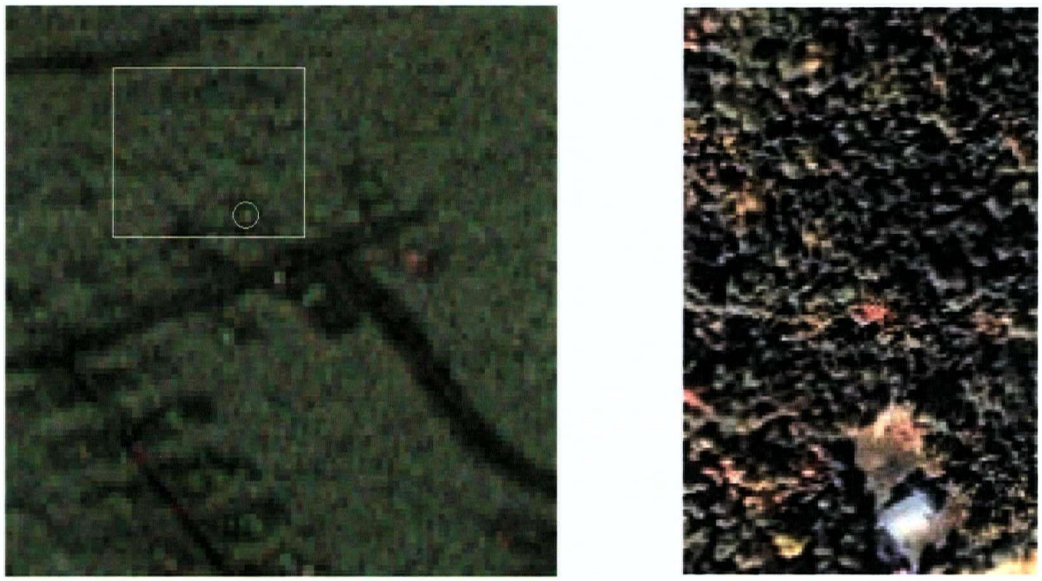

Figure 26: Target 14 - RGB composite and photograph. Left: Colour composite image (HH – Red, HV – Green, VV – Blue) showing Target 2 (in the ellipse) and the surrounding ground. The white diagonal feature in the image is a ditch separating two crop fields. Right: Target 2.

Analysis:

Methodologies 1 and 2 presented very few false alarms (one each – see Figure 27). Only two out of the three detected target pixels were the same in these two detection maps. Methodology 4 did not detect the target with these thresholds, as the minimum size allowed is three pixels. Therefore, Methodology 4 was applied after re-applying Methodologies 1 and 2 with lower thresholds.

The false alarm rate in Methodology 4 is lower than in Methodologies 1 and 2. The false alarm detected was the only one present in all results from this methodology. This

detection happened in area of high forest, and no man made feature could be seen in the Ikonos image.

The percentage of dihedrals calculated by Freeman-Durden for this image was comparatively low all over the scene, but the target was not detected. For illustration purposes the detection result of Methodology 3 with a 1% threshold is shown in the processing results.

	Methodology 1	Methodology 2	Methodology 3	Methodology 4
False Alarm count	2	2	56	1
False Alarm Rate	144	144	4,042	72

Table 6: Target 14 - False Alarm count and False Alarm Rate (false alarms/km^2).

6.2.2.2 Processing Results for Target 14

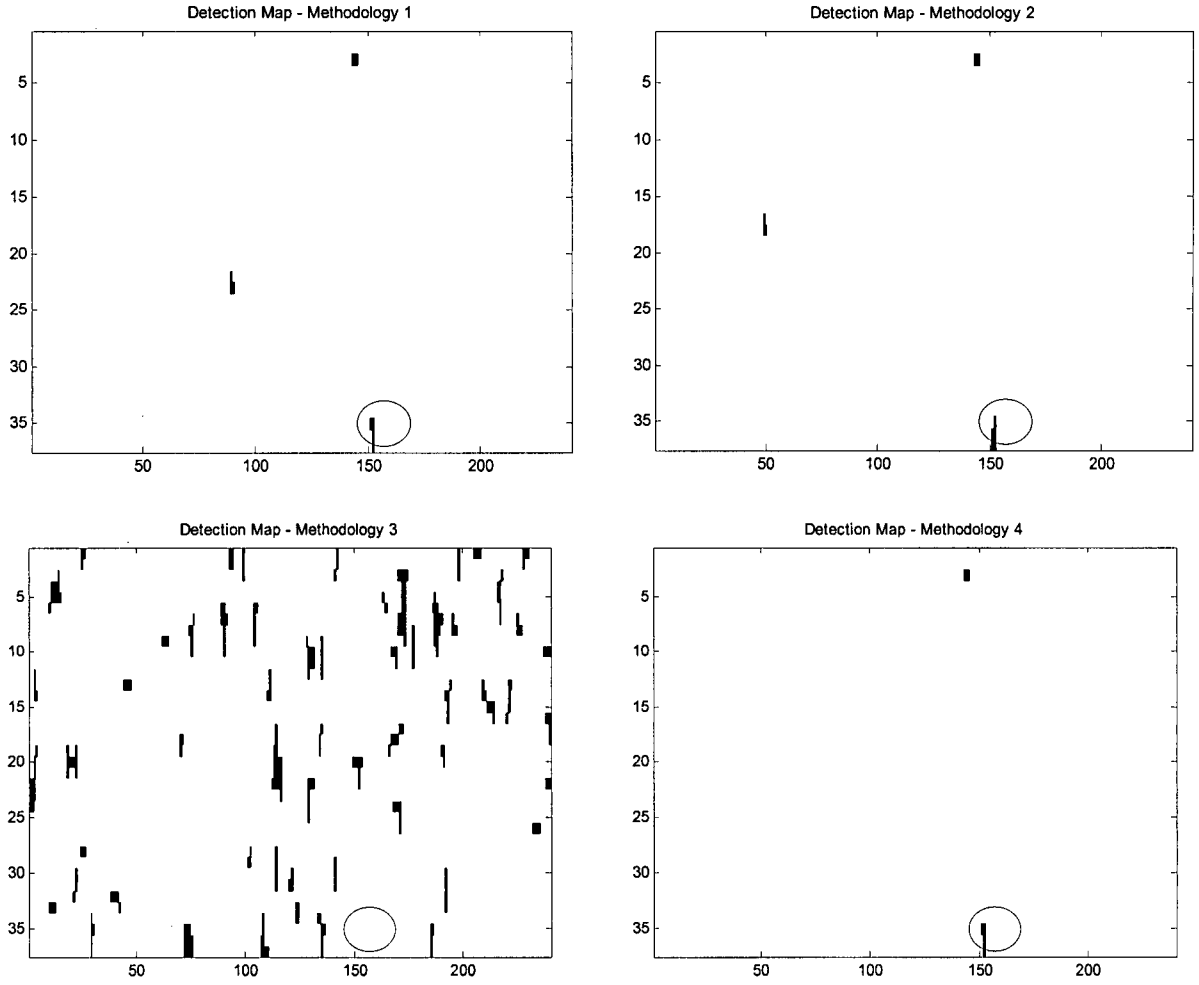

Figure 27: Target 14 - Final detection maps for Methodologies 1 to 4.

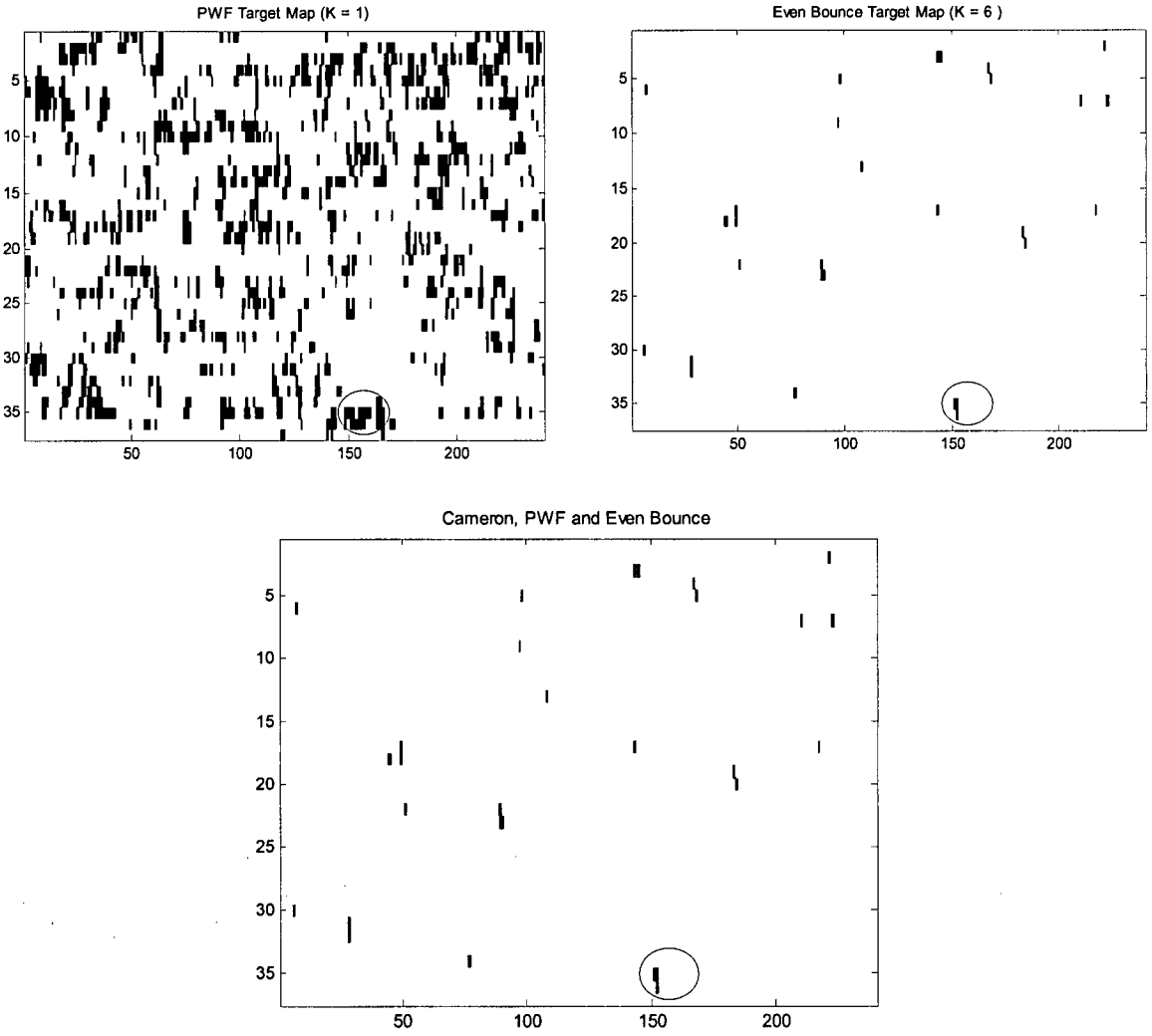

Figure 28: Target 14 - Plots from Methodology 1. Upper left: PWF target map. Upper right: Even Bounce target map. Bottom: combined result of Cameron (dihedrals plus narrow dihedrals), PWF and Even Bounce. K is the CFAR constant.

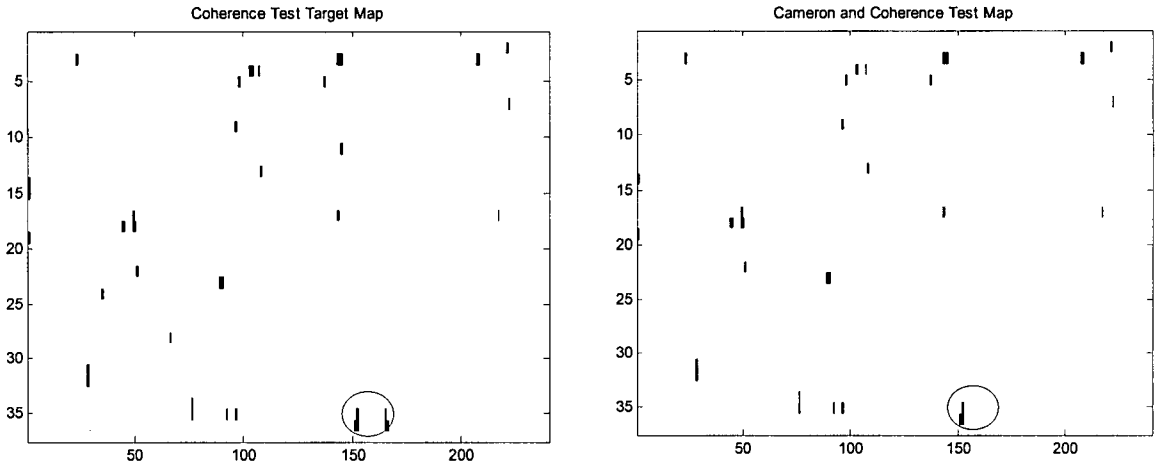

(a) (b)

Figure 29: Target 14 - Plots from Methodology 2. (a) Coherence Test target map. (b) Combined result of Cameron (dihedrals plus narrow dihedrals) and Coherence Test.

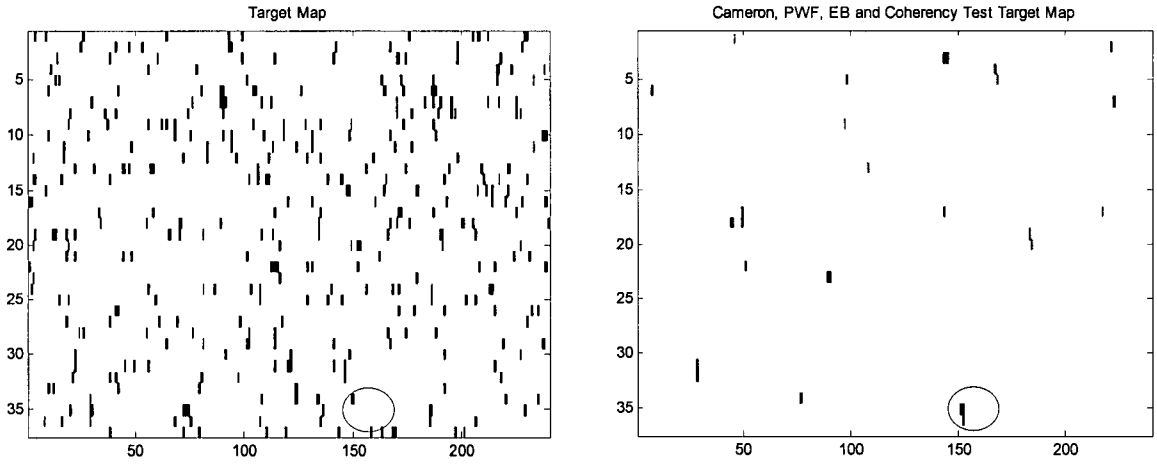

(a) (b)

Figure 30: Target 14 - Plots from Methodologies 3 and 4. (a) Freeman-Durden target map showing pixels that present a percentage of dihedral scattering above the chosen threshold. (b) Combined results of Cameron (dihedrals plus narrow dihedrals), PWF, Even Bounce and Coherence Test.

6.2.3 Results for Target 21 (House in Forest)

6.2.3.1 Target Description

Target 21 is a house by a forest near Gagetown. Both the house and the forest surrounding it are bounded by a road, which is not included in the image.

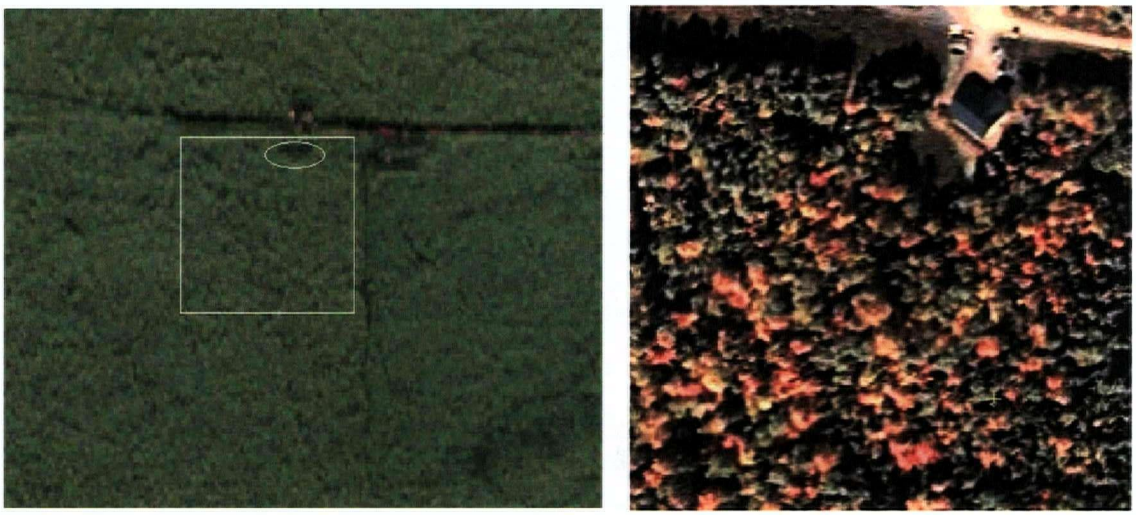

Figure 31: Target 21 - RGB composite and photograph. **Left:** Colour composite image (HH – Red, HV – Green, VV – Blue) showing Target 7 (in the ellipse) and the surrounding ground. **Right:** Target 7.

Analysis:

Both Methodologies 1 and 2 showed 2 false alarms each in the forest area (see Figure 32). In Methodology 4 it was possible to detect the target while removing these false alarms without having to change the thresholds.

The forest's high backscatter might be what degraded the PWF performance (see Figure 33). Coherence Test and Even Bounce Analysis had considerably less false detections than the PWF.

Methodology 3 generated a high number of false alarms, as the threshold had to be set in a low value (13%) in order to detect the house. If compared to the results of Target 7, the house in Target 21 was much less detectable by this methodology than the house in Target 7. This is probably due to the house's orientation with respect to the radar look direction: the house in Target 7 has walls perpendicular to the radar line of sight, while in Target 21 the house walls make a 45 degrees angle with the line of sight.

	Methodology 1	Methodology 2	Methodology 3	Methodology 4
False Alarm count	2	2	74	0
False Alarm Rate	44	44	1,652	0

Table 7: Target 21 - False Alarm count and False Alarm Rate (false alarms/km^2)

6.2.3.2 Processing Results for Target 21

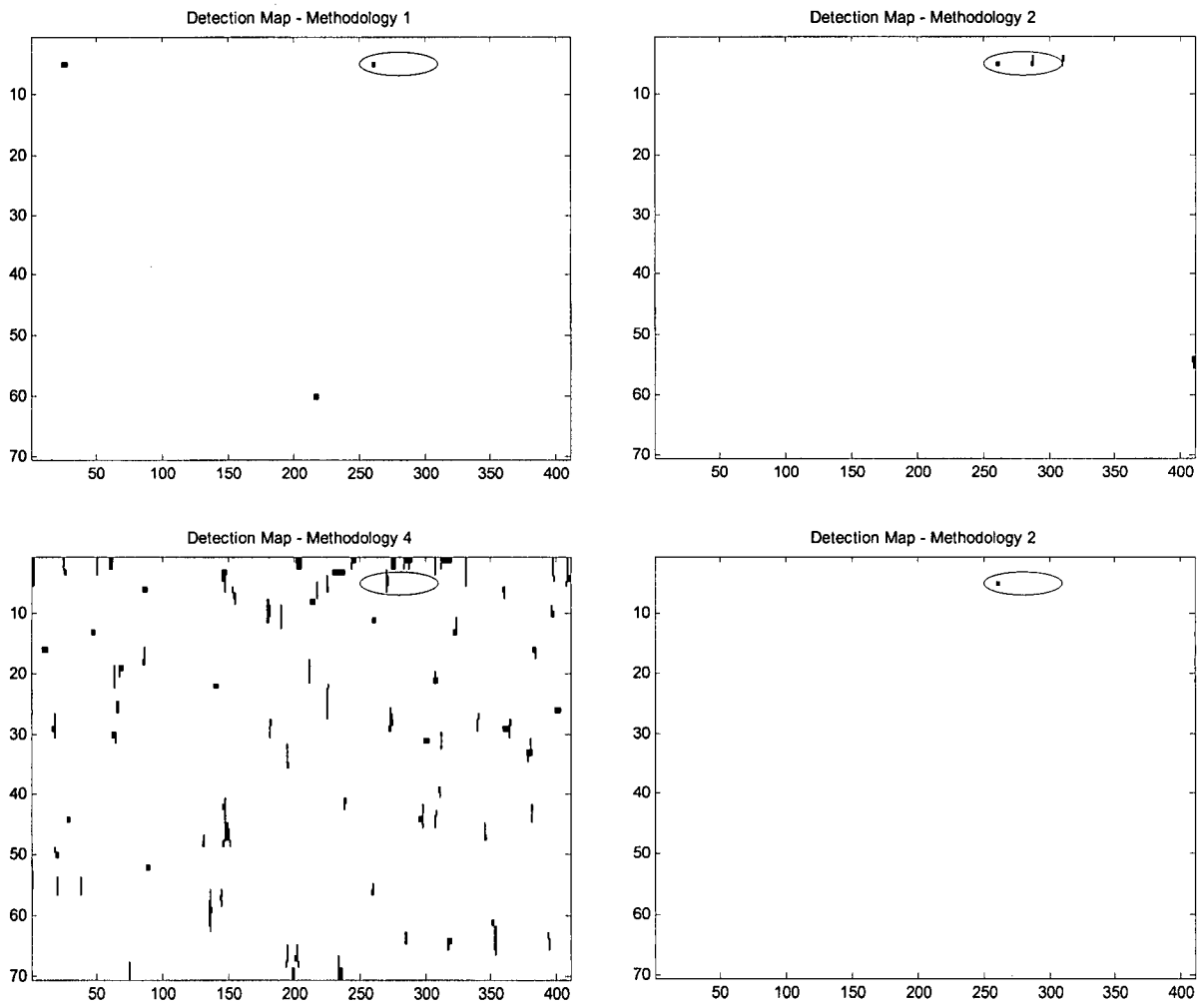

Figure 32: Target 21 - Final detection maps for Methodologies 1 to 4.

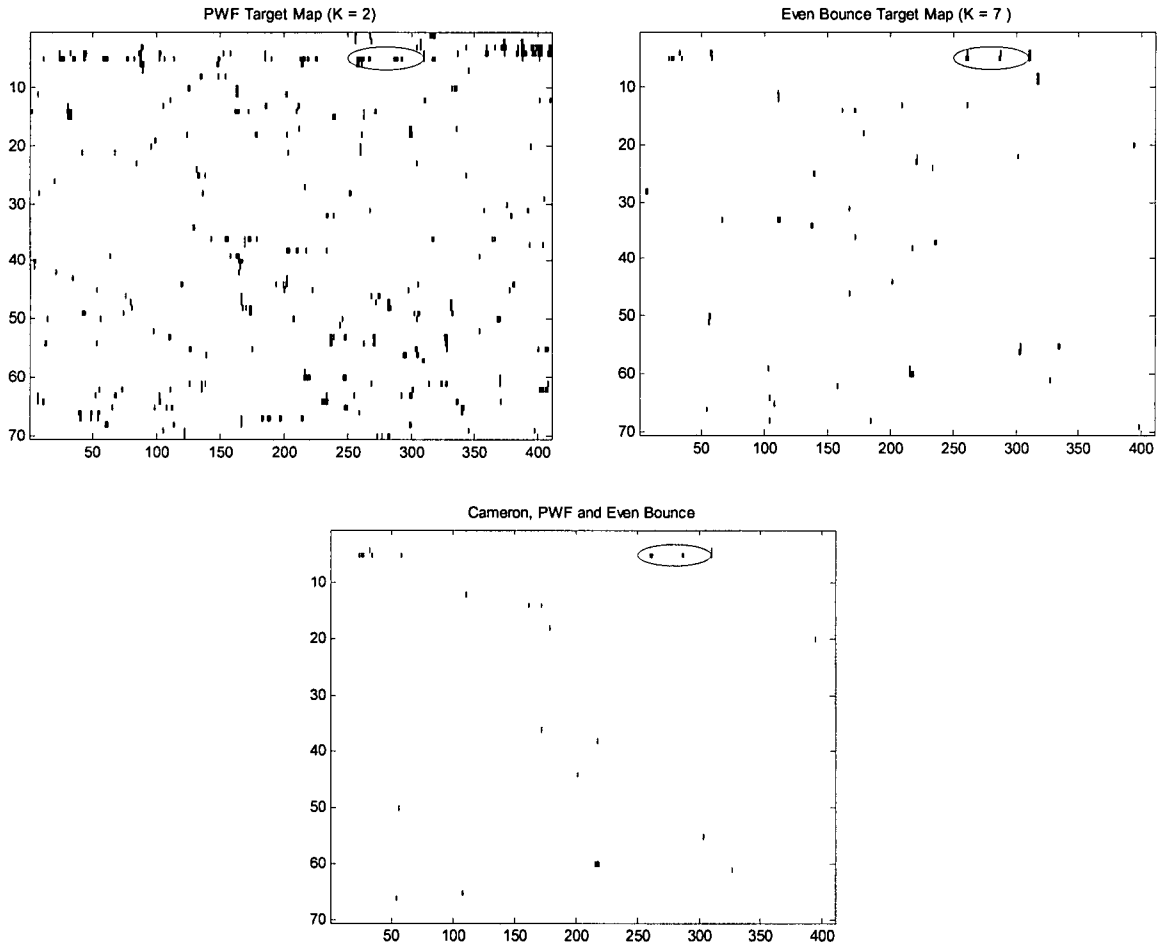

Figure 33: Target 21 - Plots from Methodology **1.** Upper left: PWF target map. Upper right: Even Bounce target map. Bottom: combined result of Cameron (dihedrals plus narrow dihedrals), PWF and Even Bounce. K is the CFAR constant.

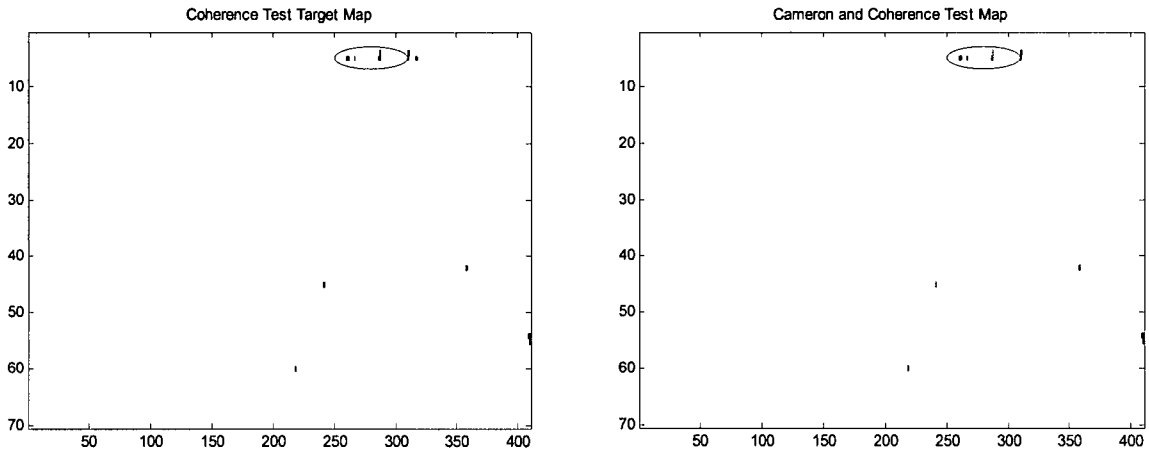

(a) (b)

Figure 34: Target 21 - Plots from Methodology 2. (a) Coherence Test target map. (b) Combined result of Cameron (dihedrals plus narrow dihedrals) and Coherence Test.

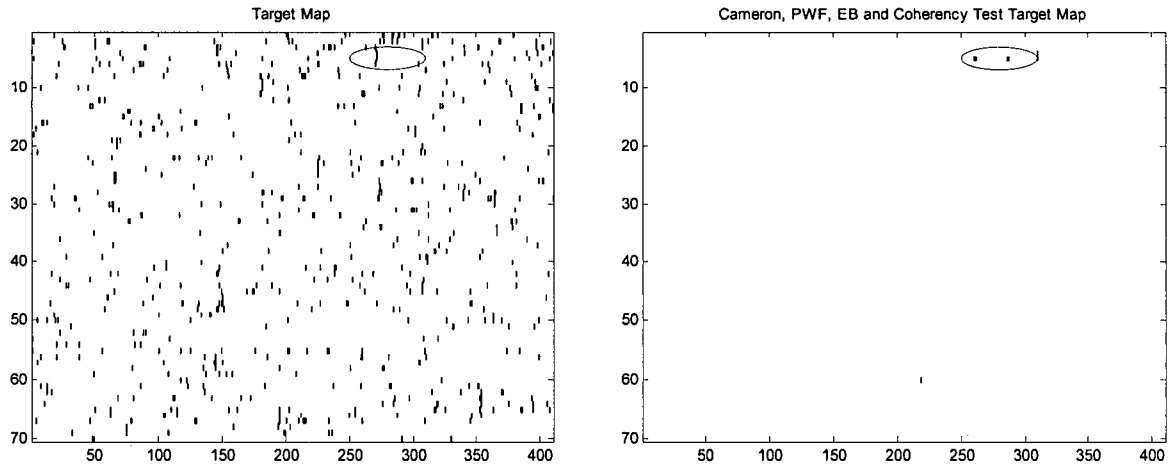

(a) (b)

Figure 35: Target 21 - Plots from Methodologies 3 and 4. (a) Freeman-Durden target map showing pixels that present a percentage of dihedral scattering above the chosen threshold. (b) Combined results of Cameron (dihedrals plus narrow dihedrals), PWF, Even Bounce and Coherence Test.

6.2.4 Results for Target 1 (Two Vertical Cylinders)

6.2.4.1 Target Description

Two vertical steel cylinders about 3 meters high and with a 4 meters diameter located on the boundary between a forested area and a wheat field in Westham Island.

Figure 36: Target 1 - RGB composite and photograph. **Left:** Colour composite image (HH – Red, HV – Green, VV – Blue) showing Target 1 (in the ellipse) and the approximate boundaries of the processed sub-image (in the rectangle). **Right:** Photograph of Target 1.

Analysis:

All the algorithms present a few more detections in the forested area (left of the target), than in the wheat field (Figures 48, 49 and 50 in Section A.1).

Methodologies 1, 2 and 4 detect the target with no false alarms, and the detection algorithms show few detections other than the target. This may be due to the fact that the target is large and has a strong response, allowing for high threshold values and therefore low false alarm rate. This is not only for its size but also because vertical cylinders behave like a vertical pole or tree trunk, presenting a strong dihedral response. Methodology 3 has a higher false alarm rate than other methodologies.

6.2.4.2 Processing Results for Target 1

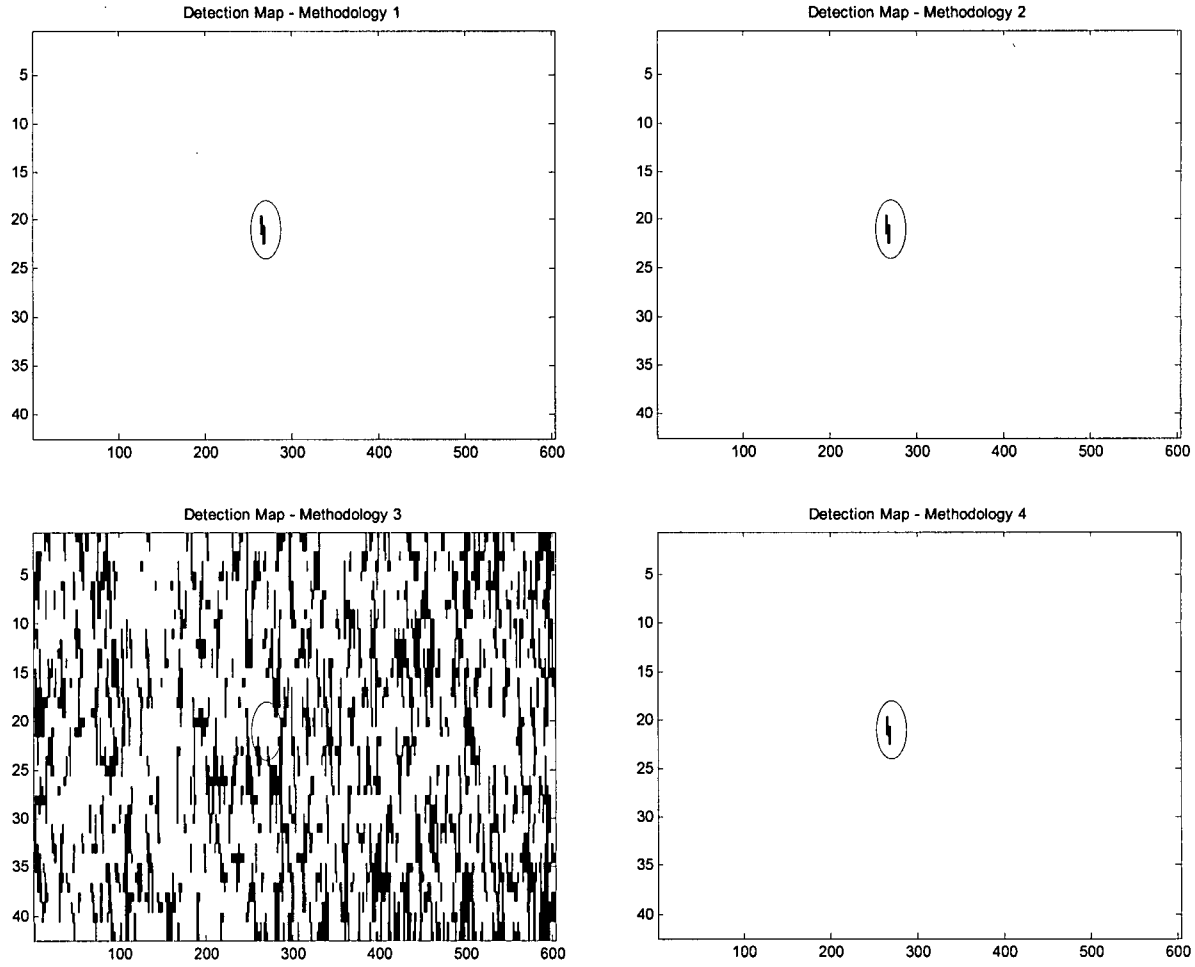

Figure 37: Target 1 - Final detection maps for Methodologies 1 to 4.

	Methodology 1	Methodology 2	Methodology 3	Methodology 4
False Alarm count	0	0	203	0
False Alarm Rate	0	0	5,138	0

Table 8: Target 1 - False Alarm count and False Alarm Rate (false alarms/km^2)

6.2.5 Results for Target 2 (Plow in Grass)

6.2.5.1 Target Description

Target 2 is an agricultural plowing machine. It is located close to a ditch that separates two crop fields. The ground in the lower left field is mostly bare soil with sparse, low grass. The upper right field is covered in higher grass.

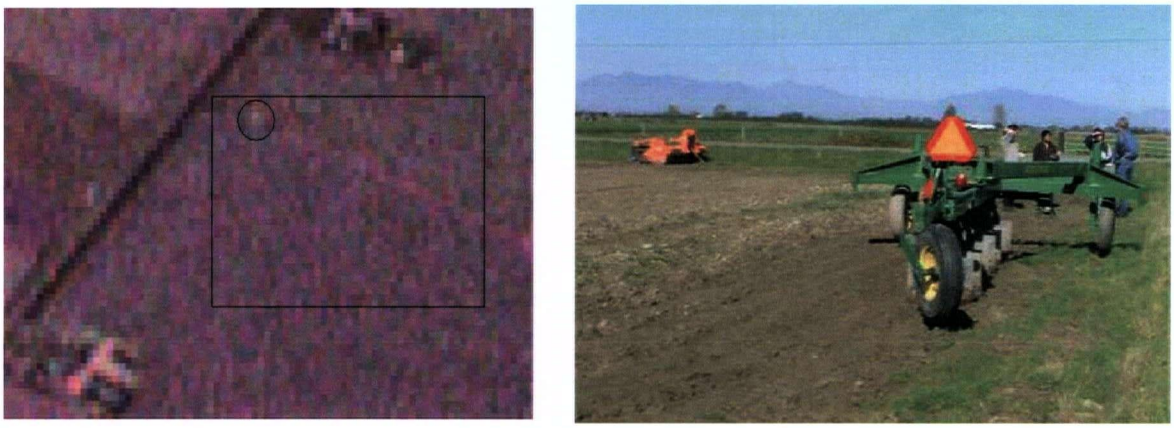

Figure 38: Target 2 - RGB composite and photograph. Left: Colour composite image (HH – Red, HV – Green, VV – Blue) showing Target 2 (in the ellipse) and the surrounding ground. Right: Target 2.

Analysis:

All the algorithms present more detections on the upper right field, where the grass causes higher, more diffuse backscatter than the bare soil. The Coherence Test detects a feature that is larger than the target in the lower field, but this feature is erased when the Coherence Test target map is combined with Cameron Decomposition. Even Bounce analysis shows less false alarms than both PWF and Coherence Test.

All algorithms have detections in the ditch, where the slope facing the radar can present occasional single and double bounce behaviour. But these detections, as the others left after the combined results of Methodologies 1 and 2 are generated, are random pixels erased by morphological processing.

Methodology 3 has a very high false alarm rate. Methodology 4 cannot be assessed as both Methodologies 1 and 2 presented zero false alarms.

6.2.5.2 Processing Results for Target 2

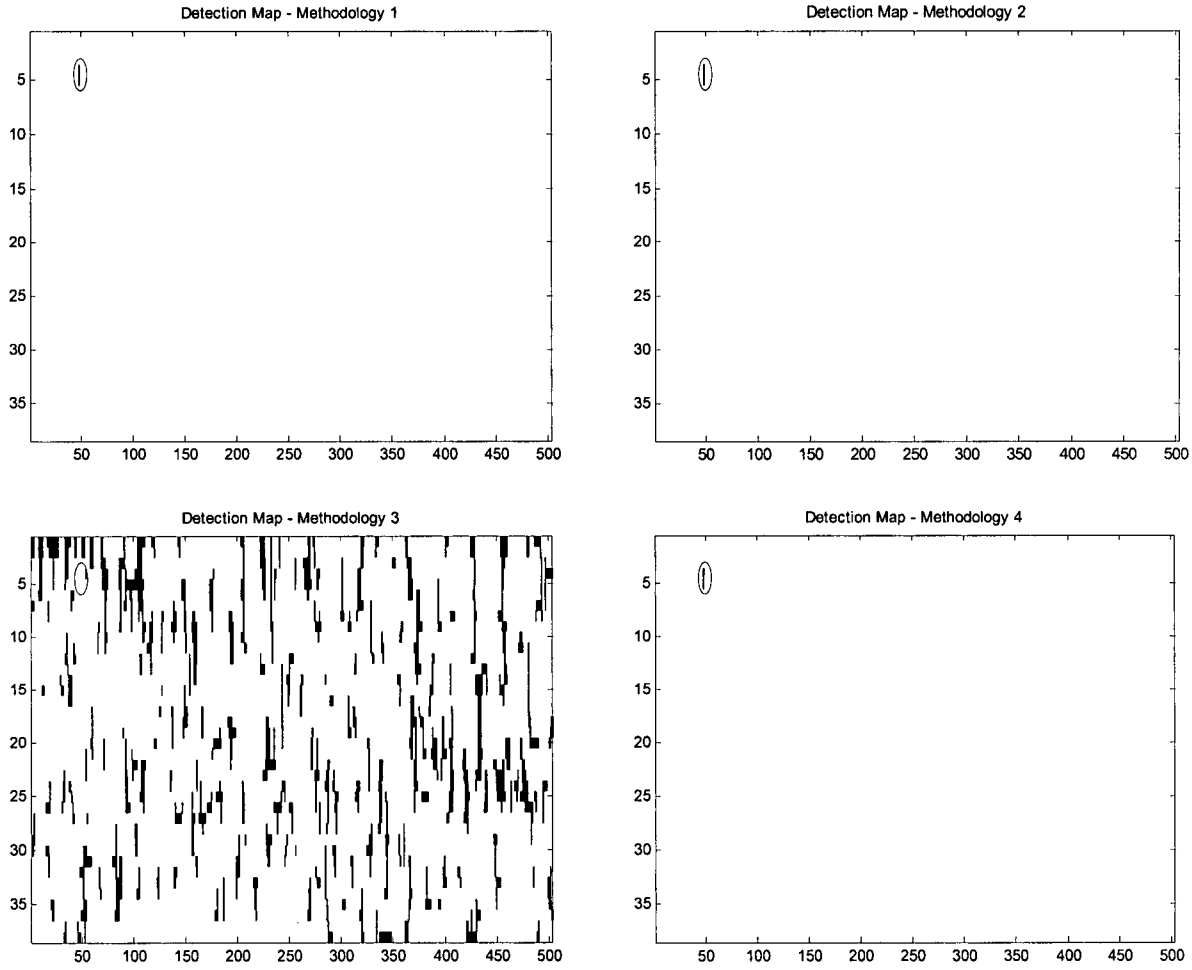

Figure 39: Target 2 - Final detection maps for Methodologies 1 to 4.

	Methodology 1	Methodology 2	Methodology 3	Methodology 4
False Alarm count	0	0	152	0
False Alarm Rate	0	0	5,875	0

Table 9: Target 2 - False Alarm count and False Alarm Rate (false alarms/km^2)

6.2.6 Results for Target 4 (Large Farm Cart)

6.2.6.1 Target Description

Target 4 is a large farm cart (blue cart in the photo) in Westham Island. Due to target location in the scene other man made targets had to be included, making this a complex scene. A single tree is located to the right hand side of the target. There are two clutter fields in the scene: low grass on the lower left part and medium grass on the upper right.

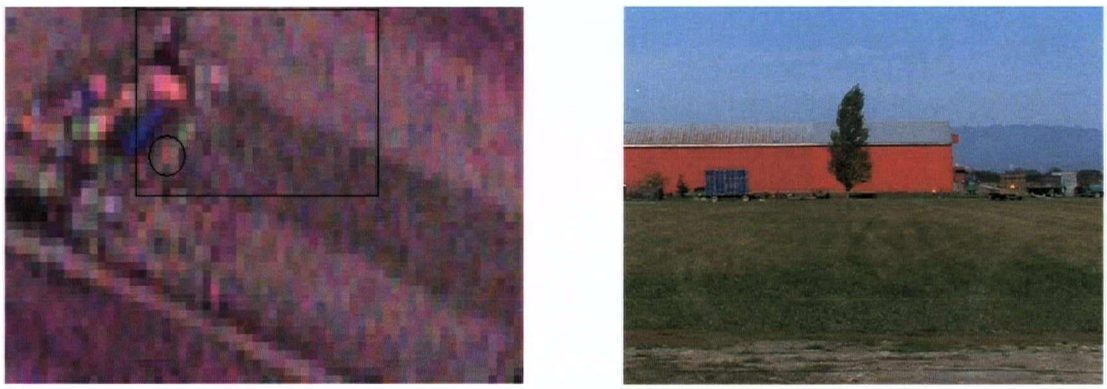

Figure 40: Target 4 - RGB composite and photograph**.** Left: Colour composite image (HH – Red, HV – Green, VV – Blue) showing Target 4 (in the ellipse) and the surrounding ground. Other man made features are present in this image. Right: Target 4 (blue cart), a single tree and other features: barn and machinery.

Analysis:

The taller grass field presented a considerable higher number of detections than the low grass field in all algorithms (Figures 54, 55 and 56), showing that the higher the vegetation the more likely it is to produce double bounce behaviour. Most of these detections were erased for not being classified as dihedrals by Cameron, and the remaining ones were of small size and were erased by the morphological processing. No false alarms were present in Methodologies 1, 2 and 4. Other man made features were detected by all algorithms, but were not considered in the false alarm rate count.

It is noteworthy that the single tree had pixels detected by Even Bounce, Coherence Test and Cameron (see Section A.4). It did not appear in the final detection map of Methodology 1 because it was not detected by PWF and because only two pixels were detected. Methodology 3 generated a much higher FAR.

6.2.6.2 Processing Results for Target 4

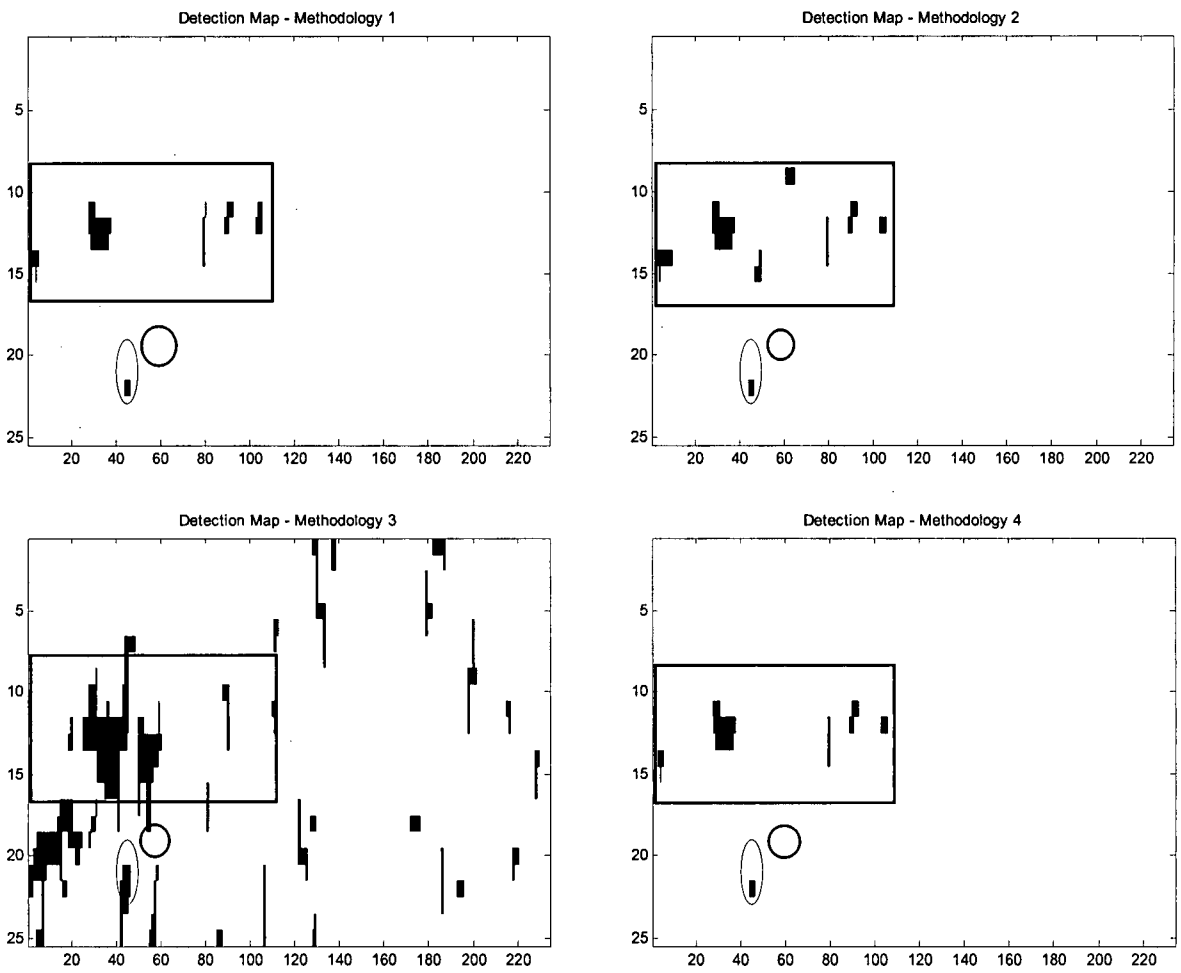

Figure 41: Target 4 - Final detection maps for Methodologies 1 to 4. Pixels in the rectangle are other man made targets in this complex scene. The circle indicates the location of a tree.

	Methodology 1	Methodology 2	Methodology 3	Methodology 4
False Alarm count	0	0	16	0
False Alarm Rate	0	0	1,749	0

Table 10: Target 4 - False Alarm count and False Alarm Rate (false alarms/km^2)

6.2.7 Results for Target 5 (Horizontal Cylinders)

6.2.7.1 Target Description

Target 5 is a set of two metal water tanks on stands with a horizontal cylindrical shape located in Westham Island. The tanks are 2-3 meters in diameter. The target is a few meters above the ground. There's some bare soil to the left of the target, but most of the clutter in the scene is composed of corn fields.

Figure 42: Target 5 - RGB composite and photograph. Left: Colour composite image (HH – Red, HV – Green, VV – Blue) showing Target 5 (in the ellipse) and the surrounding ground. The clutter is a corn field. Right: Photograph of Target 5.

Analysis:

Most of the pixels covering this target were detected by PWF and Even Bounce. Thresholds were lowered to cover more target pixels, but only one of the target pixels occupied was classified by Cameron Decomposition as a dihedral. The cylindrical shape of the target is the likely cause. In Methodology 2, the Coherence Test detected 4 pixels of the target, but also here combined result with Cameron Decomposition didn't allow target detection. The target was detected in Methodology 3 at a very high false alarm rate.

6.2.7.2 Processing Results for Target 5

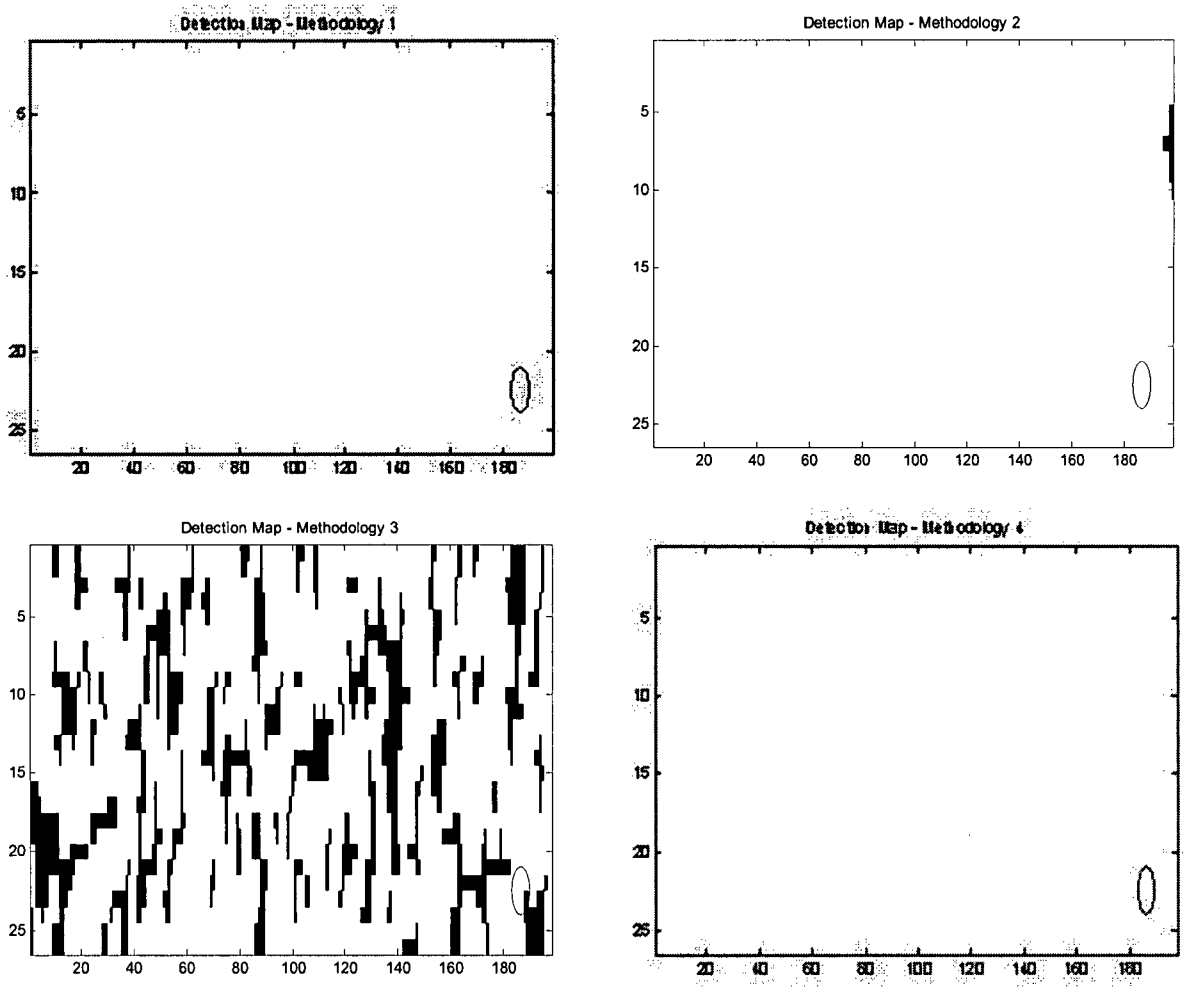

Figure 43: Target 5 - Final detection maps for Methodologies 1 to 4.

	Methodology 1	Methodology 2	Methodology 3	Methodology 4
False Alarm count	-	-	54	-
False Alarm Rate	-	-	6,724	-

Table 11: Target 5 - False Alarm count and False Alarm Rate (false alarms/km^2)

6.2.8 Results for Target 12 (Artillery Pieces in Gagetown)

6.2.8.1 Target Description

Target 12 is a set of four artillery pieces on permanent display at the Gagetown military base. There are a few trees close to one of the pieces, and the remaining clutter is short grass.

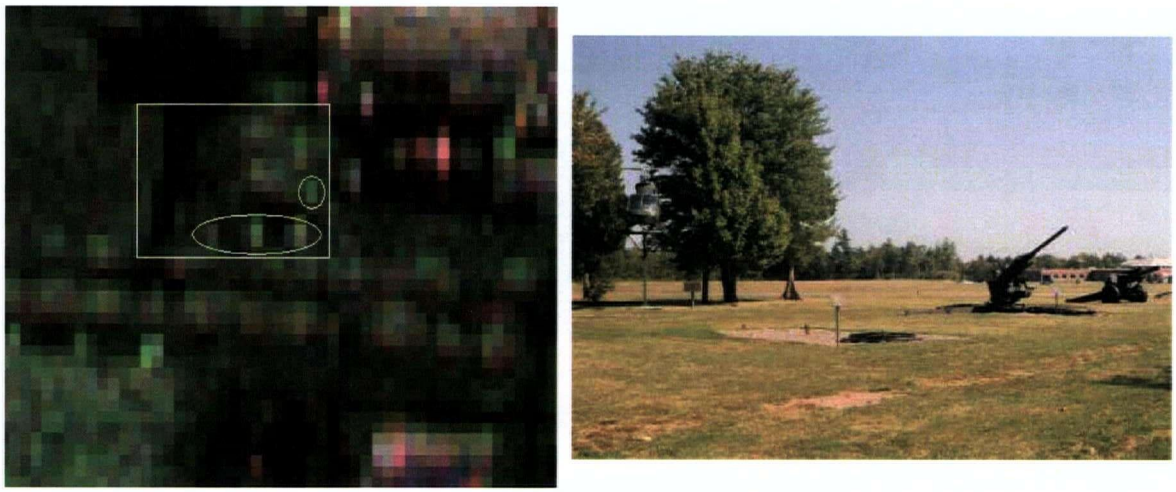

Figure 44: Target 12 - RGB composite and photograph. Left: Colour composite image (HH – Red, HV – Green, VV – Blue) highlighting the pieces that Target 12 (in the ellipse) and the surrounding ground. Right: Target 7.

Analysis:

Methodology 1 performs well, detecting the targets with no false alarms. One of the false alarms come from the trees, which was also detected by the PWF. Methodology 2 results in three false alarms, with the Coherence Test detecting the trees and part of the grass.

It was not possible to detect the targets with Methodology 3, because there were less than 3 connected target samples for each of the targets. The target map from Methodology 3 shows that one target was detected with a threshold value as low as 1% (Figure 62).

6.2.8.2 Processing Results for Target 12

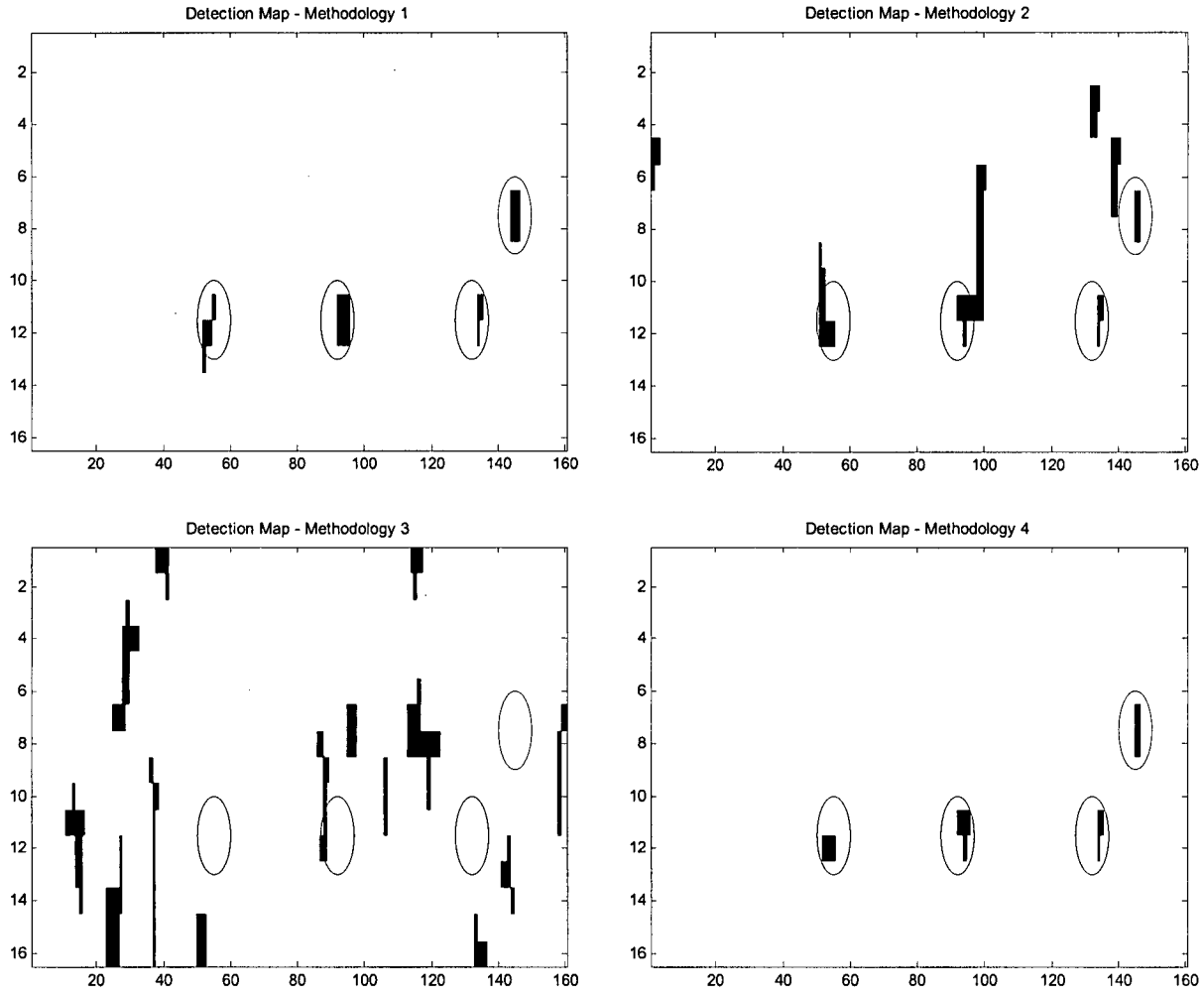

Figure 45: Target 12 - Final detection maps for Methodologies 1 to 4.

	Methodology 1	Methodology 2	Methodology 3	Methodology 4
False Alarm count	0	3	13	0
False Alarm Rate	0	751	3,225	0

Table 12: Target 12 - False Alarm count and False Alarm Rate (false alarms/km^2)

6.2.9 Results for Target 20 (Crashed Airplane)

6.2.9.1 Target Description

Target 20 is a crashed plane (same scene used by Lukowski *et al.* [8,9,10]).

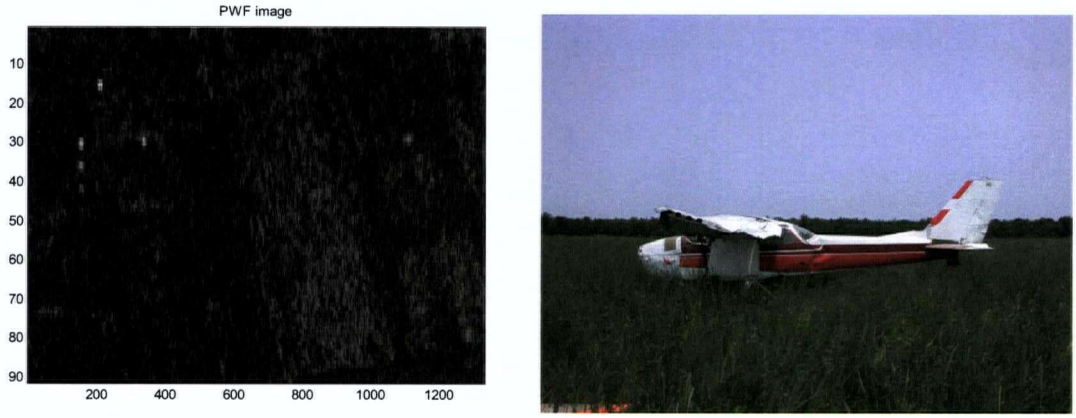

Figure 46: Target 20 - RGB composite and photograph. Left: PWF image showing Target 20, corner reflectors and the surrounding ground. Right: Target 20.

Analysis:

The Coherence Test was more sensitive to the brightness of the grass then the PWF and the Even Bounce. Cameron Decomposition eliminated the false detections on all three algorithms (see Figures 63, 64 and 65).

The corner detectors are detected well by the PWF due to their high target-to-clutter ratio, but have very few samples in Even Bounce Analysis and Coherence Test. As these devices are trihedrals, Cameron Decomposition did not detect them and they were not included in the detection maps. Methodologies 1, 2 and 4 generated no false alarms, while Methodology 3 presented a very high false alarm rate. This may be due to the fact that the target-to-clutter ratio does not affect Freeman-Durden classification.

6.2.9.2 Processing Results for Target 20

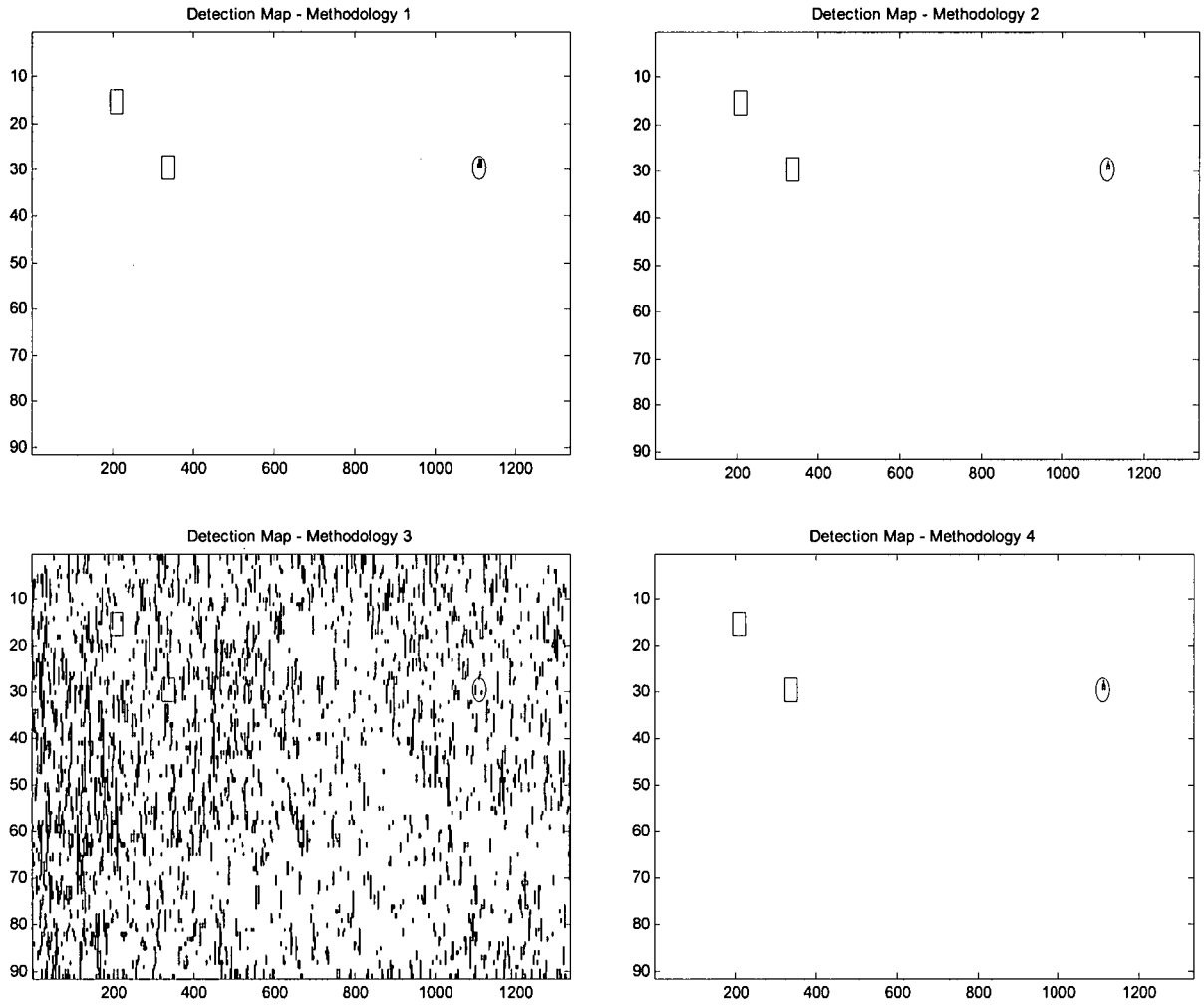

Figure 47: Target 20 - Final detection maps for Methodologies 1 to 4. Rectangles show locations of corner reflectors.

	Methodology 1	Methodology 2	Methodology 3	Methodology 4
False Alarm count	0	0	1,122	0
False Alarm Rate	0	0	5,.933	0

Table 13: Target 20 - False Alarm count and False Alarm Rate (false alarms/km^2)

6.3 Algorithm Threshold Values

Tables 14 and 15 present the threshold values used in the algorithms. The thresholds are: K, degree of coherence, Rician threshold and percentage of dihedral scattering contribution in Freeman–Durden Decomposition.

	CFAR PWF (K)	CFAR Even Bounce (K)	Degree of Coherence	Rician threshold (dB)	Percentage of Dihedral scattering contribution (Freeman -Durden)
Target 1	3	8	0.6	10	40%
Target 2	2	6	0.55	4	50%
Target 4	2	2	0.5	8	76%
Target 5	1	4	0.5	8	38%
Target 7	2	4	0.5	7	94%
Target 12	2	6	0.38	11	69%
Target 14	1	6	0.65	8	1%
Target 21	2	7	0.6	11	13%
Target 20*	3	5	0.9	8	63%

*** Data used by Lukowski *et al.*[10]**

Table 14: Optimal thresholds when Methodologies 1, 2 and 3 are applied.

	CFAR PWF (K)	CFAR Even Bounce (K)	Degree of Coherence	Rician threshold (dB)
Target 1	3	8	0.6	10
Target 2	2	6	0.55	4
Target 4	2	2	0.5	8
Target 5	1	4	0.5	8
Target 7	2	4	0.5	7
Target 12	2	6	0.38	11
Target 14	1	6	0.6	8
Target 21	2	7	0.6	11
Target 20*	3	5	0.9	8

*** Data used by Lukowski *et al.* [10]**

Table 15: Optimal thresholds when Methodology 4 is applied.

6.4 General Analysis

The results obtained by the application of the methodologies were compared and led to the conclusions that follow.

Methodology 3 is not suitable for this application. Many threshold values were tested for each target and, in order to retain the target, a large number of false alarms had to be kept as well. The man made targets do not seem to be perceived by Freeman-Durden Decomposition as stronger double bounce scatterers than the surrounding clutter.

Also, the thresholds used in Methodology 3 are not consistent from scene to scene. The values range from 13 to 94 (the 1% threshold was not counted here, as the target was not detected). This was the minimum percentage necessary to have three connected samples of the target detected.

Given the poor results of Methodology 3, we proceeded to compare the other three methodologies. Table 16 shows the total number of false alarms and the total false alarm rates per methodology.

In order to keep the results from being affected by complex scenes, we tried, as much as possible, to select homogeneous fields close to which there was ground-truthing information. This led to a limitation on image size, and the average image size was 150 x 200 m. For this reason, if any false alarms were present the false alarm rates would result in a high number.

	Methodology 1	Methodology 2	Methodology 4
False Alarm count (Low Vegetation)	0	3	0
False Alarm count (Medium Vegetation)	1	7	0
False Alarm count (High Vegetation)	4	4	1
Total False Alarm count	5	14	1
Total False Alarm Rate	210	1087	72

Table 16: False alarm count for low, medium and high vegetation types, total false alarm count and total false alarm rate (false alarms/ km^2) for each methodology.

Some targets do not have enough samples classified by Cameron Decomposition as dihedrals and cannot be detected by Methodologies 1 and 2. In this work, this is the case of Target 5.

In order to apply Methodology 4 the original thresholds may have to be changed, so all the algorithms can detect the minimum number of pixels. A comparison of Tables 14 and 15 show that only in one case the thresholds were changed, and by a small amount. This shows that the pixels detected by both methodologies in the target are very similar.

The threshold values used in Methodologies 1, 2, and 4 did not present a large variability. Therefore, there is the possibility that a single threshold would give an acceptable detection performance.

In the coherence test (in Methodology 2) the Rician threshold seems to be more sensitive to pixel intensities. Decreasing the threshold values seems to include fewer bright samples. This is expected as the Rician threshold is related to the signal-to-clutter ratio.

Table 16 shows numerical results for Methodologies 1, 2 and 4. Total false alarm count, total false alarm rate and false alarm count per vegetation type are presented. Results from the scenes containing Targets 1, 2, 4, 12 and 20 were used to calculate the low vegetation totals. Results from the scenes containing Targets 14 and 21 were used to calculate the high vegetation totals. The clutter surrounding Target 7 was considered neither high nor low because of its vegetation size and roughness. Therefore, results from Target 7 scene were shown in a separate row, which was named medium vegetation.

Total false alarm results presented in Table 16 show that the overall performance of Methodology 1 was better than Methodology 2, but Methodology 4 presented the best results. It is important to notice that, given the small size of the scenes and the relatively small number of targets, these numbers should be analyzed with care. For example, applying Methodology 2 resulted in 7 false alarms in Target 7 alone, which had a high influence on the total result.

Analysis of Table 16 also shows that Methodology 1 was very effective when applied to scenes with low vegetation clutter, while Methodology 2 was less effective than Methodology 1. When the clutter was composed of both medium and high vegetation, Methodology 1 performed less effectively than it did with low vegetation clutter, although it still performed better than Methodology 2. This supports the assumption that the DCA methodology would be less effective in forested areas. In these cases, Methodology 4 performs better than both Methodologies 1 and 2, contributing to decrease the false alarm rates. This leads to the main conclusion of this thesis: combined results from the Coherence Test from the Symmetric Scattering Characterization Method (SSCM) and the DCA methodology can improve the DCA methodology when the clutter has high vegetation.

CHAPTER 7 - CONCLUSIONS

7.1 Summary

This work, experimental and heuristic, illustrates a practical approach to target detection and is intended to serve as a reference for people building operational SAR remote sensing systems. Its purpose was to:

1. Review an existing target detection methodology that was developed to detect crashed airplanes in a specific clutter;

2. Test this methodology with a more diverse set of targets and clutter types;

3. Examine other available target detection algorithms and compare their performance with the methodology above;

4. Develop improvements to these methodologies to give good detection performance for a wide range of target and clutter types.

The starting point of this work is the methodology we call Detection of Crashed Airplanes (DCA). This methodology was applied by Lukowski in experiments to detect crashed airplanes in a low vegetation clutter. The DCA methodology uses the following algorithms: Polarimetric Whitening Filter (PWF), Even Bounce Analysis and Cameron Decomposition.

In this thesis the DCA methodology was reproduced and re-applied to the same dataset (referred to as the Ottawa Dataset in Chapter 5) and then applied on two other datasets (the Westham Island dataset and the Gagetown dataset) containing different man made targets and different vegetation clutters.

Four methodologies were tested and compared: Methodology 1 is the DCA methodology. Methodology 2 comprises the Coherence Test proposed by Touzi and Charbonneau combined with Cameron Decomposition. Methodology 3 is the application of Freeman-Durden Decomposition with a threshold applied to the dihedrals percentage. Methodology 4 is the application of the Coherence Test in combination with Methodology 1.

All data sets used in this research were fully polarimetric, C-band data acquired by the CV-580 SAR system. Ground reference data consisting of photographs and coordinates of potential targets were acquired on field trips on September, 2004 in Westham Island, south of Vancouver (BC). Ground reference data for the Ottawa and Gagetown datasets were also available.

Results for the four methodologies applied to 9 sub-images of the polarimetric data sets have been described. For the images processed in this work, Methodology 1 produces more false alarms when applied to higher vegetation clutter than when applied to the Ottawa dataset. Methodology 2 presented a marginally higher number of false alarms. Methodology 3 presented an extremely high number of false alarms in all situations. Methodology 4 generated the best detection results overall (i.e., it presented the smallest number of false alarms while detecting the known targets).

In the processing of each image, many different threshold combinations were tested in each of the methodologies. The optimal threshold values are the ones that yield the lowest false alarm rate for each image while detecting the known targets. The optimal thresholds were reported for each image and overall range of thresholds was determined. For Methodologies 1, 2 and 4 there was little variation in the threshold values used across the various images, while Methodology 3 needed a wide range of thresholds in order to detect the target.

Further analysis showed that for low vegetation clutters, Methodologies 1 and 2 typically detect the target with no or few false alarms. For high vegetation clutters there are always

false alarms and in these situations the application of Methodology 4 results in the lower false alarm rates.

These results support the work carried out by Lukowski for clutters of low vegetation. The results also extend the DCA methodology to different kinds of clutter and targets, proposing a new approach that performs better for a variety of situations.

7.2 Research Contributions

We have developed a new methodology that improves the detectability of man made targets in high vegetation clutter conditions. In pursuing this goal, the following contributions can be listed:

1. The assessment of the effectiveness of the Detection of Crashed Airplanes (DCA) methodology when applied to different data sets, different kinds of clutters and different kinds of targets.

2. The assessment of the effectiveness of using the Freeman-Durden Decomposition in the classification of targets that are supposedly coherent.

3. The application of the Coherence Test from the SSCM algorithm as a detection algorithm replacing both the PWF algorithm and the Even Bounce Analysis algorithm in the DCA methodology and the assessment of its effectiveness when compared to the original DCA methodology.

4. The application of the Coherence Test algorithm in combination with the three algorithms used in the DCA methodology (PWF, Even Bounce Analysis and Cameron Decomposition) as a new approach to decrease false

alarm rates when the DCA methodology is applied for high vegetation clutter.

5. The provision of a source of information on the application of radar polarimetry for target detection for users of data available from current and future spaceborne polarimetric SAR missions such as TerraSAR, RADARSAT-2 and COSMOS-Skymet.

7.3 Future Work

Based on the experience obtained with this study, the following issues could be suggested for future work in this field:

1. Analyse more target and clutter types to solidify our approach to setting the detection threshold, establishing and validating threshold models related to specific vegetation types. Apply a single threshold value for all scenes (applying Methodologies 1, 2 and 4) and analyse its performance.

2. Assess the effect of look direction in the effectiveness of man made target detection methods by acquiring different data sets using flight lines with different orientations.

3. Longer wavelengths could potentially be helpful for the detection of man made targets under vegetation cover. Experiments with multi-frequency SAR acquisitions could assess the effectiveness of the target detection algorithms when targets are totally or partially covered by vegetation.

4. SAR experiments related to classification are typically carried out on flat terrain, as were the ones we studied. Terrain effects due to the geometry of

radar data collection such as foreshortening, layover and very low local incidence angles usually lead to poor classification performance if only intensity is used. Man made targets located on undulated terrain might still be detected by their distinctive polarimetric signature even when the target-to-clutter ratio is low. Experiments should be performed to examine terrain effects.

5. The value of thresholds and the performance of the algorithms depend on the resolution of the radar system and on the signal/noise ratio of the data. In general, satellite SAR data has a lower resolution and a lower signal/noise ratio than airborne data. Experiments should be done with satellite data (or satellite data simulated from airborne data) to examine the effectiveness of the methodologies under the lower resolution and signal/noise ratios.

BIBLIOGRAPHY

[1] Ulaby, F., and C. Elachi, "Radar Polarimetry for Geoscience Applications", 1990.

[2] Touzi, R., W.M. Boerner, J.S. Lee, and E. Lueneburg, "A review of polarimetry in the context of synthetic aperture radar: concepts and information extraction", Can. J. Remote Sensing, Vol. 30, No. 3, pp. 380-407, 2004.

[3] Boerner, W.M., H. Mott, C. Livingstone, B. Brisco, R. Brown, J.S. Paterson, E. Luneburg, J.J. van Zyl, D. Randall, and P. Budkewitsch, Polarimetry in Remote Sensing: Basic and Applied Concepts, Chapter 5 in The Manual of Remote Sensing, 3rd edition, Principles and Applications of Imaging Radar, editor-in-chief R.A. Ryerson, American Society for Photogrammetry and Remote Sensing, Bethesda, Md., 1998.

[4] Oliver, C. J., and S. Quegan, "Understanding Synthetic Aperture Radar Images", Artech House, 1998.

[5] El-Saba, A.M., "Potential Application of Visible Passive Imaging Polarimetry in the Discrimination of Real Targets and Decoys", Proc. SPIE Vol. 5816, 2005.

[6] Van der Sanden, J. J. "Anticipated applications potential of RADARSAT-2 data", Can. J. Remote Sensing, Vol. 30, No. 3, pp. 369-379, 2004.

[7] Staples, G., J. Hornsby, W. Branson, K. O'Neill, and P. Rolland, "Turning the scientifically possible into the operationally practical: RADARSAT-2 commercialization plan", Can. J. Remote Sensing, Vol. 30, No. 3, pp. 408-414, 2004.

[8] Lukowski, T. I. and F. J. Charbonneau, "Synthetic aperture radar and search and rescue", In Proceedings of the IEEE International Geoscience and Remote Sensing Symposium (IGARSS'00), Honolulu, Hawaii, pp. 2374 – 2376, 24–28 July 2000.

[9] Lukowski, T. I. and F. J. Charbonneau, "Synthetic aperture radar and search and rescue: detection of crashed aircraft using imagery and interferometric methods", Canadian Journal of Remote Sensing, Vol. 28, No. 6, pp. 770-781, 2002.

[10] Lukowski, T. I., B. Yue, F. J. Charbonneau, F. Khellah, and R. K. Hawkins, "Detection of crashed aircraft in polarimetric imagery" Can. J. Remote Sensing, Vol. 30, No. 3, pp. 484-495, 2004.

[11] Novak, L.M., and Burl, M.C., "Optimal speckle reduction in polarimetric SAR imagery", IEEE Transactions on Aerospace and Electronic Systems, Vol. 26, pp. 293–305, 1990.

[12] Novak, L.M., Burl, M.C., and Irving, W.W., "Optimal polarimetric processing for enhanced target detection", IEEE Transactions on Aerospace and Electronic Systems, Vol. 29, No. 1, pp. 234–243, 1993.

[13] Evans, D.L., T.G. Farr, J.J. Van Zyl, and H.A. Zebker, "Radar polarimetry: analysis tools and applications", IEEE Transactions on Geoscience and Remote Sensing, Vol. 26, No. 6, pp. 774–789, 1995.

[14] Cumming, I. "Advanced Polarimetric Tutorial", Noetix Research, 2003.

[15] Dozono, H., R.K. Hawkins, K. Murnaghan, "Reading Convair-580 Polarimetric SAR Data", CCRS-TN-2004-006, 2005.

[16] Touzi, R. and F. Charbonneau, "Characterization of target symmetric scattering using polarimetric SARs". IEEE Transactions on Geoscience and Remote Sensing, Vol. 40, pp.2507-2516, 2002.

[17] Egan, W. G., "Photometry and polarization in remote sensing", Elsevier, 1985.

[18] Freeman, A. and S. Durden, "A three-component scattering model to describe polarimetric SAR data", IEEE Trans. Geoscience and Remote Sensing, vol. 36, no. 3, pp. 963 – 973, May 1998.

[19] Yeremy, M., J. Campbell, K. Mattar and T. Potter, "Ocean surveillance with polarimetric SAR", Can. J. Remote Sensing, vol. 17, no. 4, pp. 328–344, Aug. 2001.

[20] Yeremy, M., G. Geling and M. Rey, "Results of the crusade ship detection trial: Polarimetric SAR," in *Proc. IGARSS*, Jun. 24–28, vol. 2, pp. 711 – 713, 2002.

[21] Chotoo, K., B. Huxtable, A. Mansfield and H. Rais, "Probability of detection of downed aircraft using SAR polarimetry", In *Proc. SPIE*, vol. 4050, pp. 163–168, Apr. 2000.

[22] Cameron, W. L., N. N. Youssef and L. K. Leung, "Simulated polarimetric signatures of primitive geometrical shapes," IEEE Trans. Geoscience and Remote Sensing, vol. 34, no. 3, pp. 793 – 803, May 1996.

[23] Kreithen, D. E., S. Halversen and G. Owirka, "Discriminating Target From Clutter" in *The Lincoln Laboratory Journal*, vol. 6, number 1, 1993.

[24] Kennaugh, K., "Polarization properties of radar reflections", M.Sc. thesis, The Ohio State University, Columbus, Ohio, 1952.

[25] Huynen, J. R., "Measurement of the target scattering matrix", Proceedings of the IEEE, Vol. 53, No. 8, pp. 936–946, 1965.

[26] Van Zyl, J.J. "Unsupervised classification of scattering behavior using radar polarimetry data", *IEEE Trans. on Geoscience and Remote Sensing*, Vol. 27, No. 1, pp. 37 – 45, 1989.

[27] Cloude, S.R., and Pottier, E., "A review of target decomposition theorems in radar polarimetry", IEEE Trans. on Geoscience and Remote Sensing, Vol. 34, No. 2, pp. 498 – 518, 1996.

[28] Larson,V., L. Novak and C. Stewart, "Joint spatial polarimetric whitening filter to improve SAR target detection performance for spatially distributed targets" In Proc. *SPIE,* Vol. 2230, pp. 285-301, 1994.

[29] Henry, C., J. C. Souyris and P. Marthon, "Target Detection and Analysis Based on Spectral Analysis of a SAR Image: a Simulation Approach", Proceedings of IGARSS '03, Toulouse, France, pp. 2005—2007, 2003.

[30] G. De Grandi, J. S. Lee, D. Schuler, and E. Nezry, "Texture and speckle statistics in polarimetric SAR synthesized images," IEEE Trans. Geosci. Remote Sens., vol. 41, no. 9, pp. 2070-2088, Sep. 2003.

APPENDIX A - SUPPORTING PROCESSING RESULTS

The processing of the four methods generated a large amount of plots. In order to make the presentation more clear, we decided to keep in chapter 6 all the results of targets 7, 14 and 21 and the final detection map of each method for the remaining targets. The intermediate results for each of these remaining targets (Targets 1, 2, 4, 5, 12 and 20) were transferred to this appendix.

The plots are presented in the following manner: Each target is in one section of this appendix and contains four figures. Each of these figures contains the intermediate plots for one methodology. Captions indicate the methodology number and the contents of each plot.

All numerical results of this thesis are presented in Chapter 6.

A.1 – Target 1

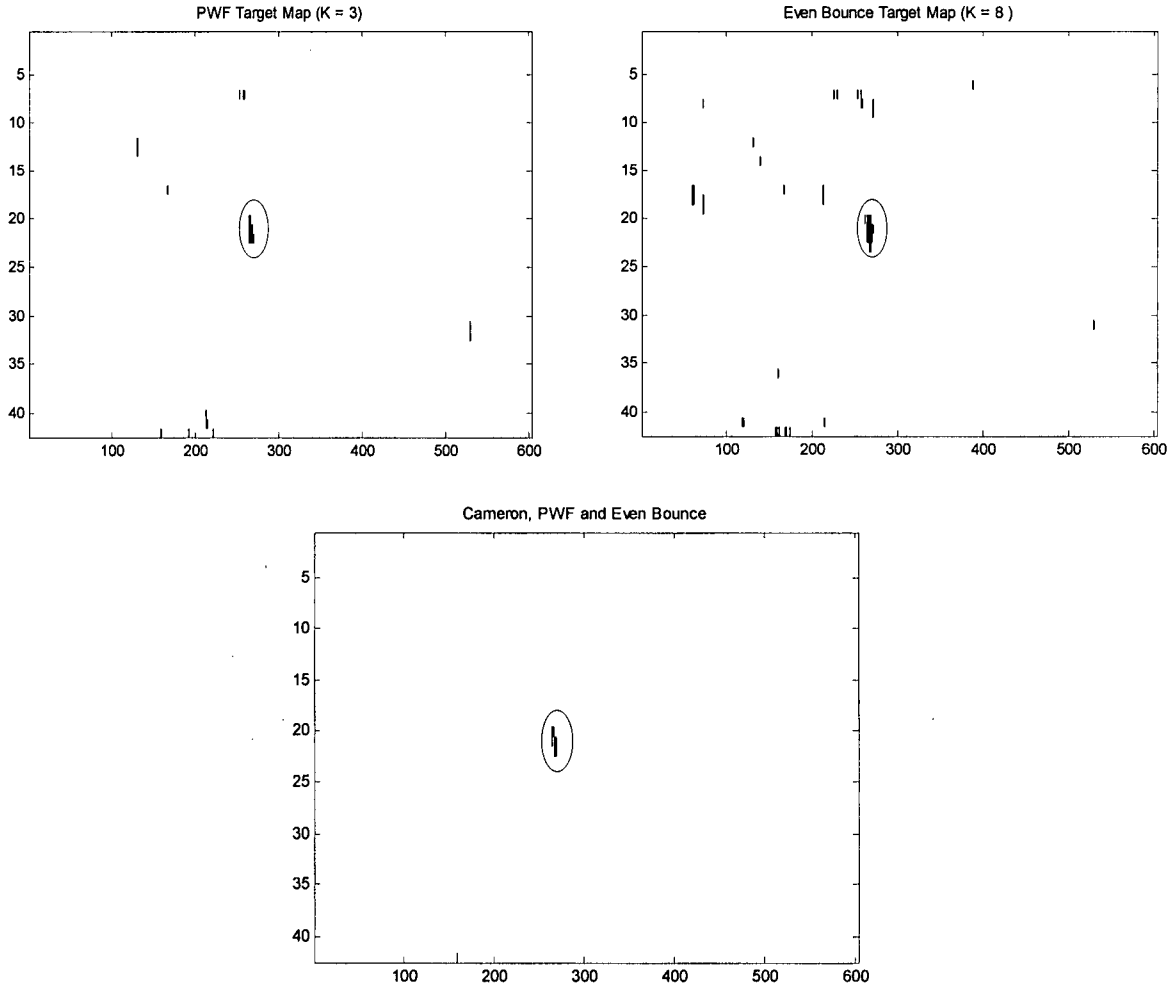

Figure 48: Target 1 - Plots from Methodology 1. Upper left: PWF target map. Upper right: Even Bounce target map. Bottom: combined result of Cameron (dihedrals plus narrow dihedrals), PWF and Even Bounce. K is the CFAR constant.

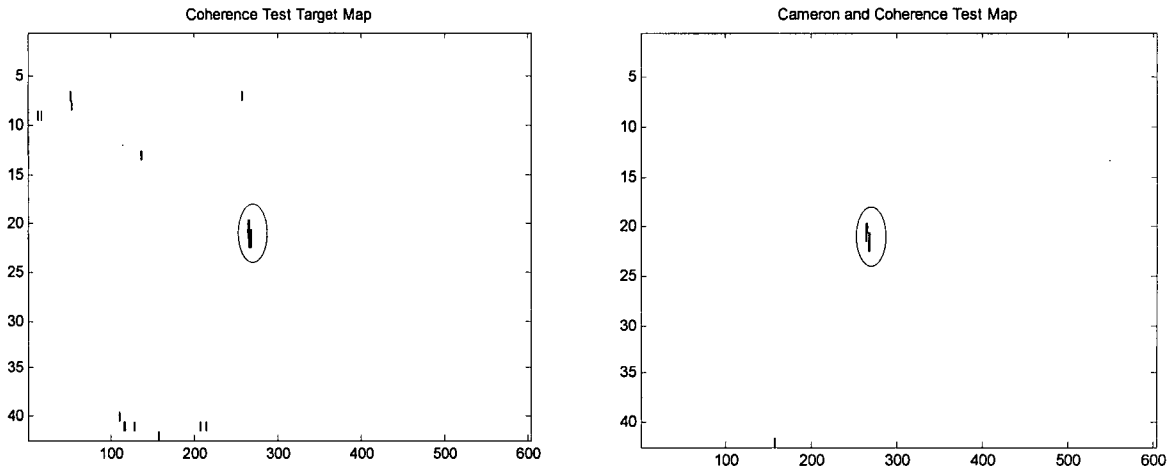

(a) (b)

Figure 49: Target 1 - Plots from Methodology 2. (a) Coherence Test target map. (b) Combined result of Cameron (dihedrals plus narrow dihedrals) and Coherence Test.

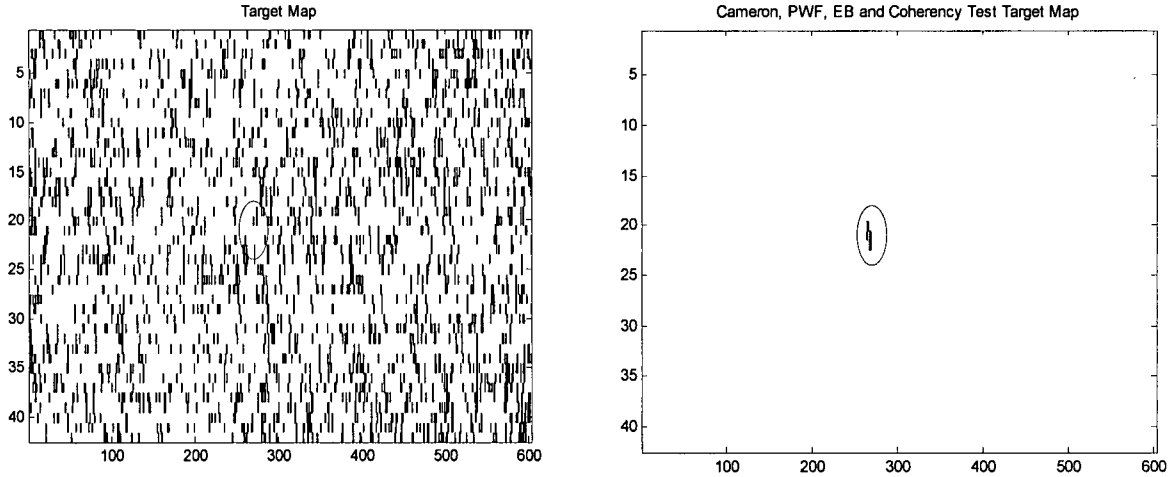

(a) (b)

Figure 50: Target 1 - Plots from Methodologies 3 and 4. (a) Freeman-Durden target map showing pixels that present a percentage of dihedral scattering above the chosen threshold. (b) Combined results of Cameron (dihedrals plus narrow dihedrals), PWF, Even Bounce and Coherence Test.

A.2 – Target 2

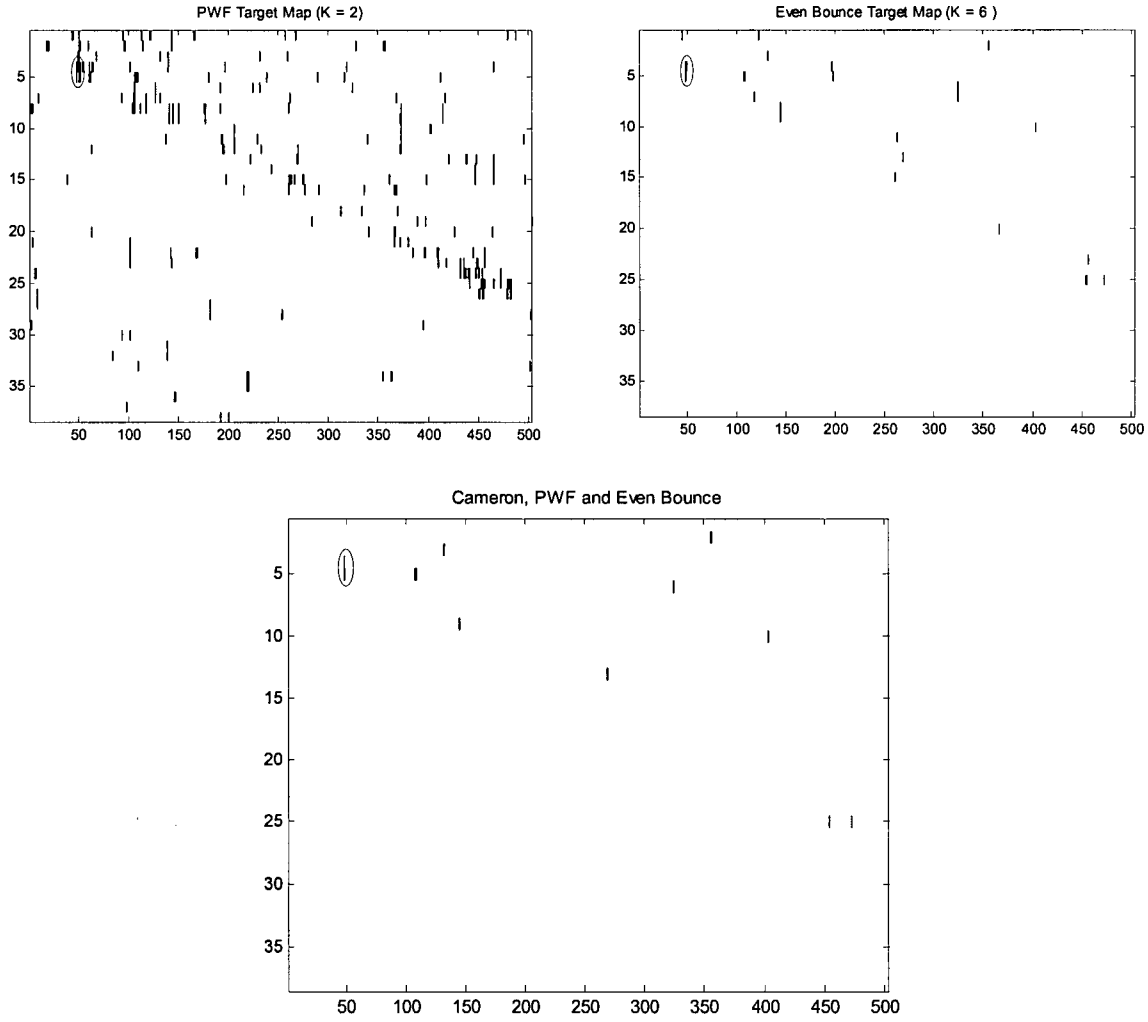

Figure 51: Target 2 - Plots from Methodology 1. Upper left: PWF target map. Upper right: Even Bounce target map. Bottom: combined result of Cameron (dihedrals plus narrow dihedrals), PWF and Even Bounce. K is the CFAR constant.

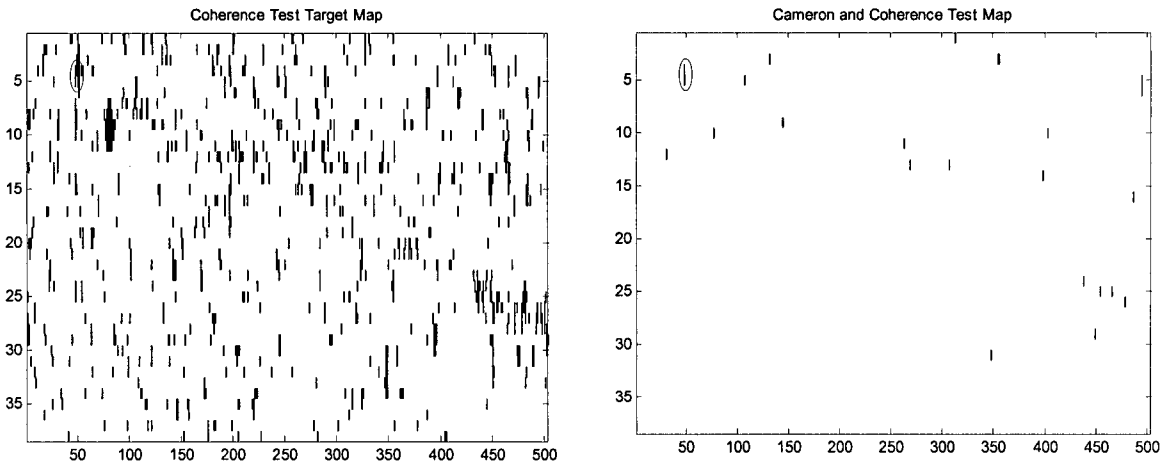

(a) (b)

Figure 52: Target 2 - Plots from Methodology 2. (a) Coherence Test target map. (b) Combined result of Cameron (dihedrals plus narrow dihedrals) and Coherence Test.

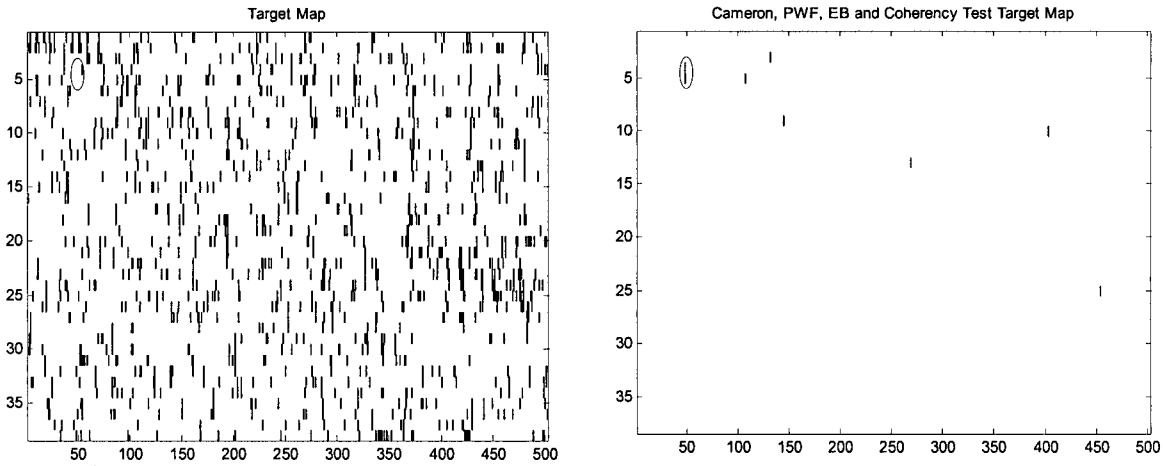

(a) (b)

Figure 53: Target 2 - Plots from Methodologies 3 and 4. (a) Freeman-Durden target map showing pixels that present a percentage of dihedral scattering above the chosen threshold. (b) Combined results of Cameron (dihedrals plus narrow dihedrals), PWF, Even Bounce and Coherence Test.

A.3 – Target 4

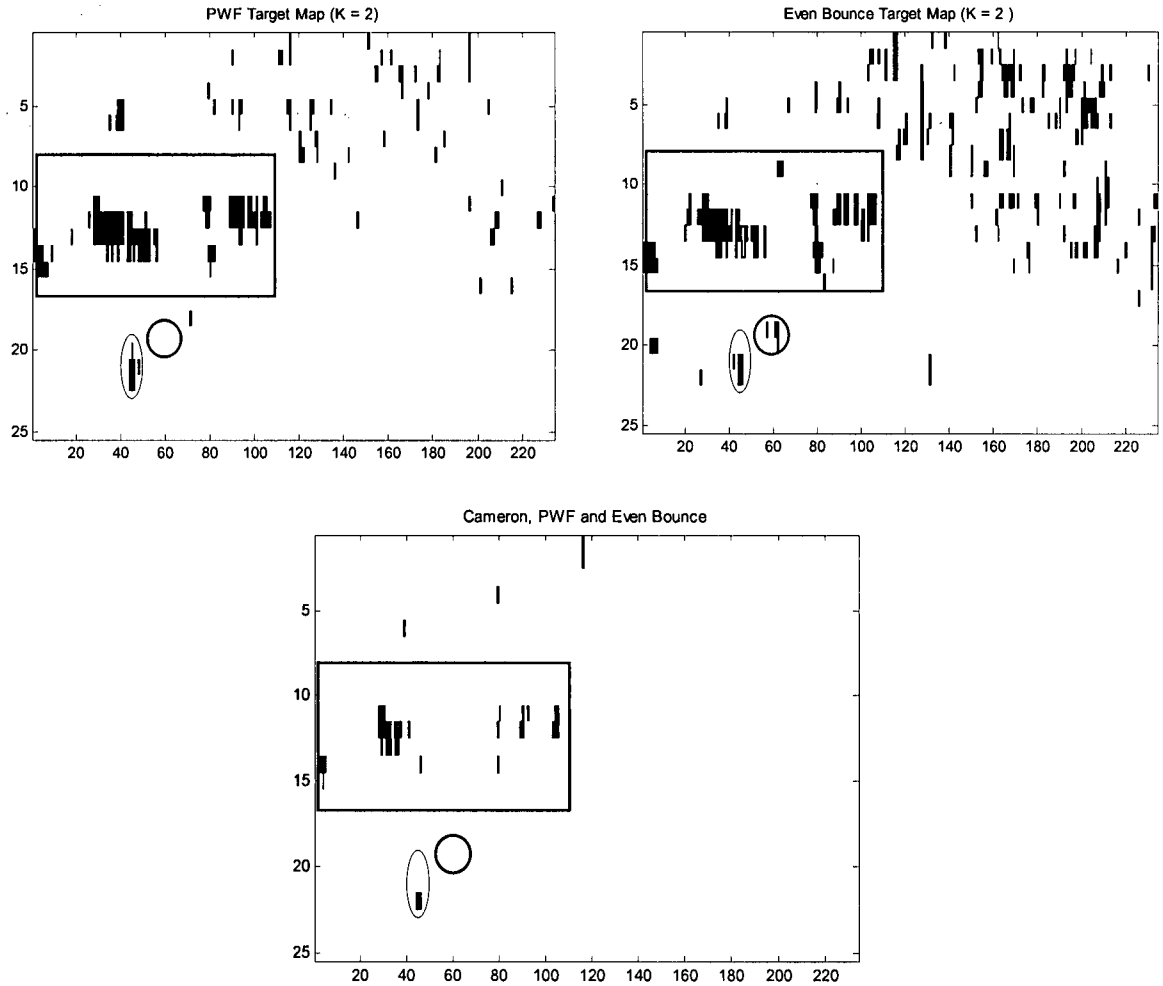

Figure 54: Target 4 - Plots from Methodology 1. Upper left: PWF target map. Upper right: Even Bounce target map. Bottom: combined result of Cameron (dihedrals plus narrow dihedrals), PWF and Even Bounce. K is the CFAR constant. Pixels in the rectangle are other man made targets in this complex scene. Circle indicates location of a tree.

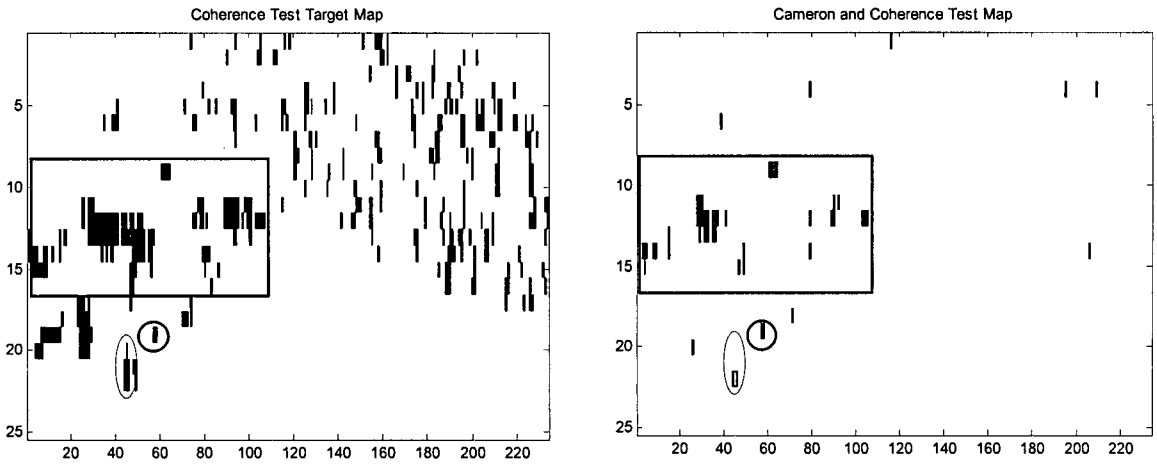

(a) (b)

Figure 55: Target 4 - Plots from Methodology 2. (a) Coherence Test target map. (b) Combined result of Cameron (dihedrals plus narrow dihedrals) and Coherence Test. Pixels in the rectangle are other man made targets in this complex scene. Circle indicates location of a tree.

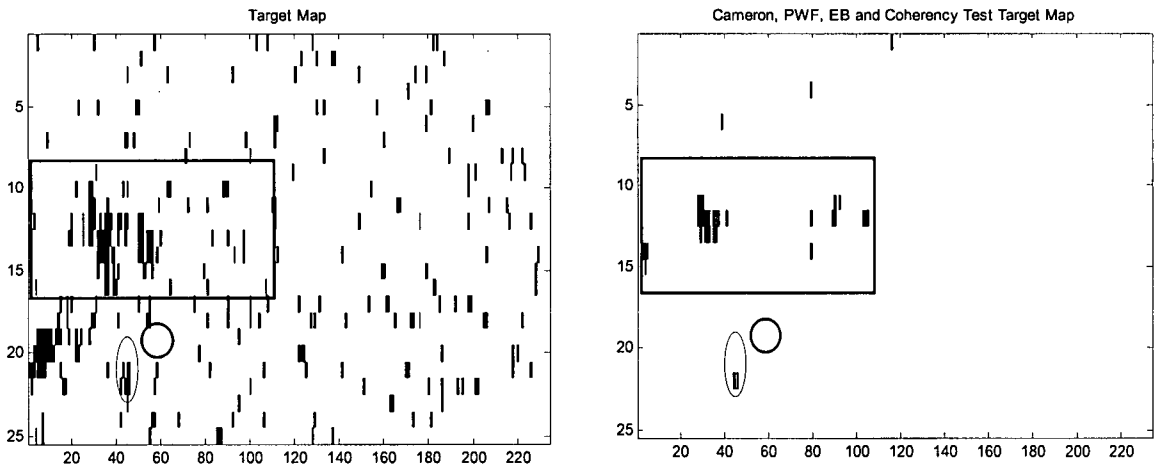

(a) (b)

Figure 56: Target 4 - Plots from Methodologies 3 and 4. (a) Freeman-Durden target map showing pixels that present a percentage of dihedral scattering above the chosen threshold. (b) Combined results of Cameron (dihedrals plus narrow dihedrals), PWF, Even Bounce and Coherence Test. Pixels in the rectangle are other man made targets in this complex scene. Circle indicates location of a tree.

A.4 – Target 5

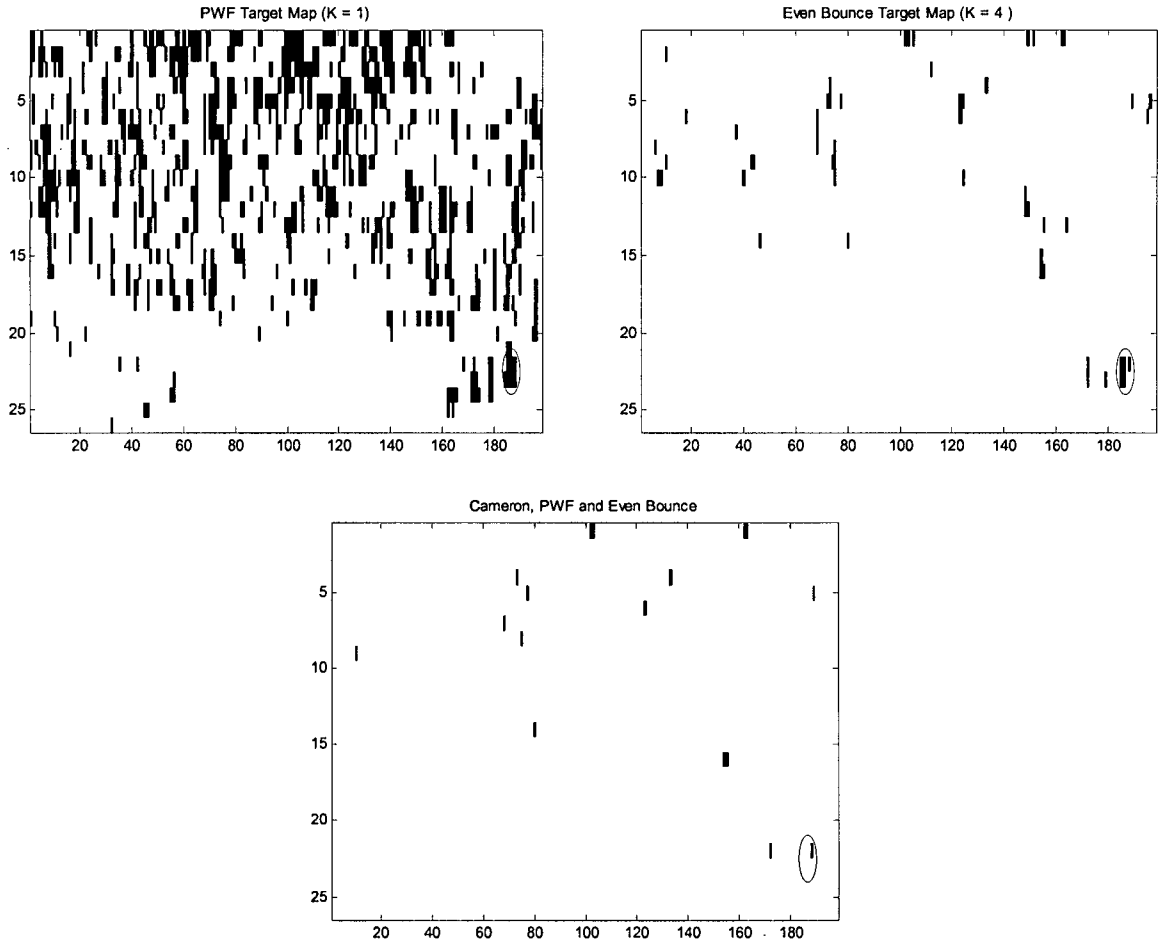

Figure 57: Target 5 - Plots from Methodology 1. Upper left: PWF target map. Upper right: Even Bounce target map. Bottom: combined result of Cameron (dihedrals plus narrow dihedrals), PWF and Even Bounce. K is the CFAR constant.

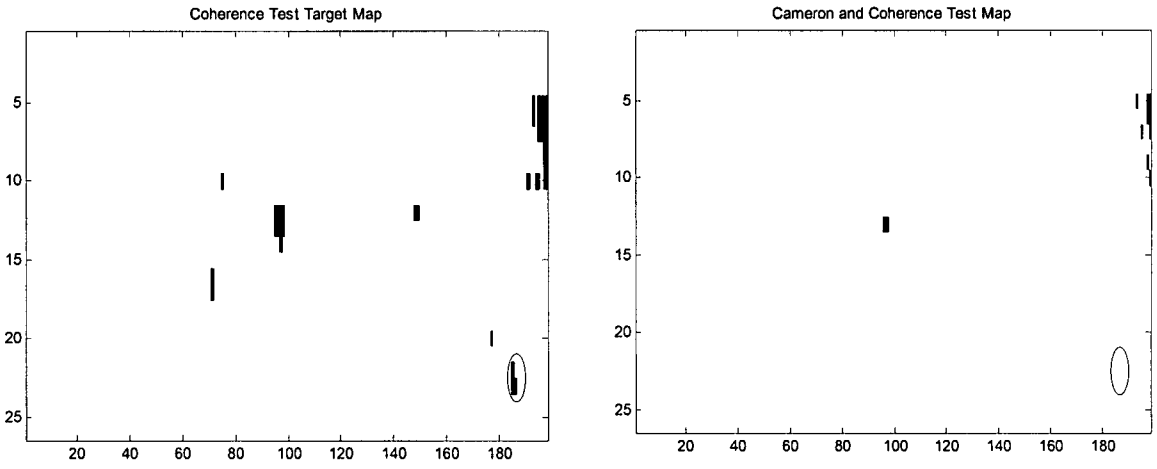

(a) (b)

Figure 58: Target 5 - Plots from Methodology 2. (a) Coherence Test target map. (b) Combined result of Cameron (dihedrals plus narrow dihedrals) and Coherence Test.

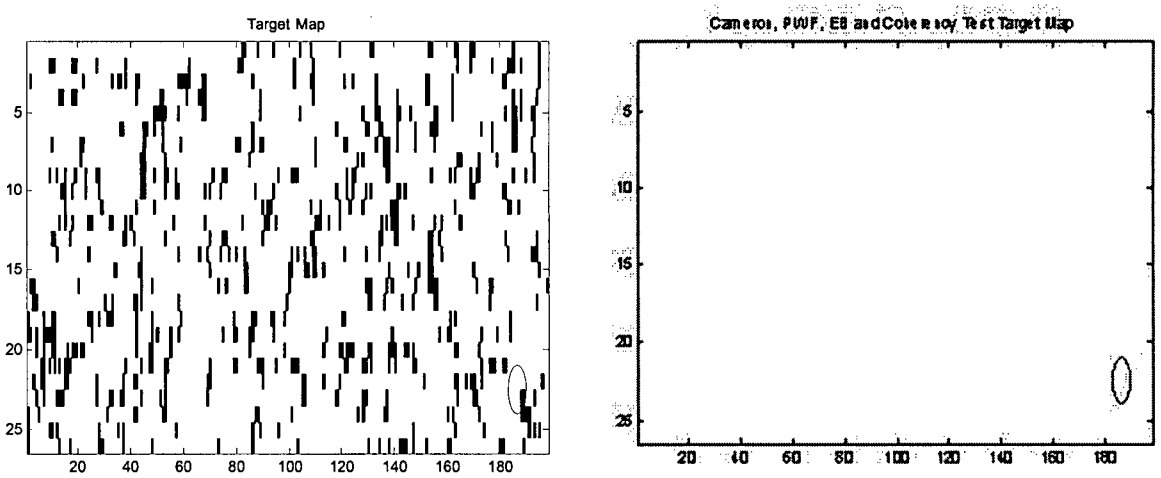

(a) (b)

Figure 59: Target 5 - Plots from Methodologies 3 and 4. (a) Freeman-Durden target map showing pixels that present a percentage of dihedral scattering above the chosen threshold. (b) Combined results of Cameron (dihedrals plus narrow dihedrals), PWF, Even Bounce and Coherence Test.

A.5 – Target 12

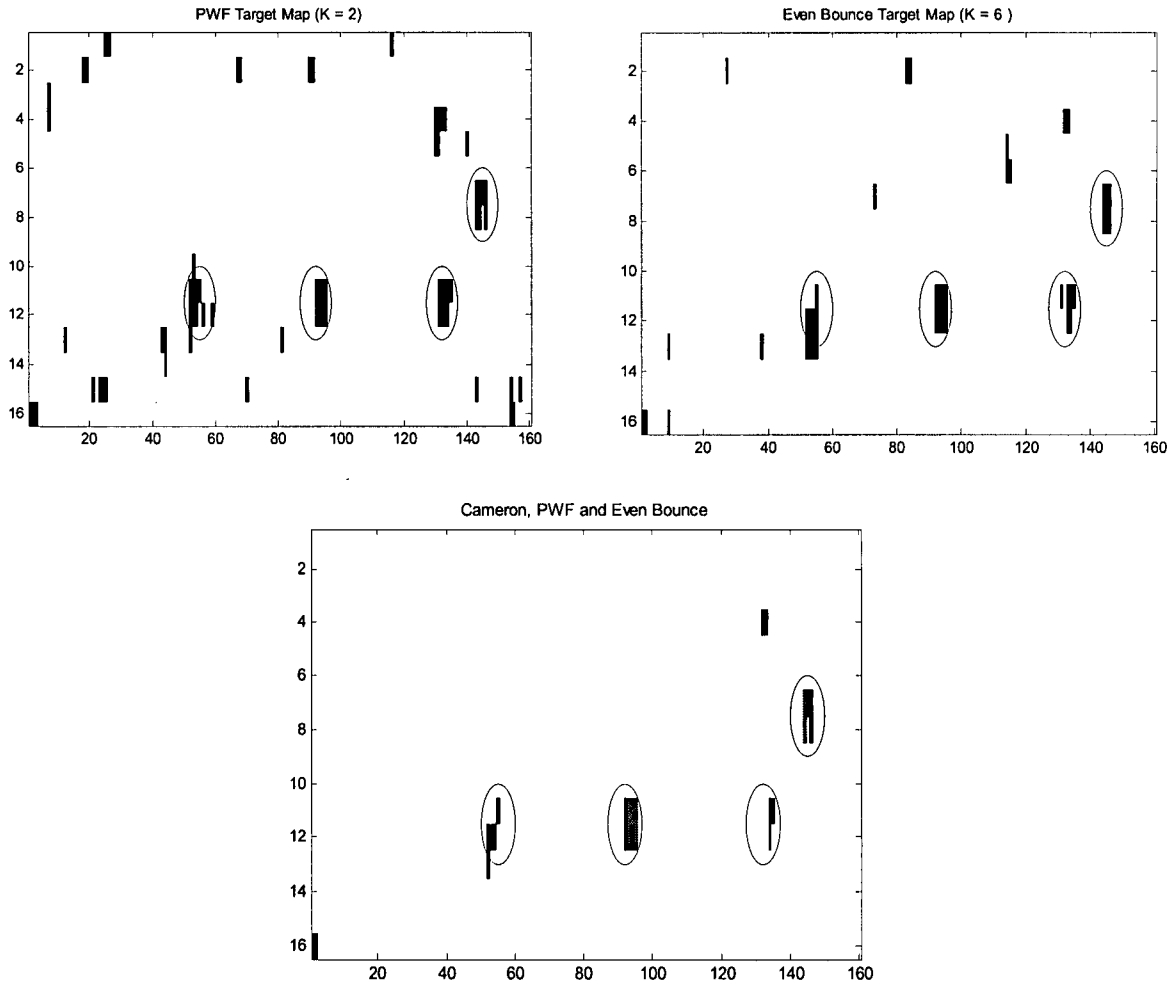

Figure 60: Target 12 - Plots from Methodology 1. Upper left: PWF target map. Upper right: Even Bounce target map. Bottom: combined result of Cameron (dihedrals plus narrow dihedrals), PWF and Even Bounce. K is the CFAR constant.

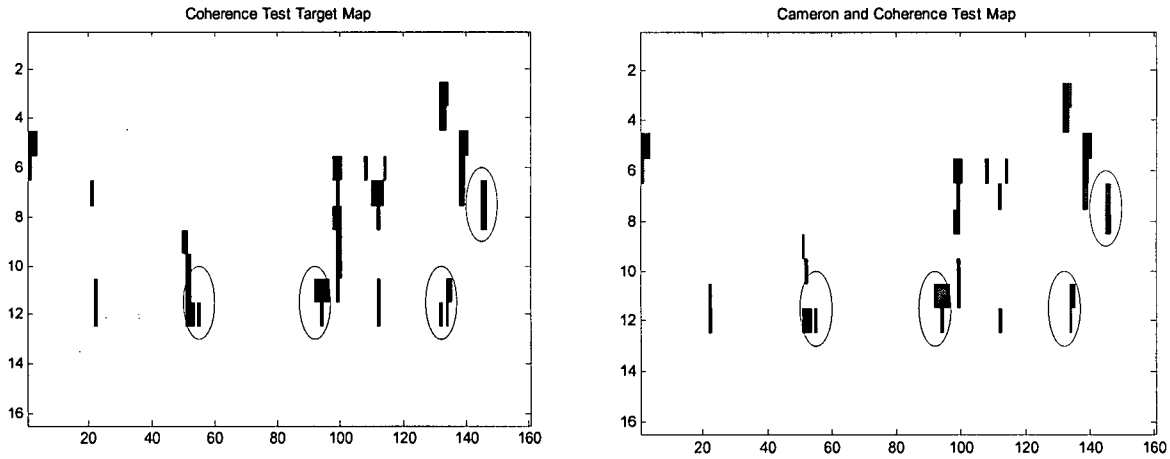

(a) (b)

Figure 61: Target 12 - Plots from Methodology 2. (a) Coherence Test target map. (b) Combined result of Cameron (dihedrals plus narrow dihedrals) and Coherence Test.

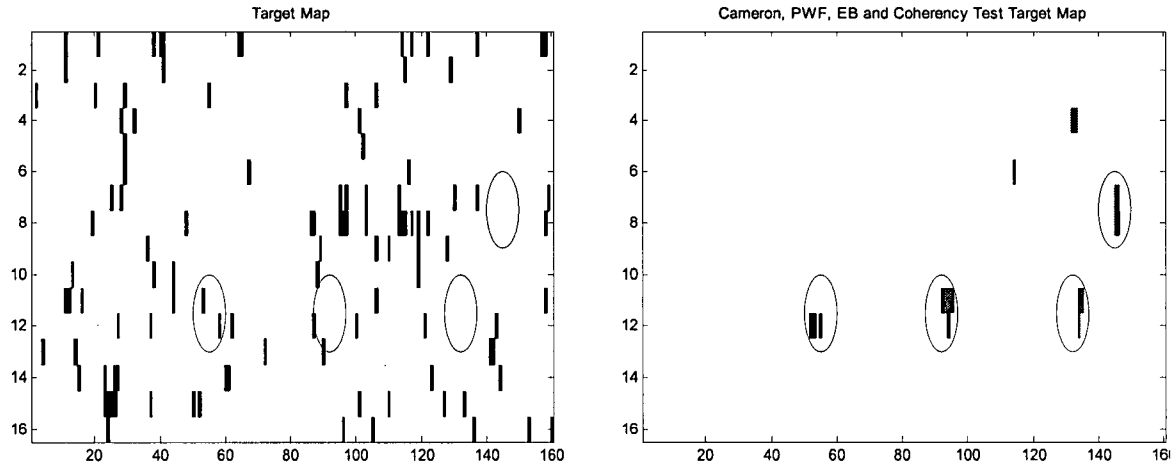

(a) (b)

Figure 62: Target 12 - Plots from Methodologies 3 and 4. (a) Freeman-Durden target map showing pixels that present a percentage of dihedral scattering above the chosen threshold. (b) Combined results of Cameron (dihedrals plus narrow dihedrals), PWF, Even Bounce and Coherence Test.

A.6 – Target 20*

* This is the scene used by Lukowski *et al.* [10]

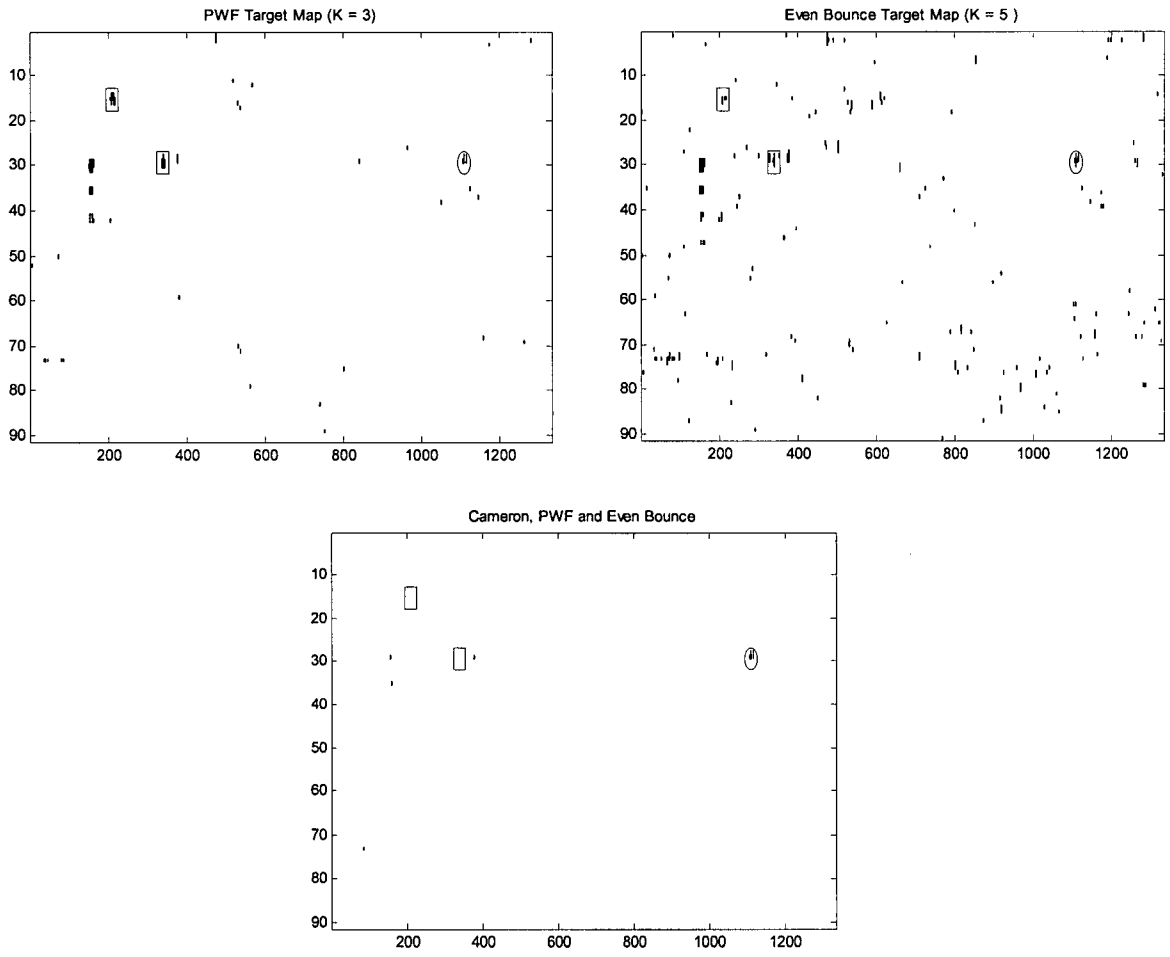

Figure 63: Target 20 - Plots from Methodology 1. Upper left: PWF target map. Upper right: Even Bounce target map. Bottom: combined result of Cameron (dihedrals plus narrow dihedrals), PWF and Even Bounce. K is the CFAR constant. Rectangles show locations of corner reflectors.

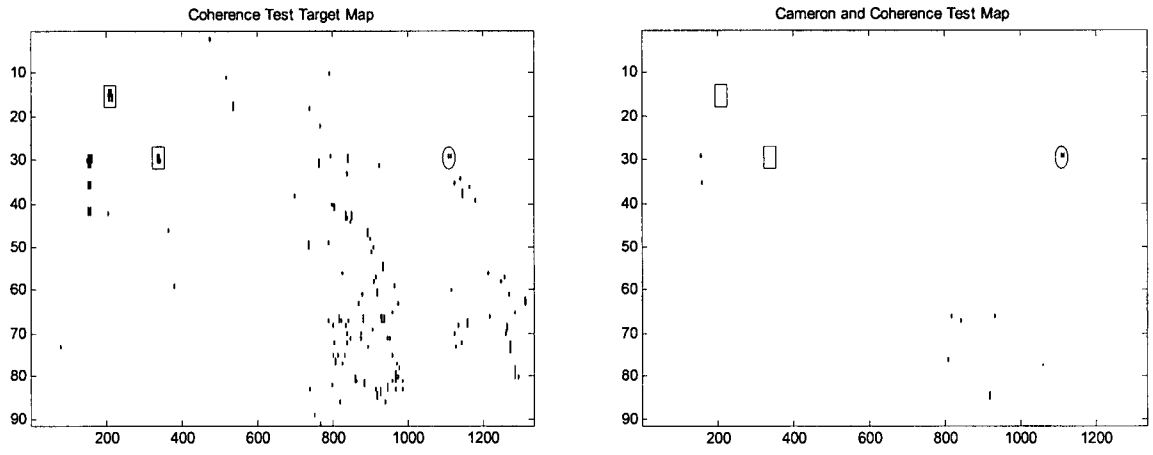

(a) (b)

Figure 64: Target 20 - Plots from Methodology 2. (a) Coherence Test target map. (b) Combined result of Cameron (dihedrals plus narrow dihedrals) and Coherence Test. Rectangles show the location of corner reflectors.

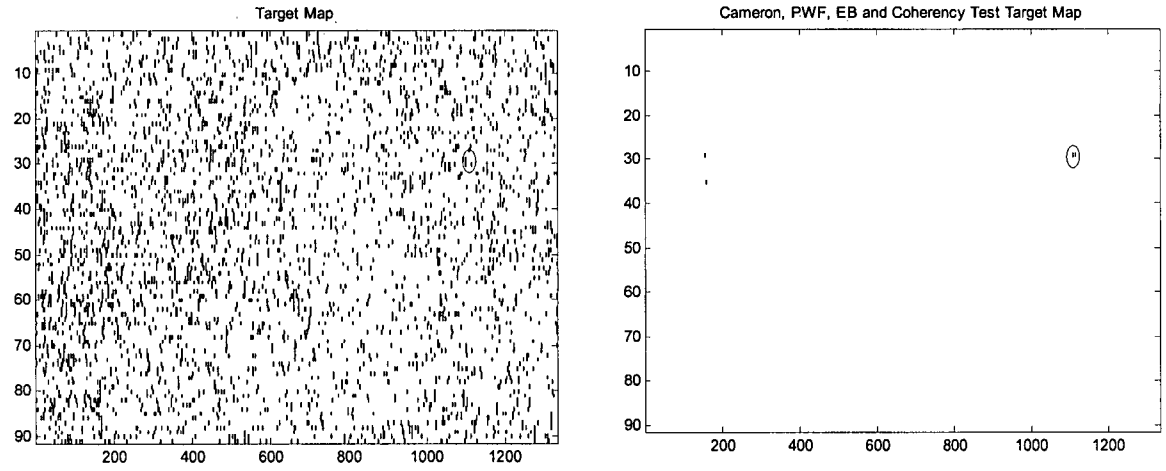

(a) (b)

Figure 65: Target 20 - Plots from Methodologies 3 and 4. (a) Freeman-Durden target map showing pixels that present a percentage of dihedral scattering above the chosen threshold. (b) Combined results of Cameron (dihedrals plus narrow dihedrals), PWF, Even Bounce and Coherence Test.